Spectroscopic interrogation of differential mobility spectrometry selected, isolated, gas-phase molecular clusters

by

Fiorella Villanueva Heldmaier

A thesis
presented to the University of Waterloo
in fulfillment of the
thesis requirement for the degree of
Master of Science
in
Chemistry

Waterloo, Ontario, Canada, 2020

Author's Declaration

This thesis consists of material all of which I authored or co-authored: see Statement of Contributions included in the thesis. This is a true copy of the thesis, including any required final revisions, as accepted by my examiners.

I understand that my thesis may be made electronically available to the public.

Statement of Contributions

Chapter 3 and Appendix A uses portions of a final report submitted for the course CHEM 740: Computational Chemistry. The authors are listed as:
Fiorella Villanueva Heldmaier
Rebecca Huard

Chapter 5 incorporates sections of a manuscript ready for submission titled *"UVPD spectroscopy of differential mobility-selected, adenine prototropic isomers"* with coauthors as listed:
Fiorella Villanueva Heldmaier
Neville Coughlan
Rebecca Huard
Marcel Nooijen
W. Scott Hopkins

Abstract

One of the most elusive challenges facing mass spectrometry-based methods is the study of isomers. Oftentimes, isomers produce identical fragmentation spectra that make structural elucidation and assignment from MS data alone difficult. In this thesis, the problem of studying isomers is addressed by employing differential mobility spectrometry-mass spectrometry experiments coupled with ultraviolet photodissociation action spectroscopy (DMS-MS-UVPD). Using a combination of experimental and computational techniques, the validity of DMS-MS-UVPD studies for applications in isomer separation and distinction is verified. During the course of two subprojects, DMS-MS-UVPD is successfully applied to separate and distinguish between geometric isomers and tautomers. First, DMS-MS experiments are conducted, and the dynamic clustering behaviour of each species is determined. Once the clustering behaviour is well-characterized, the DMS-MS parameters are optimized to select for the species of interest and used as an ion filter for subsequent UVPD action spectroscopy experiments. The results from the action spectroscopy studies produce a vibronic spectrum that can be compared to theoretical models for correct isomer assignment. Due to the complexity of excited state phenomena, many computational models were used to accurately predict vibronic spectra, including Franck-Condon based approaches and non-adiabatic dynamics. The work presented in this thesis provides the framework for the use of DMS-MS-UVPD in other isomer systems.

Acknowledgements

First and foremost, I would like to express my deepest gratitude to my supervisor, Prof. W. Scott Hopkins, for his continued guidance and support throughout the years. From my second year spectroscopy course to the end of my master's degree, Prof. Scott Hopkins has always found a way to pass on his passion for science to me.

I would also like to acknowledge my committee members Prof. Marcel Nooijen and Dr. Rick Marta. Since the first time I ran a computational chemistry calculation, Prof. Marcel Nooijen has always been available to answer my questions, provide guidance, and propose new ways to improving my simulations. From my time as an undergraduate student, Dr. Rick Marta has always been available to provide both academic and personal advice, as well modelling what it means to be a student-focused instructor. I will always be thankful for the help and expertise they provided during the course of my graduate studies.

I would like to recognize all the people who's assistance was imperative for the success of this thesis. First of all, I would like to acknowledge Dr. Neville Coughlan, for creating the experimental set up for our photodissociation spectroscopy experiments, and always being willing to share his expertise while being patient with my questions. I would also like to thank the undergraduate research students who contributed directly to the work being presented here today; Cailum Stienstra and Rebecca Huard. Cailum was instrumental in collecting DMS data for Chapter 4 and Rebecca directly contributed to the theoretical work presented in Chapter 5. Furthermore, I wish to thank Prof. Graham Murphy's research group at the University of Waterloo, and Zoltan Richter-Bisson in particular, for synthesizing humulone standard for our use in Chapter 4. I would also like to express my gratitude towards Prof. Fabrizio Santoro at the National Research Council of Italy for

graciously providing the diabatization scheme scripts needed for the construction of the vibronic model presented in Chapter 5.

Furthermore, I wish acknowledge all the members of the Hopkins group- past and present. It has been an honour to work alongside the best and the brightest physical chemists, and I know I would not be the scientist I am today without them. I would like to especially recognize my friends and colleagues in the Department of Chemistry; Yuting Li, Weiqiang Fu, Nour Mashmoushi, Ce Zhou, Suzy Lim, and Adam Marr, for always providing the best advice and support during the course of this thesis.

I would also like to thank all my friends for their words of encouragement during these past two years, and my longtime friend Natalie Di Giandomenico in particular, for donating her time to proofread this thesis. Lastly, I would like to thank my family for their constant love, support, and patience. I would particularly like to thank my sister, Isabella, for always providing laughter in the toughest times.

Table of Contents

List of Tables

List of Figures

List of Abbreviations

ACN Acetonitrile

AH Adiabatic hessian

B3LYP Becke-3-Lee-Yang-Parr

BO Born-Oppenheimer

BP86 Becke 1988 exchange and Perdew 86 correlation

CAM-B3LYP Coloumb attenuating model, Becke-3-Lee-Yang-Parr

CCS Collision cross section

CCSD Coupled cluster singles and doubles

CCSD(T) Coupled cluster singles, doubles, and perturbative triples

CID Collision induced dissociation

CV Compensation voltage

DFT Density functional theory

DLPNO Domain-based local pair-natural orbitals

DMS Differential mobility spectrometry

DNA Deoxyribonucleic acid

EMC Enhanced multiply charged scan

EOM Equation of motion

EPI Enhanced product ion

ESI Electrospray ionization

FC Franck-Condon

FCFs Franck-Condon Factors

FE Fragmentation efficiency

GD3 Grimme's dispersion correction

GGA Generalized gradient approximation

HDX Hydrogen-deuterium exchange

HF Hartree-Fock

HOMO Highest occupied molecular orbital

HPLC High-performance liquid chromatography

IBU International bitterness unit

IMS Ion mobility spectrometry

IP Ionization potentials

IPA Isopropanol

IRMPD Infrared mulitphoton dissociation

LDA Local density approximation

LUMO Lowest unoccupied molecular orbital

LVC Linear vibronic coupling

MCTDH Multiconfigurational time-dependent Hartree

MeOH Methanol

MS Mass spectrometry

MS/MS Tandem mass spectrometry

Nd:YAG Neodymium-doped ytrrium aluminum garnet

OPO Optical parameteric oscillator

PBE Perdew-Burke-Enzerhof

PCM Polarized continuum model

PES Potential energy surface

PID Photoinduced dissociation

PM6 Parameterization method 6

RNA Ribonucleic acid

STEOM Similarity transformed equation of motion

SV Separation voltage

TD-DFT Time-dependent density functional theory

UVPD Ultraviolet photodissociation

UV-UV Ultraviolet-ultraviolet

UV-Vis Ultraviolet-visible

VG Vertical gradient

Chapter 1

Introduction

Isomers are ubiquitous in chemistry. Each isomer within a family of molecules can possess different physical, chemical, and biological properties. For example, stereoisomers of lipids that differ by double bond position have been shown to exhibit different biological functions, and age-related isomerization of aspartic acid residues in eye proteins have been linked to the development of cataracts. [1, 2] Due to potential biological implications, it is imperative to study and understand the unique properties of isomers individually, requiring that isomeric species are separated and isolated from each other. Conventionally, small molecules can be studied using tandem mass spectrometry (MS/MS). MS/MS can provide accurate details regarding the molecular mass of a given species and can provide key insights into the structural properties of the molecule, using collision induced dissociation (CID) and other soft ionization techniques, by analyzing the resultant fragmentation spectrum.[3, 4, 5, 6] However, in the case of many stereoisomers, fragmentation spectra are not enough to distinguish or elucidate structural properties, due to one or more isomers having similar fragmentation channels.[3, 4] In these instances, one often needs to rely on a

chromatographic technique to spatially separate ions of interest prior to investigation with MS/MS methods.

A relatively new analytical tool that has been demonstrated to separate isomers effectively is differential mobility spectrometry (DMS). DMS is an ion chromatographic technique that separates ions spatially in the gas phase based on their differential mobility under high and low electric field conditions in a designated carrier gas.[7, 8] As a result of using an ion's differential mobility to distinguish between ions, DMS separation is highly structure dependent, allowing for analysis of species otherwise indistinguishable by traditional mass spectrometry.[9] DMS has been used to separate a plethora of isomers of all sizes, such as isomers of protonated dipeptides, deprotonated glycopeptides, protonated aniline, and protonated 4-aminobenzoic acid. [10, 11, 12, 13] Once separated, mass spectrometry-based techniques are employed to characterize the resolved species. Recently, ultraviolet photodissociation action spectroscopy (UVPD) has been used in conjunction with MS/MS to provide a direct method of identification by probing an ion's electronic structure.[14, 15]

This thesis explores the use of DMS-MS coupled with UVPD action spectroscopy as an analytical tool for the detection and characterization of isomers in the gas phase. In order to rationalize experimental findings, analogous computational studies were undertaken and provided unique insights into the electronic structure of the molecules of interest. Through the completion of two subprojects, two different applications of DMS-MS-UVPD are demonstrated and its validity as an analytical method is verified.

In Chapter 2, the fundamentals behind the methods used during the course of this thesis are presented. First, an in-depth description of DMS is reported. Afterwards, the the-

ory behind photodissociation is discussed, along with an introduction to UVPD action spectroscopy. Following a description of experimental methods, the theoretical framework behind the main computational tools used will be illustrated. Ground state and excited state electronic structure calculations were primarily performed using density functional theory (DFT) and its time-dependent analogue (TD-DFT). An introduction to the Franck-Condon (FC) principle is presented, as well as a summary of FC-based approaches to simulating vibronic spectroscopy. When the FC model was deemed insufficient to accurately predict vibronic spectra, a rigorous treatment of non-adiabatic effects was conducted using a linear vibronic coupling Hamiltonian in a diabatic basis set. The excited state dynamics was then evaluated using a wave packet propagator within the multiconfigurational, time dependent Hartree (MCTDH) framework. A full description of this theoretical model is presented in Chapter 3.

In Chapter 4, the use of DMS-MS-UVPD to separate and identify beer bittering compounds is demonstrated. Beer is a popular drink for its bitter, or hoppy, taste and aroma. The bitterness profile of a given beer is primarily affected by the addition of hops (*Humulus lupulus*) during the brewing process. Hops contains a large quantity of humulone, whom after undergoing thermal isomerization during wort boiling, isomerizes into the bitter tasting isohumulone epimers.[16] Deprotonated humulone and isohumulone were subjected to DMS-MS studies individually to characterize their dynamic clustering behaviour under different conditions and gaseous environments. The DMS-MS parameters were optimized to allow for maximum separation between deprotonated humulone and isohumulone. Afterwards, the two species underwent spectroscopic interrogation and their UV-PD action spectrum were recorded and compared to their computational vibronic spectrum, calculated using FC simulations. Key differences in the vibronic spectrum of deprotonated

humulone and isohumulone were shown, thus demonstrating that DMS-MS-UVPD is an effective technique for monitoring bitter molecules in beer.

In Chapter 5, UVPD action spectroscopy is used to directly verify that the two resolved species of protonated adenine, as presented in the work by Anwar et al., can be attributed to two different tautomeric forms.[17] Protonated adenine is of biological interest due to the fact that it serves unique biological purposes within the cell. For instance, adenine-cytosine mismatched base pairs in RNA have been shown to be stabilized when the adenine residue is protonated at a specific site [18], whereas protonation on a different site plays a role in ribosome phosphodiester cleavage.[19] Therefore, due to the fact that different tautomeric forms of protonated adenine have different biochemical activities, a thorough investigation of each isolated tautomer needs to be performed. The recorded action spectrum for each resolved protonated adenine species was compared to theoretical vibronic spectra, allowing for tautomer identification and assignment. Due to the presence of many degenerate and iso-energetic excited states in tautomers of protonated adenine, a rigorous treatment of the non-adiabatic excited state dynamics was necessary to accurately predict vibronic spectrum. Through observed differences in their electronic structure, both experimentally and theoretically, it was shown that the two resolved species arise from the presence of two different tautomers.

Through both subprojects studied during the course of this thesis, it is revealed that isomers can be separated by DMS-MS and their identification is made possible by using UVPD to probe their electronic structure. The use of computational tools helps reveal further insights into the electronic and geometric structure of the species and can provide insights into their unique fragmentation pathways. The work presented in this thesis opens

the door to other possible applications for the use of DMS-MS-UVPD as an analytical technique.

Chapter 2

Methods

In this chapter, a theoretical background to key experimental and computational techniques used during the course of this thesis is provided. Relevant instrument optimization parameters and computation specifications are discussed in their relevant results chapters.

2.1 Experimental methods

In this section, the major analytical technique being used in this thesis, differential mobility spectrometry, is described. Afterwards, a discussion on ultraviolet photodissociation action spectroscopy is provided. Ultraviolet photodissociation is an additional tool used in conjunction with differential mobility spectrometry studies to further characterize species of interest.

2.1.1 Differential mobility spectrometry

Differential mobility spectrometry (DMS) is an ion chromatographic technique traditionally used to separate isobaric compounds.[7] DMS is a variant of ion mobility spectrometry (IMS) that operates on the underlying principle that an ion's mobility within a carrier gas depends on the electric field strength. In conventional drift tube IMS, ions are driven through a gas filled cell using a low electric field.[20, 21, 22] The amount of time an ion spends in the cell before eluting, denoted the drift time t_d, is measured and the ion mobility, K, can be determined:

$$\begin{aligned} K &= \frac{v_d}{E} \\ K &= \frac{L}{t_d E} \end{aligned} \tag{2.1}$$

where v_d is the ion velocity in the drift tube, L is the length of the mobility cell, and E is the electric field strength.

Structural information can be derived from ion mobility measurements by calculating the ion's collision cross section (CCS) Ω.[22] The CCS describes the interaction area between an ion and the carrier gas molecules within the drift tube and it is dependent on the ion's charge, shape, and size. CCSs can be calculated using the Mason-Schamp equation:

$$\Omega = \frac{3eZ}{16N}\left(\frac{2\pi}{\mu k_b T}\right)^{\frac{1}{2}}\frac{1}{K} \tag{2.2}$$

where e is the elementary charge, Z is the charge of the ion, N is the number density of

the carrier gas molecules, μ is the reduced mass of the ion-gas system, k_b is the Boltzmann constant, T is the temperature of the carrier gas, and K is the ion mobility. Due to the relationship between CCS and ion mobility, changes in CCS between ions will result in different drift time.

Where DMS differs is that it leverages the field-dependence of an ion's mobility. The field-dependence can be described by [23]:

$$K(\frac{E}{N}) = K_o[1 + \alpha(\frac{E}{N})] \tag{2.3}$$

where K_o is the zero-field mobility coefficient, E is the applied electric field magnitude, N is the concentration of neutral particles, and α is a parameter which relates mobility to $\frac{E}{N}$.[23]

High- and low-field conditions are generated by the application of an asymmetric potential waveform called the separation field, with peak voltage known as the separation voltage (SV).[7] Figure 2.1 shows a schematic diagram of a typical DMS cell and an ion's trajectories when under the separation field. When exposed to the separation field, the ions adopt a zig-zag motion deviating from their initial trajectory along the longitudinal axis of the DMS cell.[7] During the high-field cycle, ions move off axis towards one of the electrodes. In contrast, during the low-field cycle, ions move away from the electrodes and return on axis towards the exit orifice.[23] Following the introduction of a collision gas, such as $N_{2(g)}$, the ion's differential mobility under high versus low-field conditions results in a trajectory change towards one of the planar electrodes, determined ultimately by the α parameter.[23] To correct the trajectory deviation and to allow for ion transmission, a counteracting compensation voltage (CV) is applied.[7, 23] For a given SV, an ion's mobility parameter, α is encoded in the unique CV required to stabilize the trajectory in order

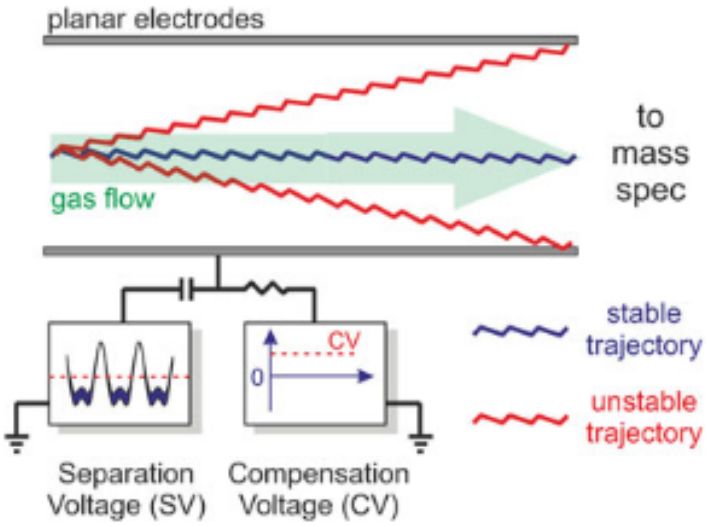

Figure 2.1: Schematic of a typical DMS cell.[7]

to transmit a desired ion for detection.[7, 23]

Physical separation can be enhanced or enabled through the addition of volatile solvents (e.g., methanol, isopropanol, water, etc.) into the curtain gas. These polar solvents are seeded into the collision gas at 1.5 % (v/v).[7, 23] Upon introduction of volatile solvents, the behaviour of the ion changes and an observed change in differential mobility can be observed. The change in ion mobility can be rationalized by considering the dynamic ion-solvent clustering and declustering behaviour during the separation field cycle.[7, 23] Under a low field, ion-solvent clusters can form. This leads to an artificial increase in the ion's collision cross section (CCS) with the carrier gas, and a corresponding reduction in its mobility. In contrast, under high field conditions, ions are accelerated and heated, leading to desolvation and a corresponding increase in mobility.[7] This dynamic clustering behaviour is particularly useful for physical separation due to its dependency on the analyte-solvent

interaction potential.[7, 23] The analyte-solvent interaction potential is dictated by the geometric structure of the species. Additionally, the resulting microsolvation and evaporation cycles themselves are dependent on the analyte's geometric structure, drastically changing DMS behaviour of similar structures (*viz.* isomers and tautomers).[23] The data collected during a DMS study as it scans through CV at a given SV is called an ionogram. By recording the optimal CV(s) needed to maximize ion transmission at incremental SVs,

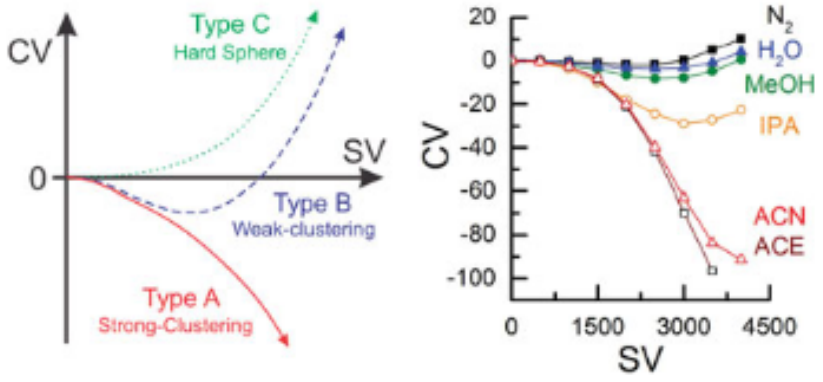

Figure 2.2: Left: Example of the three types of clustering behaviour found in a dispersion plot. Right: Dispersion plot collected for tetramethylammonium using different gaseous environments and modifiers [7].

a dispersion plot can be created.[23] A dispersion plot is an indirect physical representation of the α parameter, providing insights into an ion's physical characteristics and ion-solvent interactions. The shape of a dispersion plot can be classified as either type A, B, or C. These curves are illustrated in Figure 2.2. More exotic dispersion plots, such as type D and E, have also been documented in the literature, but will not be discussed in this thesis.[23] In Type A behaviour, more negative CVs are required to transmit ions as SV increases. This is indicative of strong ion-solvent clustering. In Type C behaviour, the ion interacts

weakly with the neutral gas molecules, and thus the collisions are approximately hard sphere. In this scenario, clustering does not occur, and the optimal CV required for ion transmission becomes more positive with increasing SV. In Type B behaviour, a decrease in CV for increasing SV is initially observed, followed by an increase in CV after some critical point. The behaviour is described as weak clustering, an intermediate between Type A and C.[7]

In summary, DMS exploits the unique dynamic clustering behaviour of ions to distinguish isobaric species. By introducing solvent molecules into the curtain gas, it is possible to distinguish between similar species by further altering their trajectory through the DMS cell.

2.1.2 Ultraviolet photodissociation action spectroscopy

After DMS separation, tandem mass spectrometry (MS/MS) experiments can be employed to supply additional information to aid in analyte determination. This is commonly done using collision-induced dissociation (CID), where an ion is activated and fragmented by collision with an inert gas. In addition to CID experiments, DMS-MS studies have been paired with indirect MS methods like hydrogen-deuterium exchange (HDX)[24, 25] to facilitate species identification. Recently, ultraviolet photodissociation action spectroscopy has been paired with DMS-MS to provide a direct method of species identification by probing the electronic structure of DMS-MS selected molecular ions.[26, 27]

Photodissociation is a useful technique due its high energy deposition, allowing for ac-

cess to alternative activation mechanisms and new fragmentation pathways that are too high energy for traditional CID to access.[28] Photodissociation is the process in which a bound molecule fragments upon absorption of one or more photons. The photon is absorbed and its energy is converted into internal molecular energy. The internal molecular energy can be released in many ways. Among these options if by fragmenting, if the transferred energy exceeds the binding energy of the weakest bond within the molecule. [29]. For a general polyatomic molecule ABC, the photodissociation process can be written as [30, 29]

$$ABC + N_{photon}h\nu \xrightarrow{(1)} (ABC)^* \xrightarrow{(2)} AB(\alpha) + C(\beta) \tag{2.4}$$

where $h\nu$ is the photon energy with frequency ν and N_{photon} is the number of absorbed photons. (ABC)* is the excited complex prior to fragmentation and the labels α and β specify the particular internal quantum states of the product ions. The amount of energy needed to fragment the excited complex depends on the dissociation energies of each bond. [29]

Ranges of dissociation energies depend on the type of molecule being investigated. For example, a few thousandths of an eV is needed to fragment a van der Waals complex, whereas several eV is needed to cleave a covalent bond[29]. The wide range of dissociation energies naturally leads to the usage of various different light sources for photodissociation, such as infrared or ultraviolet-visible light. Experimentally, photodissociation is monitored by recording the depletion of the parent ion and the formation of product ions. There are many possible photodissociation mechanisms that may be physically realized. We will be-

gin our discussion with the simple case of diatomic molecules. For a diatomic molecule AB, there are three main pathways for photodissociation, namely direct photodissociation, predissociation, and spontaneous radiative dissociation. [30]. Diagrams depicting all three mechanisms can found in Figure 2.3. In direct photodissociation, a molecule absorbs a

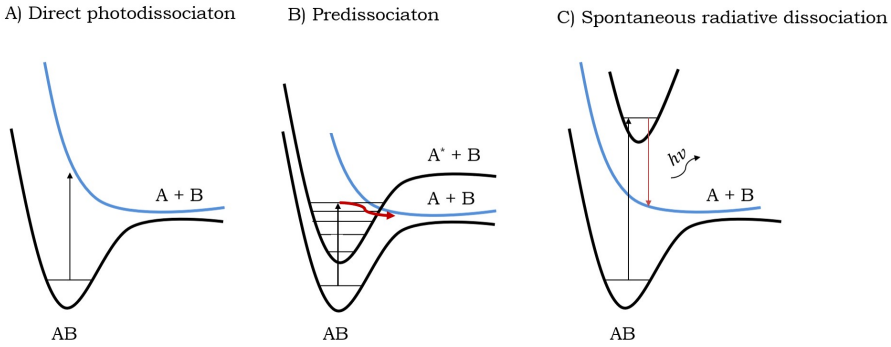

Figure 2.3: Diagram of a) direct photodissociation, b) predissociation, and c) spontaneous radiative photodissociation for an arbitrary diatomic molecule AB. Adapted from Dishoeck et al. [30]

photon and is excited into a higher excited electronic state that is repulsive in nature along the nuclear coordinate r_{AB}, ultimately causing bond breakage, as shown in Figure 2.3a.[30, 29] In a repulsive state, the atoms repel each other, yielding a potential energy surface (PES) that does not have a minimum. The lack of minimum results in no discrete vibrational levels, forming a continuum. [31] The photon energy is partitioned within the molecule as:

$$\hbar\nu + D_o = E_{trans} + E_{int} \tag{2.5}$$

Where $\hbar\nu$ is the photon energy, D_o is the dissociation energy needed to break the AB bond,

E_{trans} is the translational energy, and E_{int} is the internal energy of the product ions, which includes the vibrational, rotational, and electronic contributions. [29]

In predissociation, the molecule absorbs a photon and is excited into a bound excited electronic state. Once on the bound excited state surface, the excited molecule undergoes a non-radiative transition into a different excited state that is repulsive in nature and subsequently fragments, as shown in Figure 2.3b. [30, 29] In other words, the fragmentation takes place on a PES other than that to which the molecule was initially excited. Such examples of interactions causing non-radiative transitions are spin-orbital couplings between states of different spin multiplicity, or between states of the same symmetry through non-adiabatic couplings. [30]

Finally, in spontaneous radiative photodissociation, the molecule absorbs a photon and is excited into a bound excited electronic state. The excited molecule then undergoes emission to relax the molecule into either a lower-lying repulsive excited state or into the ground electronic state dissociation threshold, leading to fragmentation. [30, 29] This is demonstrated in Figure 2.3c.

As a molecule increases in size, it becomes less likely that the photodissociation process can be described as following one of the mechanisms depicted in Figure 2.3. For a given PES, there exists infinite vibrational levels, increasing until the dissociation threshold energy of the potential is reached. For a sufficiently large amount of atoms, the density of vibrational levels increase until formation of a quasi-continuum that can couple with excited states non-radiatively, through interactions like conical intersections. In this scenario, a molecule in the excited state may rapidly relax to a highly excited vibrational level on the electronic

ground state and fragment on this surface, through a process called internal conversion. [30]

2.1.3 Combining DMS and UVPD

In order to leverage the unique abilities of UVPD, a commercial DMS-MS apparatus was coupled with a Nd:YAG-pumped optical parametric oscillator (OPO). The details of experimental set up can be found described in detail elsewhere[26] and a schematic diagram of the setup can found in Figure 2.4. After DMS isolation, the ion of interest is held in

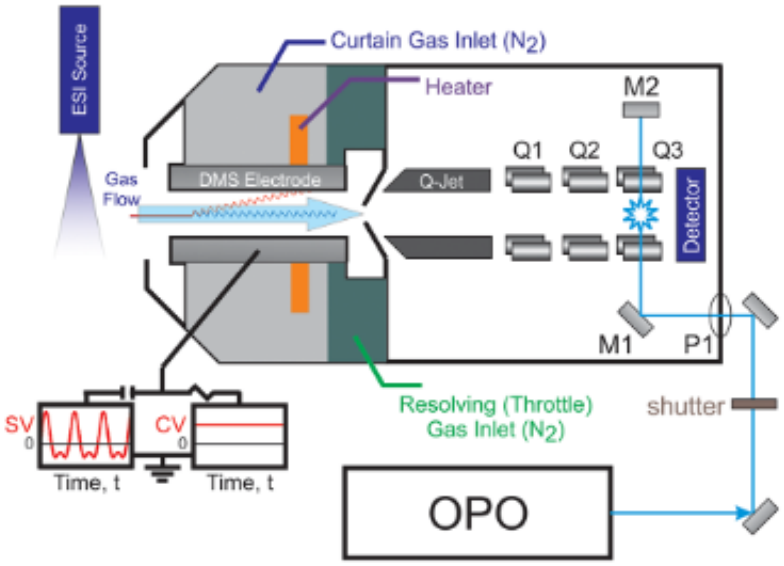

Figure 2.4: Schematic diagram of modified DMS-MS instrument that has become UVPD enabled. [30]

a quadrupole ion trap and irradiated by the OPO. At each wavelength, the parent and product ion fragment intensities are monitored and an action spectrum is generated using

the fragmentation efficiency:

$$FE = \frac{\lambda}{P} \log \frac{\sum I_{par}}{(\sum I_{frag} \sum I_{par})} \tag{2.6}$$

where FE represents the fragmentation efficiency, λ is the wavelength being irradiated by the OPO, P is the power of the incident wavelength, I_{par} is the intensity of the parent peak, and I_{frag} is the intensity of the fragment peaks. By plotting the FE at each wavelength, the action spectrum is generated.

2.2 Computational methods

In this section, a brief outline the important computational techniques used for experimental verification is presented. First, a description of the main framework used for our electronic structure calculations, ground state density functional theory, is provided. Afterwards, a brief description of its time-dependent analogue used for excited state modelling is given. Finally, an introduction to the Franck-Condon principle is presented and an explanation and illustration of the two types of Franck-Condon simulations used during the course of this project are provided.

2.2.1 Density functional theory

One of the most intrinsic properties of a molecule is its electronic structure. Determination of a molecule or ion's electronic structure allows insights into molecular properties including dipole moments as well information regarding the PES and the geometry of the species. In quantum mechanics, the most direct way to approximate the electronic structure is to solve the Schrödinger equation and obtain the wavefunction of the system. In a typical ab initio

computation, the calculation of the molecular wavefunction is one of the most crucial steps. The most common approach to determining the wavefunction is using the Hartree-Fock (HF) method. In the HF framework, it is proposed that for a molecule comprised of N electrons, the exact molecular wavefunction can be approximated to be a Slater determinant of N spin-orbitals.[32] However, the HF framework assumes no electron interactions (correlation effects). In order to reincorporate correlation effects, the wavefunction is subjected to post-HF modifications such as coupled-cluster theory or Møller-Plesset configuration interaction calculations.[32] Although this yields accurate results when compared to experiments, taking into consideration electron interactions drastically increases the degrees of freedom that must be considered, and therefore, the calculation increases in expense exponentially as N increases.[32]

One of the most popular and successful ways of balancing the expense vs accuracy problem in computational chemistry is using density functional theory (DFT). In DFT, the fundamental concept is that all properties of an interacting system, like a molecule, can be obtained by determining the electron density. The electron density is defined as the probability of finding any one electron somewhere in space and is expressed mathematically as $n(r) = 2\sum_i \psi_i^*(r)\psi_i(r)$, where $\psi_i(r)$ and $\psi_i^*(r)$ represent the wavefunction and the complex conjugate of an electron, respectively. Current realization of DFT is governed by two theorems determined by Hohenberg and Kohn[33] in 1964 and the subsequent derivation of the Kohn-Sham equations the following year.[34] The first Hohenberg-Kohn theorem states that the ground state energy, and therefore, the wavefunction, of a given system obtained from the Schrodinger equation is a functional of the electron density. [35]. In other words, there exists a one-to-one mapping between the ground state molecular wavefunction and the ground state electron density. This result implies that instead of using

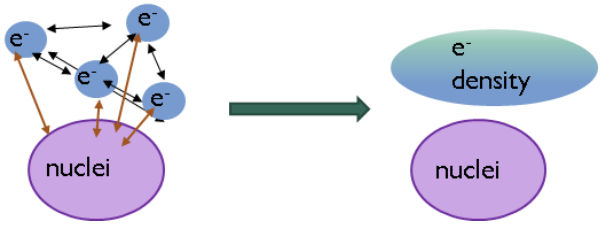

Figure 2.5: Representation of how DFT considers interacting electrons as electron density

a 3N-dimensional wavefunction to determine all ground state properties, one can use the electron density, a function comprised of only three spatial variables. [32, 35] The second Hohenberg-Kohn theorem states that the energy of the electron distribution is given by a functional of the overall electron density. At the ground state density, the functional is minimized. [32, 35]. These two theorems reduce the complexity of solving for molecular properties. Instead of solving the many-body Schrödinger equation for the molecular wavefunction, one tries to minimize the density functional to find the electron density of the system. [32] It is important to note that although Hohenberg-Kohn defined important properties of the density functional, they did not address what the general functional looks like. [32].

The Kohn-Sham equations address finding the electron density of a given system. In this approach, a fictitious and non-interacting system is created with identical electron density to the original system. The non-interacting nature makes solving the Schrodinger equation simple since the wavefunction can be represented as a sum of Slater orbital determinants called the Kohn-Sham determinant.[32, 35] One can write the resulting energy functional as:

$$E(\psi_i) = E_{known}(\psi_i) + E_{xc}(\psi_i) \tag{2.7}$$

Where the known energy functional can be further broken down into:

$$\begin{aligned} E(\psi_i) = \frac{h^2}{m}\sum_i \int \psi_i^* \nabla^2 \psi_i d^3r \\ + \int V(r) n(r) d^3r \\ + \frac{e^2}{2}\int\int \frac{n(r)n(r')}{|r-r'|} d^3r d^3r' \\ + E_{ion} \end{aligned} \tag{2.8}$$

Where the first term is the electron kinetic energy, the second term is the Coulombic interaction between electrons and nuclei, the third term is the nuclear Coulombic interaction, and the fourth term is the ion energy.[35]

The exchange-correlation functional, E_{xc} needs to be defined to include all the quantum effects not inherently incorporated within the E_{known} functional. Unfortunately, there is no universal solution known for the exchange-correlation functional, and computational efforts have been directed at finding suitable trial exchange-correlation functionals for accurate results using a variety of approximations and assumptions. [35]

One of the most common approximations used to define the exchange-correlation function is the local density approximation (LDA). In this approximation, only the density at a specified position is considered. Another common approximation is the generalized gradient approximation (GGA), where a dependency is placed on both the electron density

and its gradient. Such functionals include BP86[36] and PBE.[37] Finally, another common approach for defining functionals is the Hybrid functional approach, which mix GGA with the exact Hartree–Fock exchange term. An example of this is the popular functional B3LYP. [36, 38]

2.2.2 Time-dependent density functional theory

Time-dependent density functional theory, or TD-DFT, is a natural extension of ground state DFT for excited states that includes the interaction of electromagnetic potential.[39] Similar to the time independent analogue, TD-DFT provides an exact solution to the time dependent Schrodinger equation.[39] It postulates that the time-evolving electron density accounts for all the properties of the system under a time-dependent field. The Hohenberg-Kohn theorems were extended by Runge and Goss in 1984.[40]

2.2.3 Franck-Condon simulations

The Franck-Condon approximation provides the basis for most theoretical models of vibrational-electronic (vibronic) spectroscopy as it provides a general approach to predicting the intensity of vibronic transitions. In this section, a conceptual explanation of the Franck-Condon principle is presented, followed by a derivation of the mathematical framework needed for the Franck-Condon principle and an introduction to the Franck-Condon Factors (FCFs) is given. Finally, the two computational methods used in this project to determine the Franck-Condon spectrum are discussed and brief introduction to the breakdown of the Franck-Condon model is initiated.

Conceptual framework of the Franck-Condon principle

The fundamental assumption of the Franck-Condon principle is that due to the instantaneous nature of photon absorption, an electronic excitation is likely to occur without a change in nuclear coordinates. Following the excitation event, the molecule's geometric structure may distort through motion initiated via vibrational modes. [41, 42] In order for this assumption to hold true, one must invoke the *Born-Oppenheimer approximation*. The Born-Oppenheimer approximation states that due to the mass difference between electrons and nuclei in a molecule, one can decouple the electronic and nuclear motion and consider them independently. This results in a framework that allows for one PES to be sufficient to describe a singular electronic state. It is important to note that the Born-Oppenheimer approximation, and consequently, the assumptions made for the Franck-Condon principle, are only valid if the excited state PESs are single character and define a single electronic state.

Prior to excitation, the molecule is most likely to be in the lowest energy vibrational level at the equilibrium ground state geometry, although FC excitations can be observed for higher energy vibrational states.[44] Upon excitation, the molecule is excited to a higher electronic excited state. As previously described, the photon absorption and excitation event occurs during a shorter time-span than nuclear motion. Therefore, the geometric structure of the molecule immediately before and immediately after the excitation is approximately the same. Consequently, one can visually represent this transition by drawing a vertical line upwards from the ground state PES at the equilibrium geometry to the excited state PES; this type of transition is denoted as a vertical transition, as depicted in Figure 2.6.[44] The transition is the most intense where the vibrational wavefunctions of the ground state and excited state will have the highest degree of overlap, and is therefore

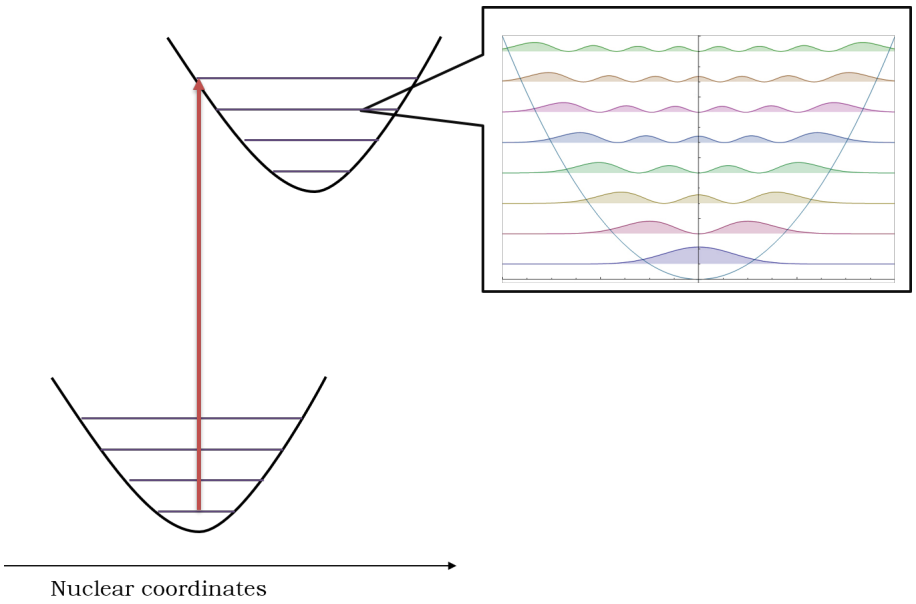

Figure 2.6: A schematic illustration of the Franck-Condon Principle. The PESs are modelled using the harmonic approximation. The vibrational wavefunctions are shown to be sinusodial functions.Modified from [43].

denoted the *Franck-Condon point*. [44] It is important to note that although the intensity of the transition will be highest at the Franck-Condon point, all vibrational energy levels in the surrounding area will have some transition probability as a result of having appreciable probability at being at the equilibrium geometry as well. This region is named the *Franck-Condon region*. In other words, transition intensities are strongest for vibrational levels that minimize changes in geometry. [44]

In practice, the observed vibrational structure of the resulting spectrum depends largely on the relative displacement between the excited state and ground state PESs. Typically, excited state PESs tend to displace to longer equilibrium bond lengths due to the higher antibonding character in comparison to the ground state. [44]

Mathematical justification for vibrational overlap

Quantitatively, the probability of a vibronic transition is determined by its corresponding FCFs. Each state within a vibronic transition is comprised of an electronic contribution $\psi_{el}(r)$ and a vibrational contribution $\psi_{vib}(R)$, forming a state $\Psi_{total}(r, R) = \psi_{el}(r)\psi_{vib}(R)$. [44] An optical excitation is dictated by the transition dipole moment μ:

$$\mu_{2,1} =< 2|\hat{\mu}|1 > \tag{2.9}$$

where 2 denotes the final state and 1 denotes the initial state and $\hat{\mu}$ is the dipole moment operator. The dipole moment operator can be expressed as:

$$\hat{\mu} = -e\sum_i r_i + e\sum_j Z_j R_j \tag{2.10}$$

where e is the charge of an electron, Z is the nuclear charge, and r_i, R_j are the distance from the centre of charge for the i^{th} electron and the j^{th} nucleus, respectively. By substituting the expression for $\hat{\mu}$ from equation 2.9 into 2.8, one obtains[44]:

$$\begin{aligned}
\mu_{2-1} =& < \psi_{el2}\psi_{vib2}| - e\sum_i r_i + e\sum_j Z_j R_j |\psi_{el1}\psi_{vib1} > \\
\mu_{2-1} =& -e\sum_i < \psi_{el2}|r_i|\psi_{el1} >< \psi_{vib2}|\psi_{vib1} > + \\
& e\sum_j Z_j < \psi_{el2}|\psi_{el1} >< \psi_{vib2}|R_j|\psi_{vib1} >
\end{aligned} \tag{2.11}$$

Where ψ_{el1} and ψ_{el2} represent the wavefunctions for two different electronic states and ψ_{vib1} and ψ_{vib2} represent the wavefunction for two different vibrational states. By the orthonormality principle, the integral of any two different wavefunctions is zero. Therefore, the second term is equal to zero. By defining the overlap integral as S, one determines that:

$$\mu_{2-1} = \mu_{electronic} S(vib2, vib1) \tag{2.12}$$

The term $\mu_{electronic}$ is the electric dipole moment of the transition that arises from the redistribution of electrons, and $S(vib2, vib1)$ is the vibrational overlap between the final and initial vibrational levels. Since the intensity of a given transition is proportional to the square modulus of the dipole moment, $|\mu_{2-1}|^2$, it can be concluded that the transition

intensity is also proportional to the square of the overlap integral $|S(vib2, vib1)|^2$, named the FCF. The greater the vibrational overlap, the higher intensity the vibronic transition will be.

Computational realization

The Franck-Condon principle offers an alternative method in obtaining information regarding the geometric structure of excited electronic states due to the dependency of vibronic band intensity on geometric structure.[45] As such, it can be used to predict or determine the excited state structures of molecules. [45]

For a large molecule comprised of 10-100s of atoms, a full computational characterization of the PES through electronic structure calculations is too computationally expensive. Therefore, the PES must be constructed using a Taylor series expansion.[46] Typically, for molecular PESs, a quadratic expansion is the lowest order expansion that gives acceptable accuracy, commonly referred to as the harmonic approximation.[46] The most challenging aspect of producing the Franck-Condon spectrum is determining a suitable model for the excited state surface; many models are available to provide a suitable PES. In this section, the two methods that were used in the course of this project will be covered: the adiabatic Hessian (AH) and vertical gradient (VG) Franck-Condon calculation. A diagram illustrating both models can be found in Figure 2.7.

Before addressing the differences between the models, the similarities between the two approaches will be highlighted. In both the AH and VG models, the ground state PES is defined using the harmonic approximation. Within the scope of molecular modelling, this entails performing a geometry optimization to find the equilibrium geometry and per-

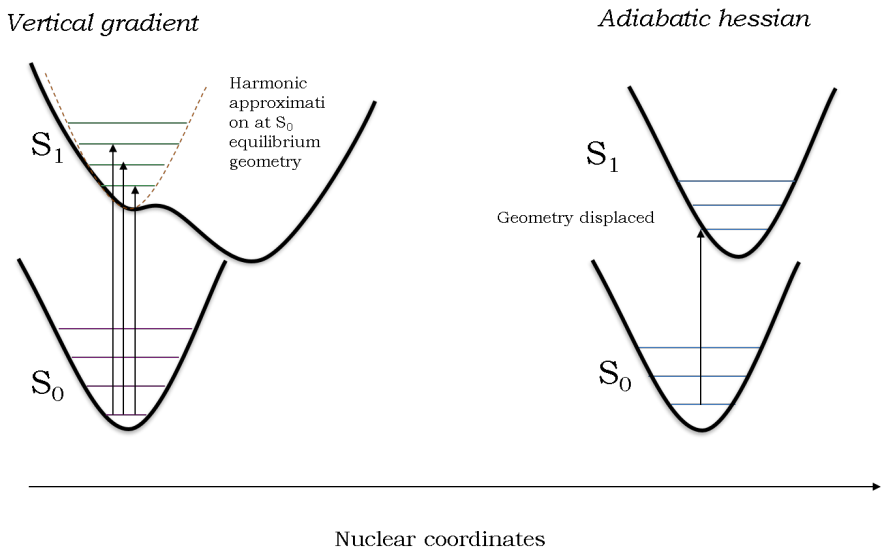

Figure 2.7: Comparison between adiabatic Hessian and vertical gradient Franck-Condon models. In both scenarios, the ground state PES is modelled as being harmonic. In the vertical gradient approximation, the potential energy surface of the excited state is artificially created by a Taylor expansion around the ground state equilibrium geometry (dotted lines). In the adiabatic hessian model, the real excited state potential energy surface is found at the excited state equilibrium geometry and using the harmonic approximation for those respective nuclear coordinates. Adapted from Santoro et al.[46]

forming normal mode analysis to define the vibrational frequencies and ultimately the Hessian.[46] However, AH and VG differ significantly when it comes to how the excited state PES is defined.

In the AH picture, the procedure follows a direct depiction of the Franck-Condon principle defined previously. The excited state PES is fully defined by its equilibrium geometry and normal modes.[46] While this provides the results closest to the actual Franck-Condon theoretical framework, it poses numerous limitations. Such limitations include the possibility of excitation events occurring at a geometry that differs significantly from the equilibrium geometry and the increasing difficultly in optimizing on excited state surfaces when other excited state phenomena (such as conical intersections and intersystem crossings) are present.

In contrast, the VG Franck-Condon procedure does not require the optimization of the exact excited state PES. In this approach, the excited state is assumed to have the same Hessian as the ground state, meaning that they have the same normal modes and frequencies. Only the equilibrium geometry gets displaced.[46] In other words, a second order Taylor expansion is performed at the equilibrium geometry (FC point) and linearly shifted upwards to reach the excited state PES. The Hessian of the excited state PES is assumed to be the same as the ground state PES, and therefore, only the new excited state gradient is calculated.[47, 48] Between the traditional AH Franck-Condon approach and the VG Franck-Condon, the VG Franck-Condon is expected to provide a better description of broad spectral features such as the position of the intensity maximum and qualitative pictures of the vibronic envelope. [47]

Franck-Condon limitations

It is important to emphasize that all Franck-Condon calculations are based on the Born-Oppenheimer approximation. The Born-Oppenheimer approximation is accurate in cases when the excited state energies are well separated, meaning that they are separated farther in energy than the nuclear motion initiated by vibrational modes. [49] In systems where the excited state changes character along its gradient, such as crossing to other surfaces via conical intersections, the Born-Oppenheimer approximation breaks down.[49] In these instances, it is more appropriate to use a model that does not assume separation of the electronic and nuclear degrees of freedom. A common choice is the use of a linear vibronic coupling Hamiltonian.[50, 49] In this picture, the PESs are written in a diabatic basis set [49], inherently capturing their multicharacter nature. A detailed description of the breakdown of the Born-Oppenheimer approximation, the need for a diabatic basis set, and generation of vibronic spectra using a linear vibronic coupling Hamiltonian can be found in Chapter 3: Theoretical framework.

Chapter 3

Theoretical framework

In this chapter, a mathematical derivation of the Born-Oppenheimer approximation is provided and the breakdown of the Born-Oppenheimer approximation is discussed. The transformation from an adiabatic to diabatic basis set is demonstrated, and a derivation of the non-adiabatic coupling parameters is shown. Finally, a derivation of the linear-coupling vibronic Hamiltonian is performed, and a brief overview of the multi-configurational, time-dependent Hartree (MCTDH) method to generate vibronic spectra will be presented.

3.1 Born-Oppenheimer approximation

The Born-Oppenheimer (BO) approximation is perhaps the most fundamental concept underlying modern chemical theory. In addition, the idea that nuclear dynamics occurs on a single electronic surface simplifies the study of excited states and provides the framework for most theoretical investigations of molecular spectroscopy, including the Franck-Condon principle. [44, 51]

Conceptually, the BO approximation proposes that owing to the difference in mass between

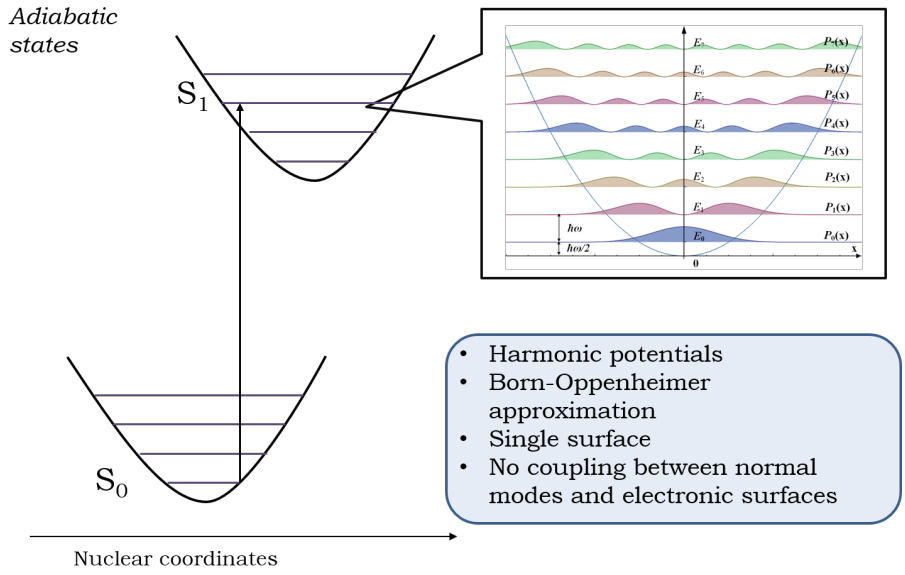

Figure 3.1: Schematic depiction of BO states. Modified from [43].

nuclei and electrons, their respective motion occurs on different timescales. Consequently, the motion of the nuclei is much slower than that of the electrons, such that one can consider the nuclei to be stationary. As a result, the electrons are treated as following the nuclei instantaneously as their configuration (*molecular geometry*) changes. One can solve the electronic Schrödinger equation for the electronic wavefunction Ψ_{el} consisting of solely electronic contributions at a selected geometry and obtain the energy. This framework is often referred to as the *clamped nuclei approximation*. Exploring how the electronic energy of the system changes as a function of geometry distortion creates a potential energy surface (PES), as shown in Figure 3.1. The PES is one of the most important concepts in chemistry, as it often is the starting point for understanding molecular spectroscopy and reaction kinetics.[44] In this section, a formal derivation of the BO approximation is provided. Unless otherwise stated, the derivations shown in this section follow the protocols

performed in the following references: [52, 53, 54, 55].

3.1.1 Clamped nuclei approximation and inclusion of nuclear movement

The full molecular Schrödinger equation is given by:

$$\hat{H}(\vec{r},\vec{R})\Psi_n(\vec{r},\vec{R}) = E_n\Psi_n(\vec{r},\vec{R})$$

where the molecular Hamiltonian $\hat{H}$ is comprised of nuclear and electronic contributions to the kinetic and potential energies, represented by nuclear and electronic coordinates $\vec{R}$ and $\vec{r}$ respectively. The molecular Hamiltonian takes the form of :

$$\hat{H} = \hat{T}_N + \hat{T}_e + \hat{V}_{ee} + \hat{V}_{Ne} + \hat{V}_{NN}$$

Where $\hat{T}_N$ and $\hat{T}_e$ are the kinetic energy operators of the nuclei and electrons, respectively and $\hat{V}_{Ne}$, $\hat{V}_{ee}$ and $\hat{V}_{NN}$ are the potential energy operators for nuclei-electrons, electron-electron, and nuclear-nuclear interactions. $\hat{H}$ can be simplified by defining the electronic Hamiltonian $\hat{H}_{el}$ as:

$$\hat{H}_{el} = \hat{T}_e + \hat{V}_{ee} + \hat{V}_{Ne} + \hat{V}_{NN}$$

$$\hat{H} = \hat{T}_N + \hat{H}_{el}$$

Thus, the Schödinger can be written as:

$$(\hat{T}_N + \hat{H}_{el})\Psi_n(\vec{r},\vec{R}) = E_n\Psi_n(\vec{r},\vec{R}) \tag{3.1}$$

The first step in order to arrive at the BO approximation is to evaluate the electronic component $\hat{H}_{el}$. This can be accomplished by solving the Schrödinger equation at a fixed

geometry R. As a result of keeping the nuclei static, $\hat{T}_N$ becomes 0. As such, the electronic wavefunction for a given electronic state can be written as, ϕ_λ^{el} which is an eigenfunction of $\hat{H}_{el}$. This step in the BO approximation is called the clamped nuclei approximation. The clamped nuclei Schrödinger equation becomes:

$$\hat{H}_{el}(r;R)\phi_\lambda^{el}(\vec{r};\vec{R}) = E_\lambda(R)\phi_\lambda^{el}(\vec{r};\vec{R}) \tag{3.2}$$

Where $\phi_\lambda(\vec{r};\vec{R})$ is a function of the electronic coordinates $\vec{r}$ at a given parameter of $\vec{R}$, the nuclear coordinates. $\phi_\lambda(\vec{r};\vec{R})$ forms an orthonormal basis set such that the condition $\int \phi_\mu^*(\vec{r};\vec{R})\phi_\lambda(\vec{r};\vec{R})d\vec{r} = \delta_{\mu\lambda}$ is satisfied. In this notation, commas within the function argument indicate two dependent variables, whereas a semicolon indicates the first term is a variable and the second term is a constant parameter.

Next, the nuclear kinetic component $\hat{T}_N$ can be incorporated assuming that the information regarding the motion of the electrons is encoded into the PES. The exact eigenstates of the molecular Hamiltonian can be found by summing over electronic states via the so-called *Born-Huang expansion*:

$$\Psi_n(\vec{r};\vec{R}) = \sum_\lambda \phi_\lambda^{el}(\vec{r};\vec{R})\chi_\lambda(\vec{R}) \tag{3.3}$$

It is important to note that Ψ is dependent on the nuclear positions, but not the nuclear velocities. Now that the mathematical framework for the electronic solution has be provided,one can arrive at the BO approximation by directly evaluating the Schrödinger equation with the wavefunction defined by equation 3.3:

$$(\hat{T}_N + \hat{H}_{el})\sum_\lambda \phi_\lambda^{el}(\vec{r};\vec{R})\chi_\lambda(\vec{R}) = E_n(\vec{R})\sum_\lambda \phi_\lambda^{el}(\vec{r};\vec{R})\chi_\lambda(\vec{R}))$$

Recall that $\hat{T}_N = \frac{1}{2M_a}\nabla_a \cdot \nabla_a$. Thus, the equation becomes:

$$(\frac{1}{2M_a}\nabla_a \cdot \nabla_a + \hat{H}_{el}) \sum_\lambda \phi_\lambda(\vec{r};\vec{R})^{el}\chi_\lambda(\vec{R}) \tag{3.4}$$

Expanding the full Hamiltonian and remembering that:

$$\hat{H}_{el} \sum_\lambda \phi_\lambda^{el}(\vec{r};\vec{R})\chi_\lambda(\vec{R}) = \sum_\lambda E_\lambda(\vec{R})\phi_\lambda^{el}(\vec{r};\vec{R})\chi_\lambda(\vec{R}))$$

generates the following terms:

$$\sum_a \frac{1}{2M_a}\{\sum_\lambda [\chi_\lambda(\vec{R})\nabla_a^2\phi_\lambda(\vec{r};\vec{R}) + \phi_\lambda(\vec{r};\vec{R})\nabla_a^2\chi_\lambda(\vec{R}) \tag{3.5}$$

$$+ \nabla_a\phi_\lambda(\vec{r};\vec{R})\nabla_a\chi_\lambda(\vec{R}) + E_\lambda(\vec{R})\phi_\lambda(\vec{r};\vec{R})\chi_\lambda(\vec{R})\} \tag{3.6}$$

Where a labels the nuclei and λ labels the electronic states. By integrating against a different electronic eigenstate, $\phi_\mu(\vec{r},\vec{R})$ one can take advantage of orthonormality at a given $\vec{R}$, yielding:

$$\sum_\lambda \quad \Big[\int \phi_\mu(\vec{r};\vec{R}) \sum_a \frac{1}{M_a}\nabla_a^2\phi_\lambda(\vec{r};\vec{R})d\vec{r}\}\chi_\lambda(\vec{R}) \qquad \textbf{A}$$

$$+ \delta_{\mu\lambda}\sum_a \frac{1}{2M_a}\nabla_a^2\chi_\lambda(\vec{R}) \qquad \textbf{B}$$

$$+ \sum_a \{\int \phi_\mu(\vec{r},\vec{R})\nabla_a\phi_\lambda(\vec{r};\vec{R})d\vec{r}\}\frac{-1}{M_a}\nabla_a\chi_\lambda(\vec{R}) \qquad \textbf{C}$$

$$+ \delta_{\mu\lambda}E_\lambda(\vec{R})\chi_\lambda(\vec{R})\Big] \qquad \textbf{D}$$

The BO approximation is obtained by truncating the expansion to a single state and

calculating its projection. (IE setting μ=λ). In this scenario, Term **C** vanishes due to the set of wavefunctions being normalized:

$$\begin{aligned}
&\int \phi_\lambda(\vec{r},\vec{R})\nabla_a\phi_\lambda(\vec{r},\vec{R})d\vec{r} \\
&= \frac{1}{2}\nabla_a \int \phi_\lambda(\vec{r},\vec{R})\phi_\lambda(\vec{r},\vec{R})d\vec{r} \\
&= 0
\end{aligned}$$

Similarly, Term **A** is denoted the diagonal Born-Oppenheimer correction, and it is sufficiently small that it neglected in most calculations. Only the **B** and **D** terms are left to be considered, resulting in the BO approximation Schrödinger equation:

$$(\hat{T}_N + E_\lambda(\vec{R}))\Psi_{\lambda,n}(\vec{R}) = E_n\Psi_{\lambda,n}(\vec{R}) \tag{3.7}$$

where λ denotes the electronic states, N labels the nuclear coordinates, and n labels the rotational-vibrational levels. $E_\lambda(\vec{R})$ represents a point on a, in general, complicated surface called the PES. It is clear that for a given geometry, each individual electronic state represented by Ψ yields an individual PES point $E_\lambda(R)$ as $\vec{R}$ varies. The clamped nuclei approximation implies that one can solve the Schrödinger equation for every possible geometry $\vec{R}$. It can be stated that for a unique geometry $\vec{R}$, one potential energy point is enough to describe a given electronic state. When these surfaces are obtained using the clamped nuclei approximation, they are denoted as *adiabatic* surfaces.[52, 54]. By solving for the rovibrational states under this approximation, one arrives at the *Born-Oppenheimer approximation.*

3.2 Expanding beyond BO

The BO approximation provides a suitable framework for systems where the nuclear dynamics occur predominately on a single surface. Typically, this occurs when the spacing between electronic states is large with respect to the vibrational energy spacing. [53] The BO approximation typically breaks down under two conditions:

(1) When the spacing between electronic states is very small and comparable in magnitude to the spacing of the vibrational levels (on the order of 0.1 eV)[49]

(2) When the character of the excited state rapidly changes upon geometry distortion. Such behaviour can be observed in regions where excited states interact, such as conical intersections.

Such scenarios are depicted in Figure 3.2. When an excited state cannot be accurately

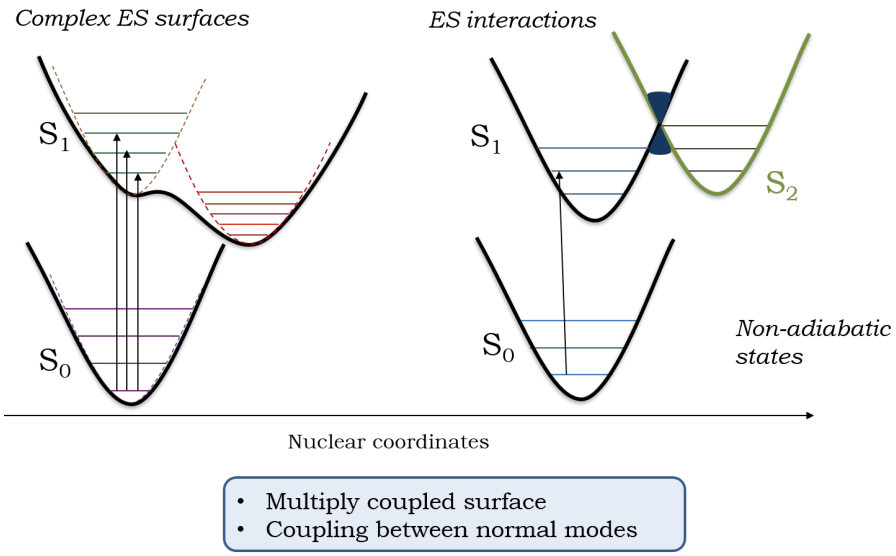

Figure 3.2: Schematic of non-adiabatic interactions and complicated PESs

modelled by a single PES, the excited states need to be defined as a linear combination

of multiple excited states within the system. The neglected terms **A** and **C** in the BO framework described in section 3.1 become increasingly important and must be calculated. However, scenarios that satisfy conditions (1) and (2) make it difficult to evaluate **A** and **C**, since derivatives with respect to nuclear coordinates would vary greatly due to the rapidly changing character of the states. First, consider the term **A** in the expanded molecular Hamiltonian representation. Mathematically, term **A** can be represented as:

$$\mathbf{A} = \sum_{\lambda} \{ \int \phi_{\mu}(\vec{r}; \vec{R}) \sum_{a} \frac{1}{M_a} \nabla_a^2 \phi_{\lambda}(\vec{r}; \vec{R}) d\vec{r} \} \chi_{\lambda}(\vec{R}) \tag{3.8}$$

As shown, both derivatives act on the electronic wavefunction ϕ_{λ}. As this term is often small and of purely electronic nature, term **A** is often referred to as the Born-Oppenheimer Correction. One can see that if the basis is truncated to a single surface by setting $\mu = \lambda$, the term would be diagonal. [55] Now, consider the term **C**, which is mathematically defined as:

$$\sum_{a} \{ \int \phi_{\mu}(\vec{r}; \vec{R}) \nabla_a \phi_{\lambda}(\vec{r}; \vec{R}) d\vec{r} \} \frac{-1}{M_a} \nabla_a \chi_{\lambda}(\vec{R})$$

This term in the expanded Schrödinger equation is called derivative coupling. These terms involve off-diagonal contributions called vibronic coupling or non-adiabatic effects. Vibrational-electronic, or vibronic, coupling refers to couplings that arise between electronic states through the vibrational normal modes. Typically, one considers vibronic couplings that may arise from the equilibrium geometry and normal modes, as well as couplings that may become allowed upon geometric distortion and symmetry breaking.[52, 53] The complexity of calculating term **A** and **C** in strongly coupled states arises from the fact that **A** and **C** are not smooth functions with respect to the nuclear coordinates.

In order to get around this limitation, one can choose a different basis set to represent

the electronic wavefunctions. Instead of choosing ones that are eigenfunctions of the electronic Hamiltonian, one can select a basis that minimizes the derivative coupling term. In other words, one can use a basis set that is multi-character in nature. In this section, the transformation from a single character basis set (adiabatic) to a multi-character basis set (diabatic) will be discussed. Afterwards, a discussion on how one can evaluate the remaining terms in the Hamiltonian will be presented.

3.2.1 From adiabatic to diabatic states

Recall that the clamped nuclei approximation assumes that the set of $\phi_\lambda(\vec{r};\vec{R})$ are eigenfunctions of the electronic Hamiltonian $\hat{H}_{el}$ for a chosen set of nuclear coordinates $\vec{R}$ and these states are called *adiabatic states*. While investigating the improvements to the BO approximation by looking at the other two terms **A** and **C**, one can create an analysis based on a linear combination of these adiabatic states, called *diabatic states*. These diabatic states are constructed under the constraint that the character of the diabatic states do not vary significantly along the nuclear coordinates. Mathematically, this constraint is defined as:

$$\int \psi_i^* \nabla_a \phi_i dr = 0 \tag{3.9}$$

Where i and j label different diabatic states. The computational method used to construct these diabatic states is called the *diabatization scheme*. In most diabatization schemes, one identifies an initial geometry R_0 where the adiabatic and diabatic states coincide. An electronic structure calculation is performed at a given geometry R to obtain the adiabatic states. A unitary operator $U(R)$ that rotates adiabatic electronic states $\phi_{ad}(\vec{r},R)$ into diabatic states $\phi_{dia}(\vec{r},R)$ is applied. $U(R)$ is selected such that the constraint defined by Equation 3.9 is most satisfied:

$$\begin{pmatrix} \psi_i(\vec{r};R) \\ \psi_j(\vec{r};R) \end{pmatrix} = U(R) \begin{pmatrix} \phi_\lambda(\vec{r};R) \\ \phi_\mu(\vec{r};R) \end{pmatrix} \tag{3.10}$$

Typically, determination of $U(R)$ begins by defining the ground state PES using the equilibrium molecular geometry $\vec{R}_0$ and normal mode coordinates q_i. This information is obtained from electronic structure calculations. Then, the adiabatic states are determined by running an excited state calculation, such as TD-DFT, on at $\vec{R}_0$:

$$[\phi_\lambda(R=0)\rangle = \left[\phi_\lambda^0\right\rangle$$

Afterwards, small positive and negative displacements $\vec{R}_0 + \delta q_i$ along each normal mode coordinate are made. At each new geometry R_i, the adiabatic excited states are recalculated $[\phi_\lambda(\delta q)\rangle$. The overlap matrix $S_{\lambda\mu}$ is calculated for states at different geometries:

$$S_{\lambda\mu} = \int \phi_\lambda(\vec{r}, \vec{R_0}) \phi_\mu(\vec{r}, R_0 \vec{+} dq_i) \tag{3.11}$$

A unitary transform $U_{\lambda j}(R_i)$ is selected such that the transformed overlap matrix, $\sum_\mu S_{\lambda\mu}(R_i) U_{\mu j}(R_i) = \tilde{S}_{\lambda \mathrm{J}}(R_i)$ is diagonal. The diabatic states follow:

$$\phi_j(\vec{r}, \vec{R}_0 + \delta q_i) = \sum_\lambda \phi_\lambda(\vec{r}, \vec{R}_0 + \delta q_i) U_{\lambda j}(R_i) \tag{3.12}$$

The new transformed diabatic states achieve maximum overlap with their respective adiabatic states at R_0.

Once $U(R)$ is determined, the full molecular Hamiltonian is expanded in this new diabatic basis set by a unitary transformation:

$$U^\dagger(R) \hat{H}_{adiabatic} U(R) = \hat{H}_{diabatic}$$

Similarly, one can transform the diagonal adiabatic electronic energy matrix into the diabatic representation and a potential energy matrix is obtained:

$$E_{ab}(R) = \sum_{\lambda} U_{\lambda a}(R) E_{\lambda} U_{\lambda b}(R) \tag{3.13}$$

Here, a and b label diabatic electronic states, while λ labels an adiabatic electronic state. In the diabatic basis set, the non-adiabatic coupling terms from term $\mathbf{C}$ vanish. From here, one can easily resolve the coupling terms and begin to build the vibronic Hamiltonian.
It is interesting to note that the diabatic states are often much simpler to model than the associated adiabatic states. In Figure 3.3, a comparison between the adiabatic (V) and diabatic (E) states for the same two level system is show. The diabatic surfaces are much smoother than the adiabatic states.

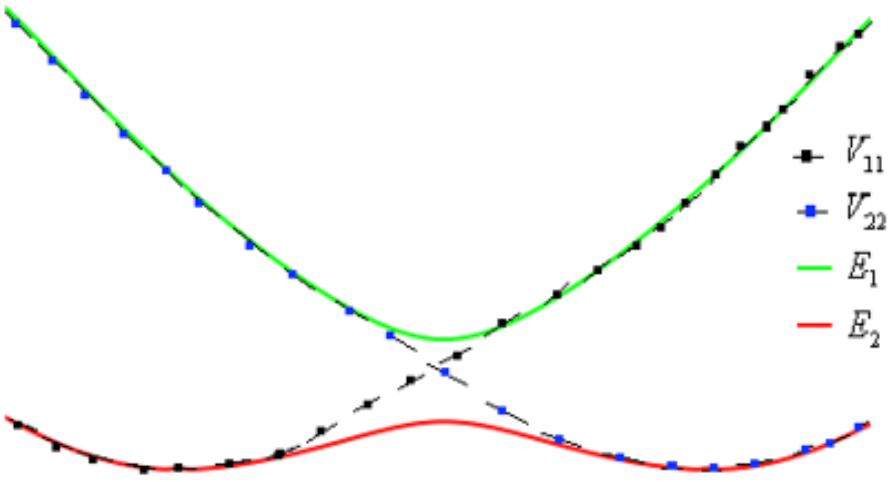

Figure 3.3: Comparison of two states obtained from an arbitrary 2D Hamiltonian in the adiabatic (V) and diabatic (E) representation.[56]

3.2.2 Building a vibronic model Hamiltonian

One can obtain the vibronic coupling constants by performing a Taylor series expansion of the potential energy matrix [54]:

$$V_{ab}(q_i) = \delta_{ab}E_{ab} + \sum_{i}^{m} E^{i}_{ab}q_i + \frac{1}{2}\sum_{i>j}^{m} E^{ij}_{ab}q_iq_j... \tag{3.14}$$

Where a and b label diabatic electronic states and i and j label normal modes up to m. One can obtain the Taylor series coefficients for the first term in the expansion, E_{ab}, for a given normal mode using numerical derivatives:

$$E^{i}_{ab} = \frac{E_{ab}(R_o + \delta R_i) - E_{ab}(R_o - \delta R_i)}{2\delta R_i} \tag{3.15}$$

It is important to highlight that equation (2.2.7) contains the first-order correction, or linear term. Higher order corrections can be derived using a similar method and high-order Taylor expansions. Such methods and protocols have been described in detail in the literature, such as the construction of a quadratic vibronic Hamiltonian [51]. In the context of this project, the vibronic model used only employs linear coupling terms.

There are three main advantages to using a vibronic model to model non-adiabatic dynamics and processes:

(1) It provides the simplest way to go beyond the BO approximation and obtain coupling between electronic and nuclear degrees of freedom.

(2) It provides an effective way to model conical intersections since the multi-character nature is inherent to diabatic states.

(3) By diagonalizing the diabatic Hamiltonian $\hat{H}_{diabatic}$, one can predict the adiabatic po-

tentials and surfaces with a high degree of accuracy since a multi-character representation naturally captures anharmonicities. This is shown in Figure 3.4.

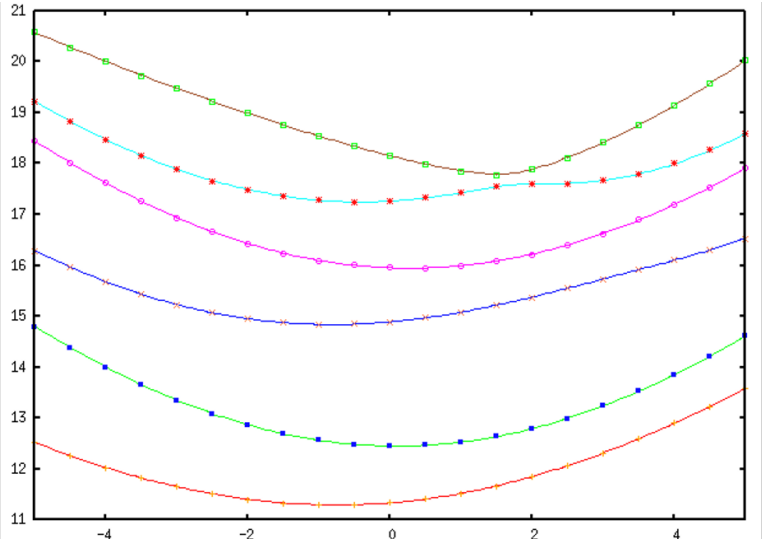

Figure 3.4: Comparison between adiabatic surfaces determined using the vibronic model vs BO electronic structure calculations. Solid lines represent the adiabatic surfaces determined by diagonalizing the vibronic Hamiltonian. Dotted points represent the actual clamped nuclei calculation determined at the IP-EOM-CCSD level of theory. The PES used is for formic acid along its fourth normal mode.[56]

3.3 Generating spectra with MCTDH

Once the vibronic model Hamiltonian has been determined, one can use multi-configurational, time-dependent Hartree (MCTDH) framework to account for time propagation and fold in real-time dynamics.

MCTDH is an algorithm to solve the time-dependent Schrödinger equation for many-body

systems using wavepacket propagation. [57, 58] In the wavepacket ansatz, the wavefunction Ψ is characterized as a product expansion of time-dependent, single particle functions. Using this ansatz, one can find a variational solution to the time-dependent Schrödinger by using a set of coupled equations. [59]

Once the Schrödinger equation has been solved, the autocorrelation function is determined. In the Heisenberg picture of spectroscopy, the time evolution of the system is considered and the total spectrum is determined by the Fourier transform of the time-correlation function. [60] The time-correlation function provides a statistical representation of how two dynamic properties are coupled as a function of time and it describes how a long certain property of the system (such as excitations) exist until it is dominated by molecular motion.[60] In general, the correlation function can be written as:

$$C_{\alpha\beta}(t) =< \alpha(o)\dot{\beta}(t) >_o \tag{3.16}$$

Where α and β represent two different dynamic properties of the system. The $<>_o$ indicates that the average is being performed at a reference time $t = 0$. When the correlation function is written as two different dynamic properties, as shown above, it is denoted the cross-correlation function, whereas if the two properties being evaluated are the same. such as $C_{\alpha\alpha}$, is denoted the autocorrelation function. In the case of vibronic spectroscopy, the spectrum is generated by the Fourier transform of the dipole moment autocorrelation function for the absorbing species. [60] In the context of this project, the autocorrelation function is defined as:

$$C(t) =< \Psi_o|\hat{\mu}e^{-i\hat{H}t}\hat{\mu}|\Psi_o > \tag{3.17}$$

where $\hat{\mu}$ is the dipole operator, $\hat{H}$ is the vibronic model Hamiltonian, and Ψ_o is the initial state of the absorbing species. This autocorrelation function is Fourier transformed into

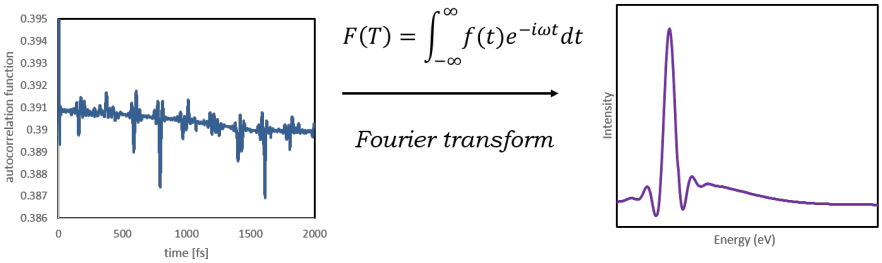

Figure 3.5: Transforming from autocorrelation to spectrum

frequency domain, to obtain a vibronic spectrum as demonstrated in Figure 3.5.

A detailed account of all calculation parameters, wave-packet propagator and Fourier transform conditions, as well as exact methodology used is found in the corresponding results chapters. A description of the exact protocol being used to generate the vibronic models used in this project can be found in Appendix A.

Chapter 4

Gas-phase separation and spectroscopic identification of beer bittering molecules

In this chapter, DMS-MS coupled with UVPD is explored as a potential alternative method to identify and quantify bittering molecules present in beer. First, the clustering behaviour under different DMS-MS conditions and environments are determined for deprotonated humulone and deprotonated isohumulone. Once the DMS-MS parameters are optimized to induce maximum separation between species of interest, deprotonated humulone and isohumulone are subjected to UVPD action spectroscopy experiments and their vibronic spectrum are analyzed. Key differences in the vibronic spectrum of deprotonated humulone and isohumulone are shown, thus validating the concept of using DMS-MS-UVPD in this application.

4.1 Introduction

Beer is among the most consumed alcoholic beverages in the world. The flavour profile - its unique combination of aroma and taste impressions - is a major factor in consumer acceptance.[20] Amongst the flavour profiles concerning the taste of beer, bitterness acts as a crucial contributor.[21] It is beneficial for breweries to accurately describe the bitterness of their product for both quality assurance and new product development. A beer's overall bitterness is intimately tied to the number of bittering compounds present and their ratios. While the overall bitterness is a result of a mixture of all brewing ingredients, approximately eighty percent of the bitterness profile is determined by the addition of hops (*Humulus lupulus*) during the brewing process.[21, 22] Hops are rich in α-acids, a family of compounds that thermally isomerize into the bitter-tasting iso-α-acids during wort boiling.[21, 22, 61]

α-Acids in hops are resinous constituents found in the female flower.[63] Comprised of homologues and isomers of humulone, approximately ninety-eight percent of total α-acids in hops are found as three major congeners: humulone, adhumulone, and cohumulone.[64] As is shown in Figure 4.1, humulone and adhumulone are regioisomers, differing solely in the position of a methyl group. Similarly, cohumulone is a homologue of humulone, containing the same base structure, but differing in the length of one sidechain. While the α-acids are precursors to the iso-α-acids, they themselves are tasteless.[65] During the beer boiling process, the tasteless α-acids undergo thermal isomerization into epimeric pairs of flavourful bitter iso-α-acids.[21, 22, 61] The proposed isomerization mechanism of α-acids to iso-α-acids proceeds via an acyloin rearrangement, transforming from a six-membered ring to a five-membered ring structure.[61, 65] For each α-acid species, *cis* and *trans* iso-

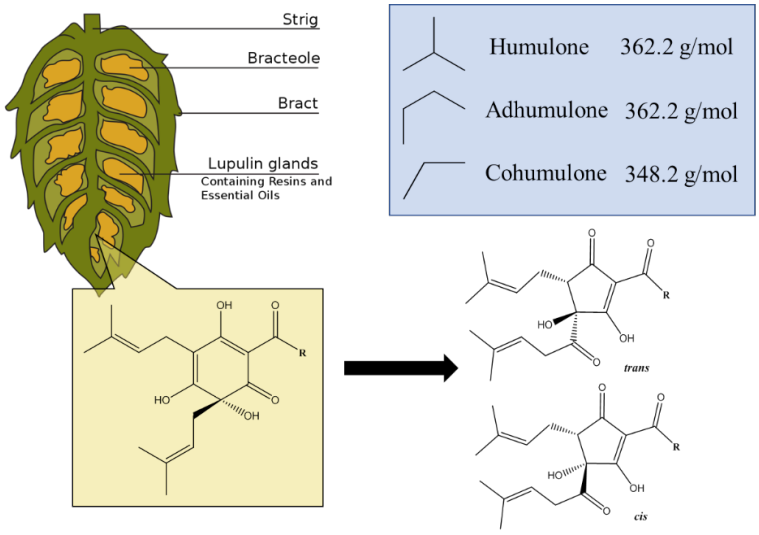

Figure 4.1: The α-acids and their respective isomers. R represents the side chain that is associated with each homologue. Modified from [62].

mers are created. The proposed reaction mechanism is illustrated in Figure 4.2. [22]

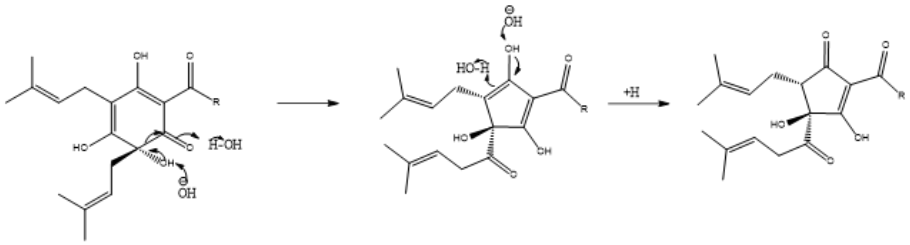

Figure 4.2: Acyloin rearrangement of α-acids into iso-α-acids.

Experimental work conducted by Jaskula et al. reveals that iso-α-acid formation follows first order kinetics, signifying that the amount of iso-α-acid formation is proportional to the initial α-acid content.[61] Utilization refers to the fraction of available α-acids that are converted into iso-α-acids.[22] In conventional brewing, the α-acid utilization plateaus

around 25-35% .[22] The cause of the poor isomerization yield is attributed to low solubility of α-acids in beer, incomplete isomerization due to insufficient boiling time, and depletion of α-acid and iso-α-acid content.[61] Additionally, final utilization is dependent on a plethora of solution properties such as pH, boil duration, and temperature.[61] Efforts to improve the final utilization is an active research area, with advances including the use of a metallic isomerization catalyst, increasing solution alkalinity, and incorporating oxidization products of the bitter acids into the brew.[22, 61, 65]

The isomerization process yields six major congeners; trans and *cis* stereoisomers of isohumulone, isoadhumulone, and isocohumulone. The formation of cis or trans isomers occurs at a ratio of approximately 7 : 3, respectively.[65, 66] Due to a reduction in steric hindrance, the *cis* isomer is thermodynamically more stable than its *trans* counterpart.[67]

Not only do different iso-α-acid congeners elicit a different bittering potency, but so do different stereoisomers derived from the same α-acid species.[65] In a series of organoleptic studies, it was reported that the *cis* congener is substantially more bitter than its *trans* counterpart, and isohumulone is more bitter than iso-cohumulone.[22] Each iso-α-acid plays a discrete role in the perceived bitterness of a beer, and therefore, an accurate portrayal of beer bitterness needs unique identification of each iso-α-acid.

Despite the variety of iso-α-acid species, most methods currently established only quantify total iso-α-acid count. The international bitterness unit (IBU) relies on ultraviolet-visible (UV-Vis) spectrophotometry to quantify bitter acids and it is calculated using the following formula[63]:

$$IBU = abs_{275} * 50 \tag{4.1}$$

While this technique provides a platform for measuring total bitterness, it is widely regarded as insufficient due to its inability to distinguish between separate iso-α-acids.[65, 16, 68] In fact, both the isohumulones and their tasteless α-acid counterparts exhibit absorption in the 275 nm regime, causing an artificial increase in the calculated IBU. Advances in iso-α-acid detection methods have been mainly focused on high-performance liquid chromatography (HPLC) coupled techniques, improving on the individual species identification.[65, 68] However, HPLC methods are extremely time inefficient and require the use of expensive standards to calibrate the column.[68] In this chapter, the use of DMS-MS coupled with UV-PD action spectroscopy to create a rapid identification protocol between iso-α-acids and α-acids is proposed, building on the work initiated by Zhang[69]. By finetuning the DMS-MS parameters to filter for a species of interest prior to irradiation, it is possible to directly probe the electronic structure, providing a method of exact species identification. The results of the UVPD studies will provide the framework to assess the validity of using gas phase electronic spectroscopy as a method for rapid bitterness quantification in beer. Deprotonated isohumulone and humulone are selected as the test isomer pair for this proof-of-concept study, owing to the fact that humulone is the most abundant α-acid congener found in hops. Aside from creating a method to draw distinction between species, UV-PD will provide insights into the electronic structure of these species and the first gas-phase electronic spectrum for deprotonated humulone and isohumulone will be reported.

4.2 Methods

4.2.1 Experimental methods

A SelexIon differential mobility spectrometer was used in tandem with a QTRAP 5500 mass spectrometer (SCIEX; Concord, ON), as described in detail in Chapter 2. ESI conditions were optimized to yield the desired parent ions. The exact ESI and DMS conditions used for each experiment can be found in Appendix B.

Analytical grade humulone (2 mg/mL in MeOH:H_2O solvent) was purchased from Carbosynth and additional humulone standard was synthesized by the Murphy group at the University of Waterloo and its structure verified using NMR spectroscopy. α-Acids and iso-α-acids extracts were obtained from Hopsteiner. Analytes were diluted to a concentration of 100 ng/mL in a 1 : 1 solution of MeOH:H_{2O} or ACN:H_2O prior to electrospraying.

Deprotonated humulone, *cis*-isohumulone, and *trans*-isohumulone were subjected to DMS-MS experiments by selecting the parent mass of m/z=361 in negative mode using enhanced product ion (EPI) mode in the mass spectrometer. It is important to note that standards of isohumulone were not readily available, therefore, experiments were conducted using a commercially available mixture of isomerized α-acids. However, due to the abundance of humulone found in hops compared to the other α-acid congeners, it is assumed that the major contribution to the m/z=361.2 parent mass in the iso-α-acid extract will be comprised of an ensemble of *cis* and *trans*-isohumulone.

DMS experiments were performed by ramping the SV from 0-4000 V. At each SV step, the CV is scanned in increments of 0.1 V to create an ionogram. In order to investigate the

clustering behaviour of each species, the obtained ionograms were used to create dispersion plots. A detailed description of DMS-based experiments can be found in Chapter 2. The experiments were first completed in a pure $N_{2(g)}$ environment, and then were repeated by seeding the collision gas with 1.5 % (v/v) of MeOH and IPA modifiers.

To facilitate photodissociation experiments, the DMS-MS apparatus was retrofitted with a window to allow for light from an Nd:YAG-pumped optical parameteric oscillator (OPO) as described in Chapter 2. Ion transmission maxima from the DMS-MS experiments were selected as SV/CV pairs and were held in an ion trap as they were irradiated by the OPO. The OPO was scanned in increments of 2 nm for a range of 208-400 nm in the case of deprotonated humulone and 208-360 nm in the case of deprotonated isohumulone. Parent and fragment ion intensities were monitored and recorded at each wavelength step and their relative intensities were used to generate an action spectrum. The exact conditions used to obtain the action spectra are presented in Appendix B.

4.2.2 Computational methods

The global minimum deprotonation tautomers of humulone, *cis*-isohumulone, and *trans*-isohumulone were selected according to the work by Zhang[69] and reoptimized at the CAM-B3LYP$/6-311++G(d,p)$ level of theory on Gaussian 16. Following optimization, normal mode analyses were performed to ensure that the structures lie on a minimum on the PES. In order to model excited states, the first fifteen vertical excitation energies were calculated for each species. CAM-B3LYP has been shown to provide more accurate excited state energies than conventional B3LYP due to the addition of a long-range correction.[70] Adiabatic Franck-Condon calculations were performed on Gaussian16 by

optimizing the ground state and the first six excited states of deprotonated humulone using the CAM-B3LYP/6311++G(d,p) level of theory. However, no vibronic progression was calculated between the ground state and excited states, signifying that vibronic activity occurs at a geometry far away from the Franck-Condon point. Therefore, the vertical gradient FC suit on ORCA 4.2.1 was used to generate theoretical spectra for experimental comparison. The FC overlap between the ground state S_0 and the first nine singlet excitations was calculated for each species and summed to create the overall vibronic spectrum. Protonated *cis*-isohumulone and *trans*-isohumulone spectra were combined to model the ensemble being probed. The *cis* to *trans* contributions were weighted according to their average abundance ratio after isomerization of $7:3$.[65, 66] Due to computational expense, calculations were performed at the CAM-$/6-311G$ level of theory. Vertical excitation energies obtained using CAM-B3LYP$/6-311++G(d,p)$ were compared to those obtained from CAM-B3LYP$/6-311G$ and minimal variation between basis sets was observed.

4.3 Results

4.3.1 DMS-MS experiments

Figure 4.3 shows the dispersion plots collected for a) deprotonated humulone and b) deprotonated isohumulone in a pure $N_{2(g)}$ environment, as well as gaseous environments seeded with 1.5% (v/v) of IPA and MeOH at low DMS temperature (150^oC). The deprotonated humulone data was collected by Zhang [69] using a dilution solvent of MeOH:H_2O in a $1:1$ ratio, whereas the isohumulone experiments were performed using a dilution solvent

of ACN:H_2O in a 1 : 1 ratio. The characteristic dispersion curve for the humulone standard was not observed in the iso-α-extract sample, indicating that humulone was not present in the Hopsteiner extract, therefore it is valid to consider both experiments individually. In the pure $N_{2(g)}$ environment, both deprotonated humulone and isohumulone exhibit hard sphere clustering. In the IPA seeded environment, both deprotonated humulone and isohumulone exhibit strong clustering behaviour, as expected. The strong solvent interaction can be attributed to the highly polarizable IPA molecules being attracted to the anion's negative charge. As an intermediate between $N_{2(g)}$ and IPA, MeOH modifier results in Type B behaviour for both deprotonated hunmulone and isohumulone, indicative of weak clustering. Interestingly, no evidence of separation of *cis* and *trans* isomers of isohumulone or separation of other iso-α-acid isobaric congeners, like isoadhumulone, are observed in the DMS-MS experiments. This is likely due to the extreme structural similarities among species and it is inferred that little to no change in CCS is observed. As a result, it is necessary to consider the probed ensemble as being comprised of a mixture of all isobaric species and tautomers. Due to the observance of strong clustering behaviour in both deprotonated

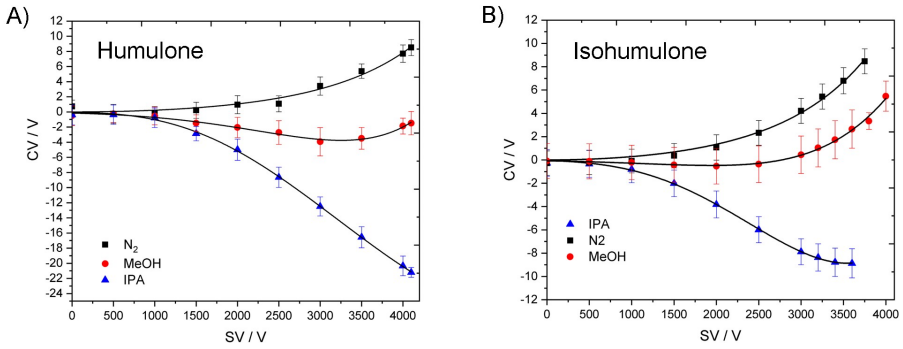

Figure 4.3: The dispersion plot for a) deprotonated humulone in $MeOH : H_2O$ solvent and b) deprotonated isohumulone in $ACN : H_2O$ solvent in $N_{2(g)}$, IPA, and MeOH modifiers.

humulone and isohumuloe, the use of an IPA seeded environment is a promising candidate for species specific selection prior to photodissociation experiments. Resulting from the fact that the dispersion plot data presented for humulone in Figure 4.3 was collected using a dilution solvent of MeOH:H_2O, the DMS-MS experiments were repeated using ACN:H_2O to provide an accurate comparison with the obtained results for deprotonated isohumulone. The results of the DMS-MS experiments for deprotonated humulone in ACN:H_2O are presented in Figure 4.4 and the ionograms obtained at an SV = 3600 V when selecting for m/z=361.2 in b) deprotonated humulone and c) deprotonated isohumulone are provided. It is important to note that while the dispersion plot in Figure 4.4a showcases two curves, the mass spectrum of the black curve does not contain the parent mass m/z=361.2, and therefore, is not considered to evolve from our ion of interest. When comparing the ionograms presented in Figure 4.4b and 4.4c, it is apparent that deprotonated humulone and isohumulone elute at significantly different CV, namely CV = -4 V for deprotonated humulone and CV = -9 V for deprotonated isohumulone.While the current experiments were not replicated using a mixture of deprotonated humulone and isohumulone, it can be inferred that the use of IPA modifier presents sufficient selectivity to separate between the isobars that are inseparable by traditional MS. Therefore, IPA modifier and the resulting clustering behaviour is used as the ion filter prior to irradiation by the OPO.

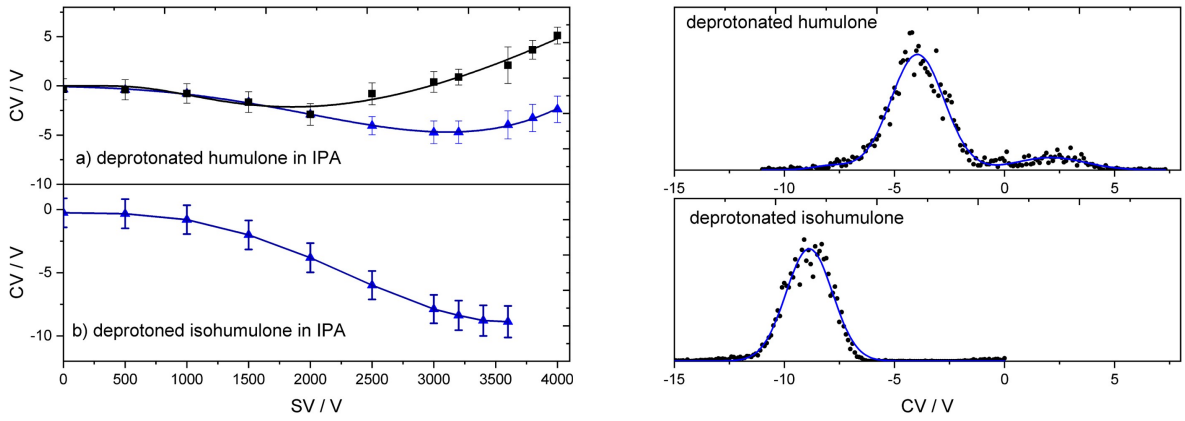

Figure 4.4: Right: Collected dispersion plot of a) deprotonated humulone and b) deprotonated isohumulone in IPA using ACN:H_2O solvent. Left: The ionogram collected in IPA modifier at SV = 3600 V for deprotonated humulone and deprotonated isohumulone in ACN:H_2O solvent.

4.3.2 Photodissociation experiments

Photodissociation experiments were performed on deprotonated humulone and deprotonated isohumulone in an IPA seeded environment using an SV = 3500 V.While higher SVs would likely result in an increase in difference between CVs needed to elute deprotonated humulone and isohumulone, an SV of 3500 V was selected to prevent high charge accumulation in the DMS cell resulting in electrical breakdown in the instrument. Photofragmentation spectra were collected using a modified version of enhanced multiply charged scan (EMC) mode. When using EMC mode, both deprotonated humulone and isohumulone show additional ionogram features and transmission maxima when compared to analogous experiments performed using EPI. Through an analysis of the fragmentation spectrum at each new ion transmission maxima, it was inferred that the new ionogram features result from a doubly charged parent dimer, and therefore, was excluded from further photodissociation analysis. The EMC ionograms and their resulting fragmentation spectrum of the additional ionogram features can be found in Appendix B. The effects of using modified EMC are still unclear and further investigation is needed to clarify how EMC mode may change the charge distribution of analytes.

Deprotonated humulone was selected at CV = -2.7 V and deprotonated isohumulone was selected at CV = -12.0 V. The action spectrum for deprotonated humulone was created by monitoring the depletion of the parent mass m/z=361.2, and the formation of daughter fragments m/z=347.4 and 292.2, whereas the action spectrum of deprotonated isohumulone was created by monitoring the main fragments m/z=264.5, 265.4, and 195.7, among other minor fragments. The photofragmentation mass spectrum of deprotonated humulone and deprotonated isohumulone at 276 nm are shown in Figure 4.5a and Figure 4.5b, respectively. In the case of deprotonated humulone, the m/z=347.4 fragment can be attributed

to the loss of CH_2 , forming the structure for deprotonated cohumulone, whereas the m/z=292.2 fragment results from loss of C_5H_9 . For deprotonated isohumulone, the major photodissociation fragments are m/z=264.5 and 265.5 and that can be attributed to the loss of the acyloin moiety leading to the formation of humulinic acid and dehydrohumulinic acid, respectively, followed by the subsequent loss of C_5H_9 to produce m/z=195.7.

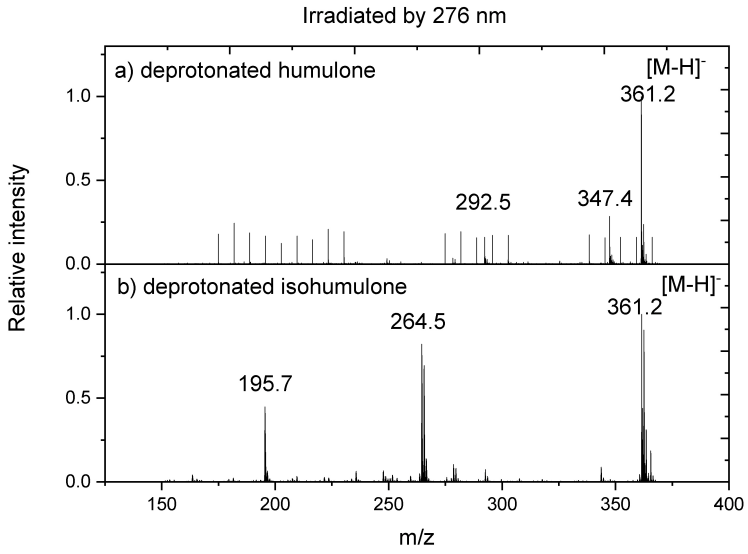

Figure 4.5: The mass spectrum collected for a) deprotonated humulone and b)deprotonated isohumulone when irradiated by 276 nm light.

The degradation of isohumulone via photolysis to form dehydrohumulinic acid is the first step in creating the light-struck flavour in beer. The photofragmentation occurs via a Norrish type I mechanism causing the cleavage of the acyloin moiety. [71, 72]. In a Norrish Type 1 photoreaction, a carbonyl is first excited into a singlet state then undergoes a spin-forbidden transition into a low-lying triplet state via an intersystem crossing. Once in the excited triplet state, an energy transfer occurs, causing the cleavage of a C-C bond located next to the carbonyl α-carbon. [73] Once the cleavage takes place, products may

undergo rearrangement on the GS PES to form stable products.[73] Isohumulone possesses an enolized -tricarbonyl chromophore. [74]

It is important to note that during the photodissociation experiment of deprotonated isohumulone, parent and ion fragment masses appear to shift by 1 m/z unit during the low energy OPO regime (292-360 nm) and in high energy OPO regime (208-234 nm), while the intermediate energy regime (234-292 nm) appears to be unaffected. Due to the frequency dependence of the mass shift, the discrepancy has been attributed to slight movement in the UV beam that causes a change in the photodepletion conditions. The mass spectra depicting these mass shifts can be found in Appendix B.

The total action spectrum for deprotonated humulone and isohumulone is shown in Figure 4.6. The onset of the first vibronic progression in the action spectrum for deprotonated isohumulone is blueshifted in comparison to the action spectrum obtained for deprotonated humulone, in agreement with reported solution phase UV-Vis absorption spectra for the two species. [75, 76, 77] While the two vibronic bands occurring between 4.0 - 4.75 eV and 4.75 eV - 5.75 eV are similar in both species, deprotonated humulone demonstrates additional absorption activity in the low energy region of the spectrum, with a local maximum occurring at 3.43 eV. Therefore, spectral dissimilarities between deprotonated humulone and isohumulone indicates that the electronic spectrum can be used as a fingerprint to identify either species by probing absorption activity at 3.43 eV. Notably, both deprotonated humulone and isohumulone demonstrate absorption at the wavelength used to calculate IBU, 275 nm (4.51 eV), providing further evidence that IBU measurements can be artificially increased by α-acid absorption interference. Globally, both spectra depict broad vibronic bands that lack vibrational fine structure. This indicates that the dominate

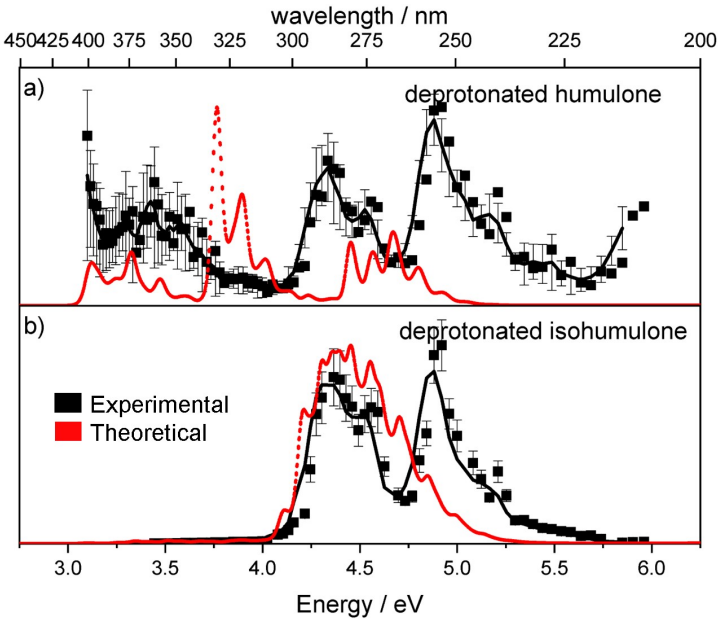

Figure 4.6: The action spectrum obtained for a) deprotonated humulone and b)deprotonated isohumulone. Black points indicate raw data, black curves present the 3-point average of the raw data. Error bars represent +/- 0.5 σ at each wavelength. The red curves represent the theoretical vibronic spectrum calculated for each species.

photofragmentation mechanisms in deprotonated humulone and deprotonated isohumulone occur on a vibrationally hot ground state surface. Further investigations into elucidating the fragmentation mechanisms is needed.

The band maxima for deprotonated humulone occur at 3.43 eV (362 nm), 4.34 eV (286 nm), and 4.88 eV (254 nm). The maxima occurring at 3.43 eV and 4.88 eV are relatively consistent with the first and second absorption maximum reported in UV-Vis solution phase absorption, measured at approximately 3.59 eV (345 nm) and 5.28 eV (235 nm), respectively.[75, 76, 78] Using the two absorption maxima as a reference, the gas phase spectrum is approximately 20 nm red-shifted in comparison to solution phase results. Additionally, the action spectrum of deprotonated humulone shows a third absorption maximum, intermediate in energy between the two expected maxima, that is not observed in solution phase.

In contrast, the deprotonated isohumulone spectrum shows a band maximum at 4.37 eV (284 nm), and a secondary maximum occurring at 4.88 eV (254 nm). The experimentally determined absorption maxima in deprotonated isohumulone are in good agreement with the expected absorption wavelengths of its chromophore. The enolized β-tricarbonyl chromophore is known to have a strong $\pi - \pi^*$ type absorbance at a wavelength of 255 nm and possess an absorbance shoulder at 270-280 nm. [74] Furthermore, the reported deprotonated isohumulone action spectrum matches the solution phase UV-Vis absorption spectrum. [77]

Computational results

Table 4.1 shows the first nine vertical excitation energies for deprotonated humulone, *cis*-isohumulone, and *trans*-isohumulone, along with their dominant transition type. Deprotonated humulone is predicted to exhibit lower energy absorption when compared to deprotonated isohumulone, verifying the observed energy shift in the experimental action spectrum. All three species possess predominately $\pi - \pi*$ type transitions, as expected with the presence of highly conjugated chromophores. Interestingly, the HOMO-LUMO transition for all three species demonstrates a $\pi - n^*$ type of transition, as shown in Figure 4.7.

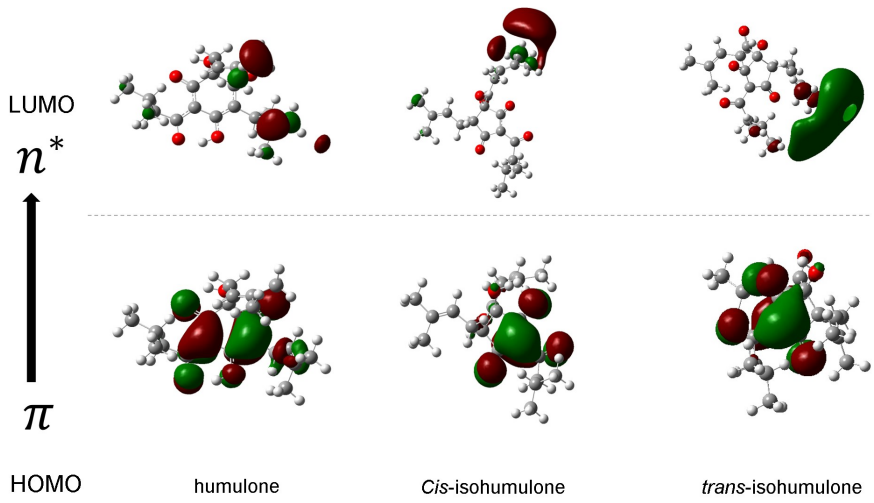

Figure 4.7: The HOMO-LUMO transition orbitals for deprotonated humulone, *cis*-isohumulone, and *trans*-isohumulone. Determined at the CAM-B3LYP/6-311++G(d,p) level of theory.

Table 4.1: The first nine vertical excitations (eV) for deprotonated humulone, *cis*-isohumulone, and *trans*-isohumulone, calculated using CAM-B3LYP-6311++G(d,p) on Gaussian 16. Transition type was determined by analyzing the major orbital contributions for each transition. Orbitals were considered major if their character was $\geqslant 0.2$. Oscillator strength for each vertical transition is reported in brackets.

Excited State	humulone	*cis*-isohumulone	*trans*-isohumulone
S_1	3.7987 (0.087)	4.0287 (0.006)	4.0299 (0.005)
	$\pi - \pi^*$	$\pi - \pi^*$	$\pi - \pi^*$
S_2	4.0907 (0.003)	4.2541 (0.012)	4.2434 (0.004)
	$\pi - \pi^*$	$\pi - \pi^*$	$\pi - \pi^*$
S_3	4.3319 (0.272)	4.5821 (0.003)	4.5409 (0.002)
	$\pi - \pi^*$	$\pi - \pi^*$	$\pi - \pi^*$
S_4	4.3809 (0.092)	4.6959 (0.029)	4.6273 (0.006)
	$\pi - \pi^*$	$\pi - \pi^*$	$\pi - \pi^*$
S_5	4.5534 (0.001)	4.7385(0.156)	4.8431 (0.128)
	$\pi - \sigma^*$	$\pi - \pi^*$	$\pi - \pi^*$
S_6	4.6579 (0.005)	5.1598 (0.010)	5.0634 (0.041)
	$\pi - \pi^*$	$\pi - \sigma^*$	$\pi - \sigma^*$
S_7	4.7921 (0.004)	5.2891 (0.187)	5.2043 (0.047)
	$\pi - \sigma^*$	$\pi - \pi^*$	$\pi - \sigma^*$
S_8	4.8878 (0.002)	5.3111(0.005)	5.2990 (0.023)
	$\pi - \sigma^*$	$\pi - \sigma^*$	$\pi - \sigma^*$
S_9	5.0297 (0.002)	5.3472 (0.002)	5.3526 (0.002)
	$\pi - \pi^*$	$\pi - \sigma^*$	$\pi - \sigma^*$

To provide comparison to our experimental results, the theoretical vibronic spectra containing the first nine excited states for deprotonated humulone, *cis*-isohumulone, and *trans*-isohumulone was determined. The theoretical spectrum of each species was redshifted by 50 nm and the results are presented in Figure 4.6. In the case of deprotonated humulone, the theoretical spectrum captures the initiation of the first vibronic progression with accuracy, but fails at locating absorption maxima. The theoretical results predict an individual small vibronic feature in the high energy region of the spectrum, whereas the experimental results demonstrate two large features within this energy regime. In the case of deprotonated isohumulone, the theoretical model accurately predicts the position of the first vibronic progression, however it fails to account for the second feature. This indicates that the amount of excited states considered in the FC spectrum construction were insufficient and must be expanded to include higher energy excited states. In both cases, the reduction of basis set size and the lack of consideration for non-adiabatic effects can be held responsible for some of the inconsistencies between experimental and theoretical models. As shown in Table 4.1, all three species demonstrate many degenerate and isoenergetic singlet excited states, resulting in the presence of non-adiabatic interactions like conical intersections being present. The high amount of vibrational degrees of freedom present in both deprotonated humulone and isohumulone further amplifies the amount of non-adiabatic interactions. Future computational work will be focused on calculating a vibronic model with full consideration of non-adiabatic effects for vibronic spectra generation.

4.3.3 Conclusions

In this study, DMS-MS parameters were optimized to specifically allow for the selection of deprotonated humulone and isohumulone. By performing DMS measurements and record-

ing the optimal CV needed to transmit the parent mass m/z=361.2, IPA modifier was chosen to enable maximum CV separation between transmission ion maxima of deprotonated humulone versus deprotonated isohumulone. When exposed to an IPA seeded environment at an SV of 3500 V, it was recorded that deprotonated humulone eluted at a CV = -2.7 V while deprotonated isohumulone eluted at a CV = -12 V. The large separation between elution CV for both species indicates that these conditions can be used to separate a mixture comprised of both isobars. Once selected by DMS-MS, deprotonated isohumulone and humulone were subjected to spectroscopic interrogation and their action spectrum were recorded. A significant blueshift was observed when comparing the vibronic spectrum of isohumulone to humulone, signifying that DMS-MS coupled with UVPD experiments is a viable methodology for quantifying the overall presence of bittering molecules within a beer sample. Experiments should be repeated again on different days to test for reproducibility.

Chapter 5

UVPD spectroscopy of differential mobility-selected, adenine prototropic isomers

In this chapter, a study on applying DMS-MS coupled with UVPD to protonated adenine tautomers is presented in order to directly prove that the two DMS resolved species observed by Anwar et al. corresponds to two tautomeric forms. The action spectrum for both tautomeric species is recorded and compared to quantum chemical calculations to provide insights into the identity of the tautomeric species, the electronic and geometric structure, and their behaviour under ionizing radiation. Due to the large amount of degenerate and iso-energetic excited states within protonated adenine, investigation of the non-adiabatic processes governing excited state behaviour is conducted using a linear vibronic coupling (LVC) Hamiltonian and the multiconfigurational, time-dependent Hartree algorithm. These calculations consider complicated excited state phenomena like conical

intersections. Generation of theoretical vibronic spectra using the LVC model allows for direct comparison with experimental action spectra for correct tautomer assignment.

5.1 Introduction

Adenine, one of the building blocks of DNA and RNA, plays a fundamental role in the storage, encoding, and expression of genetic information.[17] Owing to its biological relevance, many theoretical and experimental studies have been conducted to elucidate the structure and properties of adenine, such as its different tautomeric forms[79] and its interaction with UV ionizing radiation.[80, 81] Although adenine is usually a neutral molecule under physiological conditions, studies have shown the presence of protonated adenine $[A+H]^+$ in biological systems and revealed its biological functions. For instance, adenine protonated

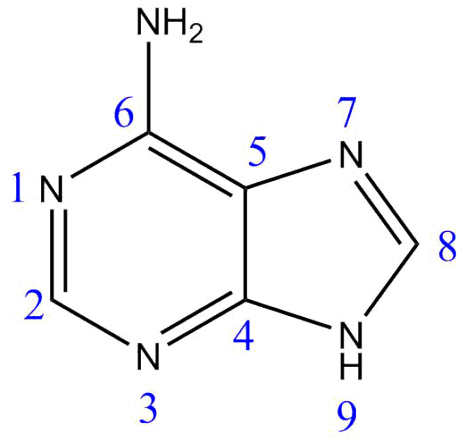

Figure 5.1: Diagram of neutral adenine with conventional numbering.

at the N1 site has been demonstrated to stabilize adenine-cytosine mismatched base pairs in RNA [18], and protonation at the N3 site may have a role in ribosome phosphodiester

cleavage.[19] Different tautomeric forms of $[A+H]^+$ have different physicochemical activities and therefore different implications in bioprocesses that may lead to mutations causing genetic disease or cancer. To understand the possible roles of the different tautomers, a thorough investigation of each isolated individual tautomer of $[A+H]^+$ and their properties needs to be performed. According to quantum chemical calculations done by Anwar and coworkers[17], four energetically low-lying tautomers of $[A+H]^+$ exist in the gas phase, each requiring their own individual and isolated experiments to elucidate their electronic structure and unique properties. The four lowest-lying tautomers, their standard nomenclature, and their relative energies are shown in Figure 5.2. Various spectroscopic techniques have been employed to study tautomers of $[A+H]^+$ and related structures, such as infrared multiphoton dissociation (IRMPD) spectroscopy[82, 83], femtosecond pump-probe spectroscopy[84], UV–UV hole-burning spectroscopy[85], and ultraviolet photodissociation action spectroscopy.[86, 87, 88] However, most spectroscopic experiments have been focused on the global minimum $[A+H]^+$ tautomer and little has been done to investigate the structures of other tautomeric species.

When coupled with mass spectrometric techniques, ultraviolet photodissociation (UVPD) action spectroscopy is a useful tool for elucidating the electronic structure of gas-phase biomolecules.[14, 15] UVPD studies have been shown to be sufficiently sensitive to distinguish between the protonation tautomers of a given species[89, 90] and have been a popular choice for studying the electronic structure of protonated, neutral, and cationic adenine. [80, 86, 87, 91, 88] Several groups have independently measured UVPD action spectra for the various tautomers of $[A+H]^+$. Notably, in a study performed by Marian et al., an investigation into the electronic structure of protonated adenine in comparison to its neutral form was conducted using a combined experimental and theoretical

approach.[87] The UV photofragmentation action spectrum reported for the range 4.2-4.9 eV demonstrated a wide onset at 4.3 eV and spectral features indicative of a strong $S_0 - S_1$ geometry shift. Based on quantum chemical calculations, the authors concluded that the spectrum resulted mainly from the global minimum tautomer,11H-9H-A^+. The wide onset was speculated to arise from a low-lying conical intersection between the S_1 excited state and the electronic ground state S_0, allowing for an ultrafast relaxation pathway and dissociation from a vibrationally hot ground state. [87] Likewise, in 2014, Berdakin et al. conducted a photofragmentation study on cold protonated adenine.[91] Their results indicated the presence of two systems that are close in energy in their experimental action spectrum. Using an argument based on Boltzmann thermal populations, the two systems were assigned to the two lowest energy tautomers respectively. [91] It is worth noting that neither study had the experimental capacity to completely eliminate the presence of other tautomers. Cheong and coworkers[88] studied the UV photofragmentation of selectively prepared $[A + H]^+$ tautomers, one prepared by dissociation of a neutral adenine dimer system, and one prepared by using a conventional electrospray ionization (ESI) source. By comparing the recorded fragmentation pattern to literature, Cheong et al. concluded that the ESI source favoured the global minimum tautomer, 1H-9H-A^+. Likewise, using quantum chemical calculations and an observed redshift in action spectrum when compared to Marian et al.'s action spectrum for the 1H-9H-A^+ tautomer, the species derived from dissociation of the dimer system was assigned to their second lowest lying tautomer, which corresponds to the 3H-9H-A^+ tautomer. It is important to note that in their study, the universal second lowest-lying tautomer, corresponding to 3H-7H-A^+, was not considered in their theoretical framework. Although the work undertaken by Cheong et al. allowed for the investigation of the electronic structure of the 3H-7H-A^+ tautomer, it remains difficult to draw comparisons between the various spectra obtained for $[A + H]^+$, owing to the fact

that the spectra collected by Cheong et al. and Marian et al. were performed under different experimental conditions and at different locations. Furthermore, it was not possible to rule out the presence of other tautomers in their ESI ensemble.[88]

Differential mobility spectrometry (DMS) lends itself naturally to being utilized to separate different tautomers of $[A + H]^+$. In a paper by Anwar et al., two tautomers of $[A + H]^+$ were separated using DMS and their physicochemical behaviour was studied using MS methods including collision-induced dissociation and hydrogen-deuterium exchange (HDX).[17] Although indirect in nature, the results of the MS studies affirmed the hypothesis that the two DMS-resolved species were indeed associated with two different tautomeric forms of $[A + H]^+$. However, assignment of geometric structure could only be made based on a Boltzmann distribution of calculated gas-phase structures.[17] In this chapter, it is proven that that the two species resolved by Anwar et al. are two different tautomeric forms, by directly probing their electronic structures using UVPD action spectroscopy. Complimentary theoretical work is used to support experimental findings and provide structural assignments to the resolved species.

5.2 Methods

5.2.1 Experimental methods

A SelexIon differential mobility spectrometer was used in tandem with a QTRAP 5500 mass spectrometer (SCIEX; Concord, ON). An ESI voltage of +4500 V was used and the source temperature was set to 32^oC. A nebulizing gas pressure of 30 psi and an auxiliary gas pressure of 0 psi were used. The DMS cell was set to a temperature of 150^oC. Nitrogen

was used as both the curtain gas (20 psi) and the gas for collisionally activated dissociation (9mTorr).

Adenine was purchased from Sigma-Alderich and diluted to a concentration of 10 ng/mL in 50:50 mixture of ultrapure water and methanol with 0.1% formic acid. The adenine solution was pumped into the ESI source at a rate of 7μL/min. Enhanced product ion (EPI) mode was used to study the parent ion $m/z = 136$ in positive mode. The DMS separation voltage (SV) was scanned from 0 V to 4000 V in increments of 500 V from 0-3000 V, and in increments of 200 V from 3000-4000 V, whereas the compensation voltage (CV) was scanned from -10 V to + 10 V in 0.1 V increments to produce an ion transmission curve (ionogram) at each SV step. The ionogram was fit to a Gaussian curve and the maxima were recorded at each corresponding SV point to create a dispersion plot. A SV of 3500 V was selected for the photodissociation experiments to give maximum spatial separation between ion transmission maxima.

To facilitate photodissociation experiments, the DMS-MS apparatus was retrofitted with a window to allow for light from an Nd:YAG-pumped optical parameteric oscillator (OPO) as described previously.[26] Ion transmission maxima from the DMS-MS experiments were selected as SV/CV pairs and were held in an ion trap for 1 and 30 ms, respectively, to ensure ideal ion intensity as they were irradiated by the OPO. The OPO was scanned in increments of 1 nm from 208-350 nm for 20 cycles. Parent and fragment ion intensities were monitored and recorded at each wavelength step and their relative intensities were used to generate an action spectrum. Experiments were repeated three times on different days to ensure reproducibility and can be found in Appendix C.

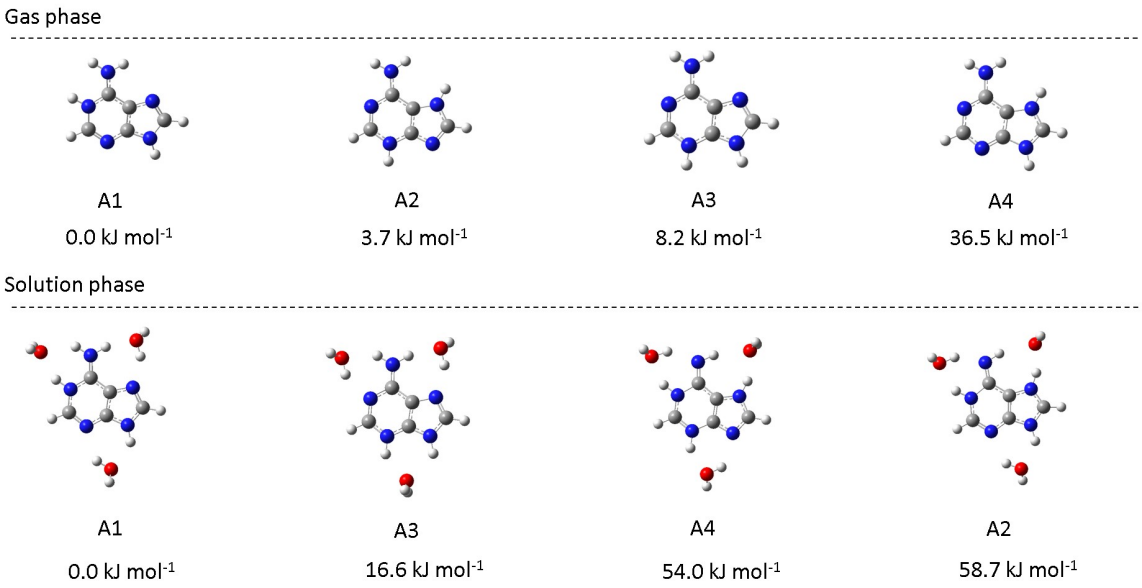

Figure 5.2: Relative energy ordering of the four lowest-lying tautomers of $[A+H]^+$ in both the gas and solution phase. Structures were optimized using B3LYP/6-311++G(d,p) and the electronic energy was calculated using CCSD(T)/6-311++G(d,p).

5.2.2 Computational methods

All geometric structure and electronic energy calculations were performed using Gaussian 16. [92] Four adenine tautomers were found by changing the site of protonation, as shown in Figure 5.2. The initial optimized structures of $[A+H]^+$ were taken from the work done by Anwar et al. at the B3LYP 6-311++G(d,p) level of theory.[17]. Normal mode analyses were performed using the same level of theory to ensure these structures were located on a minimum on the potential energy surface and the electronic energies of the DFT optimized structures were improved using CCSD(T)/6-311++G(d,p). The first fifteen vertical excitation energies were calculated for all four tautomeric species using TD-DFT on Gaussian 16, at the same level of theory described above. To further refine the excited state energies,

the vertical excitation energies were calculated again using the STEOM-DLPNO-CCSD/6-311++G(d,p) level of theory on ORCA 4.2.1[93]. STEOM-DLPNO-CCSD has been shown to provide more accurate vertical excitation energies when compared to experiment for 50 Boron-dipyrromethene compounds than their TD-DFT analogues with similar computational time.[94]

Theoretical vibronic spectra, including vibronic coupling effects were generated to include the first fifteen excited states using a linear vibronic coupling Hamiltonian in a diabatic basis set. The theory behind this method can be found elsewhere and the fundamentals are described in Chapter 3. [95, 96] An adiabatic reference basis set was created using vibrational and excited state single point energy calculations at the B3LYP/6-311++G(d,p) level of theory on Gaussian 16 and the TD-DFT transition densities are transformed into a diabatic basis set using the maximum overlap criterion[97]. The diabatization scheme yields an operator file that includes all the Hamiltonian parameters needed to model the system of interest. Electric transition and magnetic dipole moments were included for all excited states along each Cartesian coordinate individually. The operator file was subjected to a wave-packet propagator within the Multi-configurational, time dependent Hartree algorithm (MCTDH) framework[98, 99], as implemented in the QUANTICS software package[100], generating an autocorrelation function. Due to the size of the species being investigated, only one single particle function was used to describe each excited state along each normal mode. The autocorrelation function was Fourier transformed to generate a spectrum along each Cartesian coordinate. The results along each coordinate were summed to create the rotationally averaged vibronic spectrum. Details on the input parameters selected for calculations are provided in Appendix C. All calculations were repeated using the CAM-B3LYP functional for a test system, however, results for B3LYP

were found to be more consistent with experimental findings.

5.3 Results

5.3.1 DMS-MS and collision induced dissociation of $[A+H]^+$

Figure 5.3 shows the dispersion plot for four different ion signals for protonated adenine following differential mobility separation in N2(g)by Anwar et al. [17] The major features highlighted by the red and black lines occur at an ion transmission intensity of 10^8 whereas the minor features in blue and green occur at an intensity of 10^6. Using declustering potential (DP) studies, it was determined that the red and black curves result from tautomer derived species, whereas the green and blue signals are attributed to weakly bound adenine-solvent clusters that fragment post-DMS to yield the bare ion.[17] Therefore, in the presented work, the possibility of the multiple peaks being attributed to weakly-bound clusters was ruled out by setting the declustering potential to 0 V. Figure 4b shows the resulting ionogram recorded when selecting for protonated adenine (m/z 136) at an SV of $3500V$. Two ion transmission maxima at $CV = -6.1V$ and $CV = -3.1V$ are observed, in agreement with the results obtained by Anwar et al.[17]. An asymmetric feature located at $CV = -1.2V$ on the Gaussian curve centered at $CV = -3.1V$ was also selected for investigation. To reiterate, due to the dependency the transmission CV has on the unique ion mobility of the analyte, the presence of two ion transmission maxima indicates that there exist at least two isomeric forms of $[A+H]^+$ under current experimental conditions. The CV values at which maximum ion transmission was obtained for each tautomer of protonated adenine were used for ion selection prior to electronic excitation in the UVPD experiments.

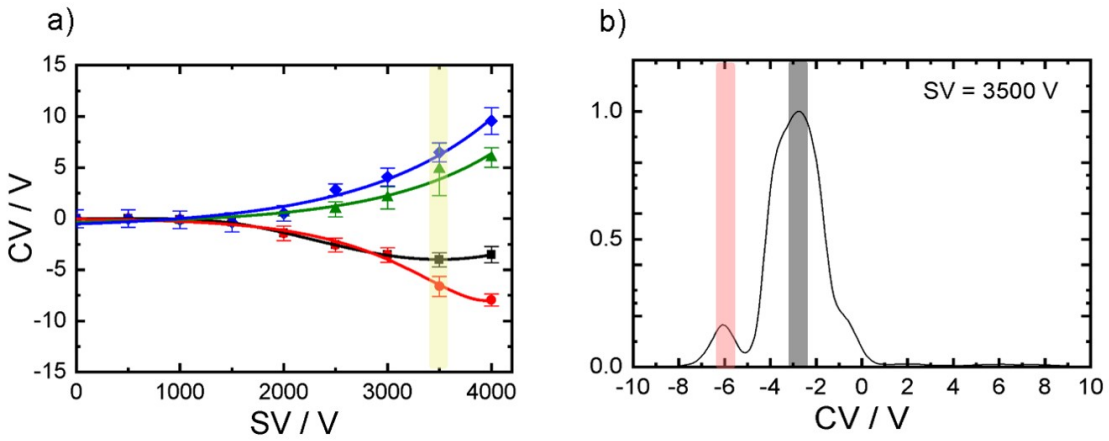

Figure 5.3: a) The dispersion plot obtained by performing DMS-MS experiments on m/z= 136 in a pure $N_{2(g)}$ environment. Modified from the data presented by Anwar et al.[17] b) The obtained ionogram at SV = 3500V. The red and black shaded regions indicate the ion transmission maximum recorded resulting from tautomeric species at CV = -6.1 V and CV = -3.1 V, respectively.

Upon irradiation, the generation of product fragments m/z = 119, 109, and 94 were monitored along with the depletion of the parent ion (m/z = 136) to generate an action spectrum. The fragments with m/z= 119 and 109 are associated with loss of NH_2 and loss of HCN, respectively, and are observed in high abundance in CID studies and are consistent with the fragmentation pattern reported by Anwar et al.[17] As stated in the literature, these fragments are likely statistical in nature and do not have differences in dissociation mechanisms between tautomers.[88, 87]. The fragment m/z= 94 is associated with loss of NH_2CN and is typically not observed in high abundance following CID of the parent ion and has been shown by femtosecond pump-probe experiments to be a photoinduced dissociation (PID) fragment of protonated adenine. [101, 84] Nolting et al. described the m/z = 94 appearing after initial pump excitation, with the intensity of production increasing

once the species is further excited by the probe wavelength.[84] As a result of its photo-specific behaviour, this fragmentation channel should be highly sensitive to differences in electronic structure between tautomers and should therefore be a good choice for tautomer differentiation. As demonstrated in the study by Berdakin et al. where differences in the m/z = 94 channel were used to distinguish between tautomers.[91] In the work by Berdakin et al., two unique photofragmention systems were observed for $[A+H]^+$, one starting its vibronic progression at $4.40eV$ and one at $4.54eV$. Aside from exhibiting differences in band progressions, it was noted that in the low energy system, m/z= 94 and $m/z = 119$ were produced at the same intensity, whereas in the high energy system $m/z = 119$ was produced at a higher intensity than $m/z = 94$. Berdakin et al. stated that the intensity difference in the $m/z = 94$ mass channel likely arise from structural differences between tautomers. [91]

5.3.2 Action spectroscopy and calculated vibronic spectra

The photodissociation action spectra for the two ion populations transmitted at $CV = -3.1V$ and $CV = -6.1V$ ($SV = 3500V$) are shown in Figure 5.4. The asymmetric shoulder at $CV = -1.2V$ yielded the same spectrum as the main feature at $CV = -3.1V$ and was credited as resulting from the same tautomer. The spectrum for $CV = -1.2V$ can be found in Appendix C. In both Figure 5.4a and 5.4b, a broad and smooth onset is observed, along with features that lack vibrational resolution. This may be indicative of a short excited-state lifetime or many vibrational transitions being accessed. Indeed, as demonstrated in Table 5.1, the vibronic progression observed experimentally begins at a lower energy than the anticipated S_1 surface across all tautomeric species, allowing to infer that the fragmentation occurs on the electronic ground state S_0. A direct comparison with

calculated vibronic spectra is necessary to assign each spectrum correctly.

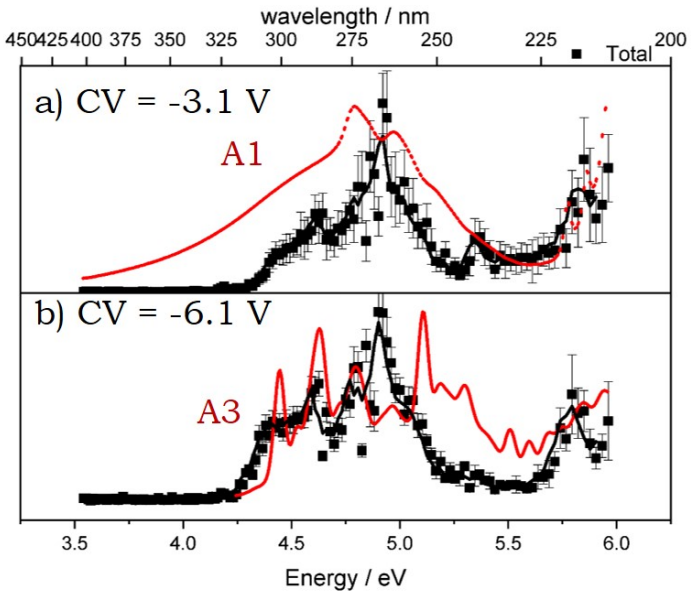

Figure 5.4: The total action spectrum collected for $[A+H]^+$ at $SV = 3500V$ at a) $CV = -3.1V$ and b) $CV = -6.1V$ in a $N_{2(g)}$ environment. Points represent the raw data, curves represent a 3-point Gaussian smooth of the data, and the error bars represent $pm0.5\sigma$ at each scanned wavelength.

The first three vertical excitations for each tautomer are tabulated in Table 5.1. It can be noted that degenerate and iso-energetic excited states are present in all four tautomers. Degenerate states are considered to be within the vibrational energy spacing (0.2-0.3 eV) whereas iso-energetic states are spaced between 0.4-0.6 eV. As described in detail in Chapter 3, when excited states are degenerate or iso-energetic, the states can interact with each other through non-adiabatic interactions like vibronic coupling of excited states. The presence of many degenerate and iso-energetic excited states in all four $[A+H]^+$ tautomers

Table 5.1: The first three vertical excitations (eV) for each $[A+H]^+$ tautomer and their major canonical orbital contributions. Orbital contributions were considered if their amplitude was greater than 0.20. Oscillator strengths are reported in brackets. Calculated using STEOM-DLPNO-CCSD/6-311++G(d,p) on ORCA 4.2.1

Excited State	A1	A2	A3	A4
S_1	4.67 (0.229)	4.74 (0.496)	4.76 (0.478)	4.62 (0.324)
	$\pi - \pi^*$	$\pi - \pi^*$	$\pi - \pi^*$	$\pi - \pi^*$
S_2	5.32 (0.004)	4.85 (0.122)	4.93 (0.008)	4.70 (0.049)
	$n - \pi^*$	$\pi - \pi^*$	$\pi - \pi^*$	$\pi - \pi^*$
S_3	5.34 (0.102)	5.13 (0.000)	5.03 (0.002)	4.87 (0.002)
	$\pi - \pi^*$	$n - \pi^*$	$n - \pi^*$	$n - \pi^*$

suggests that the excited state dynamics of these species may be regulated by non-adiabatic processes. Indeed, conical intersections have been computationally shown to be ubiquitous in excited states for both neutral and protonated adenine. [87, 102, 103, 104, 105]. In the theoretical investigations reported by Nielson et al. and Marian et al. on the structures of A3 and A1, respectively, conical intersections existing between S_0 and S_1 surfaces have been located at a distorted ring puckered geometry. [87, 105] Therefore, in order to generate accurate theoretical models, non-adiabatic effects must be considered. The theoretical vibronic spectra for the four lowest lying tautomers of $[A+H]^+$ are shown in Figure 5.5.

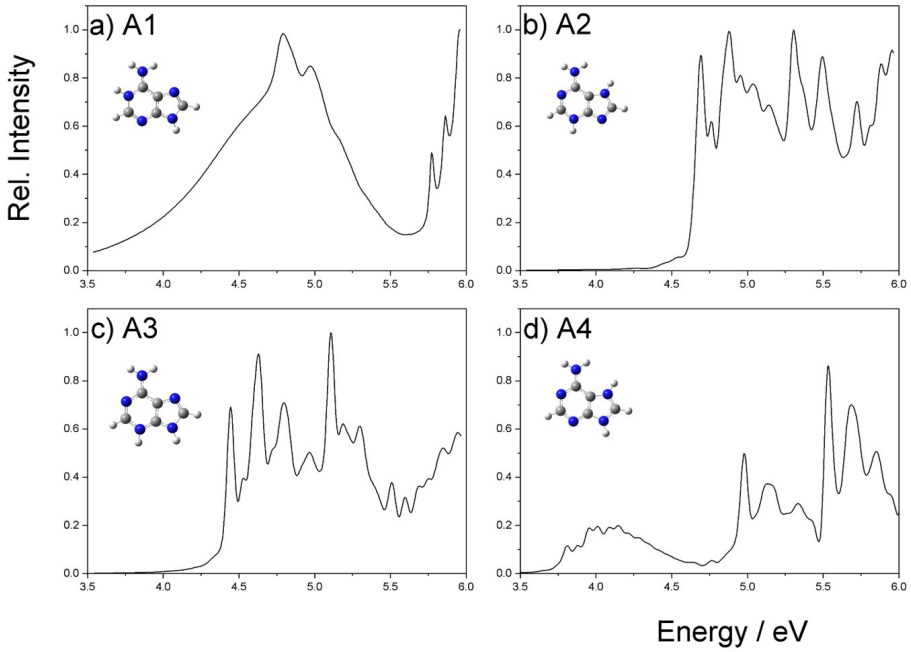

Figure 5.5: Theoretical vibronic spectra calculated for the four lowest-lying tautomers of adenine using a linear vibronic Hamiltonian model at the B3LYP/6-311++G(d,p) level of theory.

The presence of A4 can be immediately ruled out: in addition to being the highest energy tautomer, the predicted spectrum for A4 shows response within the low energy region of the spectrum (3.5-4.5 eV). This not observed in either experimental spectrum, leaving A1, A2, and A3 for consideration. First, consider the action spectrum presented in Figure 5.4a for $CV = -3.1V$. The first feature begins at approximately 4.3 eV and exhibits a wide, smooth onset leading up to a main feature at 4.9 eV, in good agreement with the reported action spectrum by Marian et al.[87] The wide feature and lack of vibrational fine struc-

ture is consistent with the predicted spectrum of A1. Furthermore, the vertical excitation energies reported in 4.1 indicate the presence of an energetically isolated S_1 surface, in accordance with only one distinct absorption maximum being present in Figure 5.4. It is important to recognize that our predicted spectrum for A1 appears to be over-broadened, potentially due to theoretical limitations of the MCTDH calculation. More investigation into the cause of the over-broadening is needed. Assuming thermal equilibrium is reached, one expects the global minimum tautomer, A1, to be the most abundant species. Since the ionogram recorded at $SV = 3500V$ shows a larger ion population at $CV = -3.1V$ in comparison to $CV = -6.1V$, both the action spectrum and ion population support A1 assignment to the $CV = -3.1V$ resolved species.

Now, consider the spectrum plotted in Figure 5.4b for CV = -6.1 V. In comparison to the A1 spectrum, the lower energy region (4.25-4.6 eV) of the spectrum, is more intense and it is red shifted by approximately 0.2 eV in comparison to Figure 5a, consistent with the results reported by Cheong et al.[88] The spectrum shows the presence of two distinct features occurring at 4.6 eV and 4.9 eV. Both tautomers A2 and A3 have energetically close S1 and S2 states that could account for the features in this vibronic progression. A noticeable band gap with the range of 5.2-5.6 eV distinguishes A2 and A3. This is indicative of the fact that the excited states being accessed at this energy level do not lead to a dissociative channel. The predicted spectrum of A3 possesses this band gap, whereas the predicted spectrum of A2 does not, allowing us to conclude that the spectrum presented in Figure 5b corresponds to A3. Although the comparison of the theoretical to the experimental spectrum provides a strong argument for assigning the species to A3, it is worth noting that a mixture of A2 and A3 cannot be ruled out entirely.

To further investigate the differences in electronic structure between the proposed tautomers of protonated adenine, the individual action spectra for each of the three primary fragments (m/z = 119, 109 and 94) were analyzed and are found in Appendix C. As expected, the action spectra for the fragmentation channels m/z = 119 and 109 were identical to each other in both tautomeric species A1 and A3, validating the hypothesis that these fragments are statistical in nature. Interestingly, in the A1 spectrum, the m/z= 94 channel shows the same action spectrum as the other two primary fragments. Therefore, one can conclude that these fragments occur statistically from a vibrationally hot ground state, consistent with similar works in literature.[87, 88] In contrast, in the case of A3, the action spectrum for m/z = 94 shows a somewhat different intensity profile to that of the other two fragments. This indicates that a different dissociation channel is being accessed to produce m/z = 94 in A3 in comparison to A1.

Comparing the individual action spectra for the generation of the photoinduced fragment $m/z = 94$, as shown in Figure 5.6, reveals that the spectral dissimilarities found in the total action spectrum reported in Figure 5 are replicated in higher intensity when considering exclusively the m/z = 94 channel. In the A3 m/z= 94 action spectrum, a distinct band gap is present between maxima located at 4.6 eV and 4.9 eV. By analysing the S_1 (4.76 eV) and S_2 (4.93 eV) excited state energies for A3 in Table 1, it can be speculated that these two maxima can be attributed to the $S_0 - S_1$ and $S_0 - S_2$ transitions, respectively.

To gain further insights into the fragmentation mechanism involved in the formation of the m/z=94 fragment, relaxed redundant coordinate scans were performed on Gaussian 16. Redundant coordinate scans were performed using B3LYP/6-311++G(d,p) for A3 and at the PM6 level of theory for A1, due to computational limitations. The calculations were

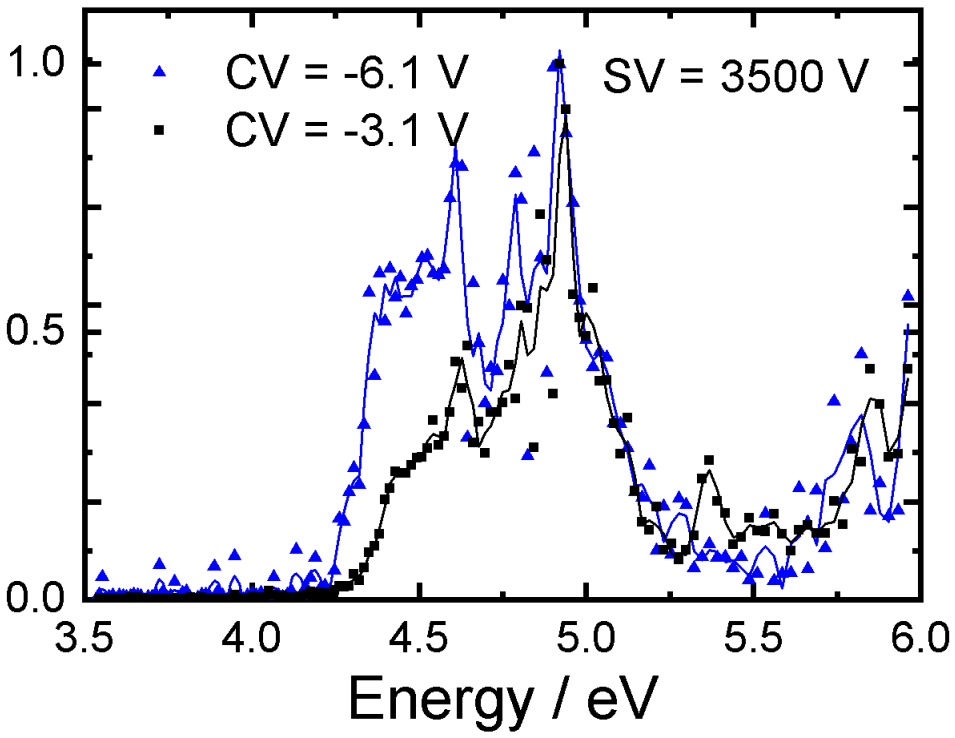

Figure 5.6: The action spectrum obtained by monitoring the formation of m/z= 94 from fragmentation of the A1 and A3 parent species. Points represent the raw data and curve represent a 3-point Gaussian smooth of the data.

performed in two steps, first scanning along the cleaved N-C bond, followed by scanning along the C-C bond to fragment the molecule fully to form m/z=94 and $[A+H-94]^+$. It is important to note that while redundant coordinate scans provide a qualitative picture of the dissociation pathway, the energetics and thermodynamics require a proper optimization and normal mode analysis treatment to be accurate. The proposed mechanisms are shown in Figure 5.7 Resulting in the difference in protonation sites on the six-membered ring, it was discovered that A1 and A3 yield different product ions and neutral fragment loses. In the case of A1, the parent ion loses HNCNH, whereas the photofragmentation of

A3 causes the loss of NH_2CN. The variation in proposed product ions upon loss of m/z=94 is consistent with the observed differences between action spectrum for the channel in A1 compared to A3. In the case of A3, one expects the dissociation of m/z= 94 to proceed through a different mechanism, in contrast to the other product ions, due to the action spectrum for this channel different than for m/z= 119 and 109. Furthermore, the results of the A1 fragmentation study are consistent with the proposed mechanism obtained from a MD simulation performed by Giacomozzi et al. [106] While the results of the redundant coordinate scans provide a foundation for elucidating the fragmentation mechanism for A1 and A3, it is important to note that these calculations must be repeated at a higher level of theory to be accurate. Additionally, all calculations were conducted on the electronic ground state, not considering the necessary absorption event that drives the photodissociation process. Due to the excited state nature of photodissociation, it is extremely likely that non-adiabatic dynamics are governing the photofragmentation pathway. For example, one potential mechanism may be initiated by an excitation into a low-lying singlet state, loosening the first cleaving bond. The system then may undergo an intersystem crossing into a nearby triplet state, allowing for the loosening of the second cleaving bond. Afterwards, the system may transition into the ground state singlet state via a conical intersection, allowing for fragmentation. Potential mechanisms on the excited state surfaces need to be further investigated computationally to gain an in-depth understanding of possible fragmentation pathways.

Based on the results of the computational fragmentation mechanism studies, dissociation thresholds for each product ion were calculated. The structures for each product fragments resulting from the tautomers A1 and A3 in the ground state were optimized on Gaussian16 at the B3LYP/6-311++G(d,p) level of theory and normal mode analyses were performed

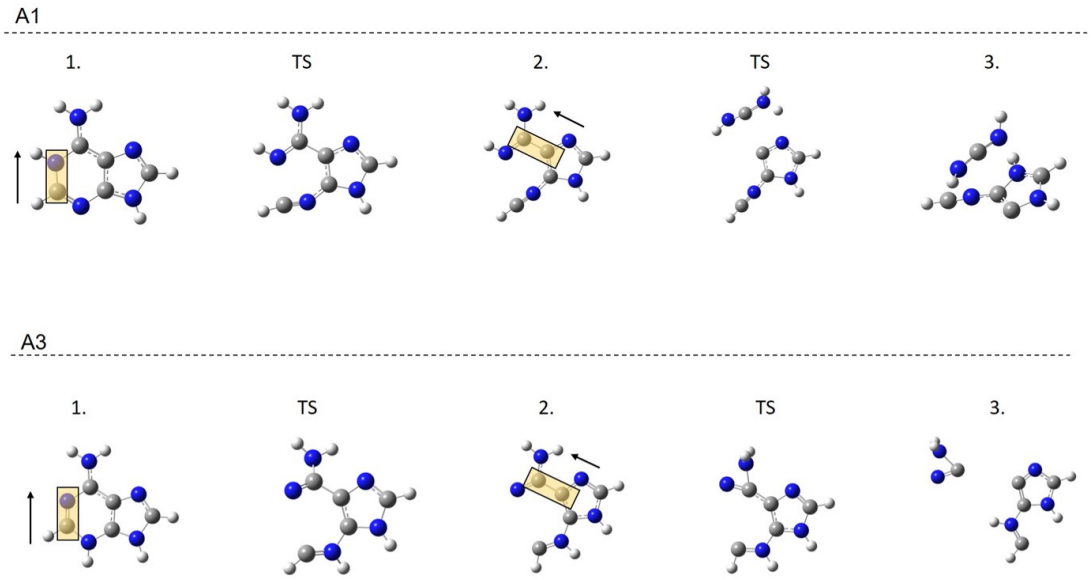

Figure 5.7: The qualitative depiction of the proposed fragmentation mechanism elucidated by relaxed redundant coordinate scans in Gaussian16.

to obtain the thermodynamic properties of each molecule. The Gibbs energy of formation equation was used to calculate the thermodynamic threshold of dissociation for each product fragment and are tabulated in Table 5.2. Exact structures used in the calculation of thermodynamic thresholds can be found in Appendix C. The thermodynamic thresholds were found to be below the single photon energy across all product fragments and tautomers investigated, even for the lowest energy photons used (3.54 eV). This implies that that the dissociation is governed by a high energy transition or intermediate state, and therefore, more computational work will be needed in order to determine the true threshold of dissociation. Interestingly, the thermodynamic thresholds for all product fragments were below the vertical excitation energies for all species. It can be inferred that all dissociation events occur on a vibrationally hot ground state. In the case of A1, the broadness

Table 5.2: The thermodynamic thresholds in (eV) required to fragment parent ion into resulting product ions.

Fragment (m/z)	A1	A3
119	3.41	3.35
109	3.48	3.41
94	3.19	5.04

of both the predicted and experimental spectrum reflects a coupling with a dissociative channel. Indeed, theoretical studies, such as the work done by Marian et al. and Nielson et al., predict a low-lying conical intersection between the first excited singlet and the ground state for both A1 and A3.[87, 105] This would allow for an ultrafast internal conversion to a highly excited vibrational state within the electronic ground state, allowing for statistical fragmentation of all three product ions. This is further supported by considering that all three individual fragment channels showed the same action spectrum in A1, meaning they must be produced in the same manner.

5.3.3 Justifying tautomer assignments using condensed-phase calculations

According to conventional Boltzmann statistics determined at the DMS cell temperature of 150^oC, the relative populations of structures A1, A2, and A3 should be 0.69, 0.24, and 0.07, respectively. From these results, the tautomer assignments made by direct comparison to the theoretical vibronic spectra are not consistent with the predicted gas-phase tautomer equilibrium. However, Boltzmann statistics do not necessarily apply within the DMS cell due to non-equilibrium effects including localized heating and kinetic trapping of energetic

tautomers. In order to explore the latter effect, the aqueous-phase tautomer equilibrium was investigated computationally. Cluster systems consisting of $[A+H]^+$ with three H_2O molecules at the H-bonding sites were created to mimic the first solvation shell and the polarizable continuum model (PCM) was employed to account for the solvent effects of water. Structures were optimized at the B3LYP/6-311++(d,p) level of theory with the inclusion of Grimme's dispersion correction (GD3) and normal mode analysis was performed to ensure the resulting structures correlated to a minimum. Electronic energies were calculated using CCSD(T)/6-311++G(d,p), as shown in Figure 5.2. Interestingly, the relative tautomer energy ordering changed in the solution phase compared to gas-phase. Using the original nomenclature for consistency, the tautomer energy ordering becomes: A1 (0 kJ/mol), A3 (16.6 kJ/mol), A4 (54.0 kJ/mol) , A2 (58.7 kJ/mol). This is consistent with the fact that the two tautomers identified in our action spectroscopy experiments and by Cheong et al. and Marian et al.[87, 88] were tautomers A1 and A3. A possible explanation for capturing the solution phase equilibrium rather than the gas-phase in the DMS cell may be that the A3 tautomer is kinetically trapped upon vaporization in ESI. The large energy difference between A3 and A2 allows us to confidently rule out the presence of A2 in the DMS resolved species.

5.4 Conclusions

When coupled with DMS-MS studies, UVPD is a useful tool for distinguishing and characterizing tautomers in the gas-phase by observing their electronic structure. In this study, two tautomers of protonated adenine were successfully separated and probed their electronic structure. Two ion transmission maxima were recorded for SV = 3500 V at CV = -3.1 V and CV = -6.1 V. Theoretical vibronic spectra for all four tautomers were produced

using a linear vibronic coupling Hamiltonian. By comparing the resulting experimental action spectra to calculated vibronic spectra, assignment of tautomers A1 and A3 were made. Broad spectral features shared between both experimental spectra may indicate that a short excited-state lifetime is present. Computational calculations suggestion that a conical intersection results in the fragmentation primarily occurring from a vibrationally hot ground state. Differences in the action spectrum for the m/z = 94 for the A3 tautomer in comparison to other product ions and results from fragmentation mechanism calculates seems to indicate a unique dissociation channel was accessed. A difference in fragmentation pathways and product ions were suggested as the cause of the observed differences between A1 and A3. Theoretical investigations into the aqueous-phase tautomer equilibrium was performed and an energetic reordering in comparison to the gas-phase was observed that aligned with the assigned tautomeric species for the observed experimental results. Similar analyses have been extended towards protonated cytosine and protonated uracil tautomers. The preliminary experimental and theoretical spectra for these species can be found in Appendix C.

Chapter 6

Conclusions

In this thesis, the use of DMS-MS-UVPD action spectroscopy as an analytical technique to separate and identify isomers was explored. A joint experimental and computational approach was taken to elucidate the electronic structures of the geometric isomers deprotonated humulone and isohumulone, as well as the tautomeric isomers of protonated adenine. Noticeable differences in the electronic and geometric structures of the species allowed for verification of their identity.

In Chapter 4, the use of DMS-MS-UVPD to separate and distinguish between deprotonated humulone and isohumulone was investigated. The dynamic clustering behaviour of both species was determined, and the DMS-MS parameters were optimized to allow for maximum separation between deprotonated humulone and isohumulone. When exposed to an IPA seeded environment at an SV of 3500 V, it was recorded that deprotonated humulone is transmitted at CV = -2.7 V, while deprotonated isohumulone is transmitted at CV = -12 V. The 9 V separation between elution CV for deprotonated humulone and isohu-

mulone allows it to be inferred that the species would be separable in mixture comprised of both isomers. Using the optimized DMS-MS conditions, deprotonated isohumulone and humulone were selected and subjected to UV-PD experiments and their action spectrum were recorded. A significant blueshift was observed when comparing the vibronic spectrum of isohumulone to humulone, indicating that the spectral dissimilarities can be utilized to distinguish between either isomer. Computational calculations verified that the observed action spectra are accurate.

In Chapter 5, it was revealed that DMS-MS-UVPD is a useful tool for distinguishing and characterizing tautomers in the gas phase, by observing their electronic structure. In this study, two tautomers of protonated adenine were separated, and their electronic structure was revealed. Two ion transmission maxima were recorded for SV = 3500 V at CV = -3.1 V and CV = -6.1 V. Theoretical vibronic spectra for four low-lying tautomers were produced using a linear vibronic coupling Hamiltonian. By comparing the results in the experimental action spectra to calculated vibronic spectra, assignment of tautomers A1 and A3, respectively, were made. Broad spectral features shared between both experimental spectra may indicate that a short excited-state lifetime is present. The results from quantum chemical simulations suggestion that the primary mechanism for fragmentation occurs through a conical intersection to a vibrationally hot electronic ground state. Spectral dissimilarities in the action spectrum for the $m/z = 94$ in comparison to other daughter ion channels in the A3 tautomer, along with results from fragmentation mechanism calculations, draw the conclusion that a unique photofragmentation pathway was accessed. The difference in theoretical fragmentation mechanisms derived for A1 and A3 are used to rationalize the observed differences in experimental spectra. By calculating the aqueous-phase tautomer equilibrium using both implicit and explicit solvation models, it

was determined that the observed tautomer population in the DMS cell is consistent with the solution phase equilibrium, likely owing to kinetic trapping upon electrospraying.

The results of Chapter 4 and Chapter 5 provide good evidence that DMS-MS-UVPD is a useful tool for the joint separation and identification of isomers in the gas phase. It was shown that in both the case of geometric isomers and tautomers, differences in the action spectra were observed that allowed for species distinction and were identified using theoretical vibronic spectra. The results of this thesis lay a foundation for this analytical technique to be applied to a wider scope of isomers and provided a framework to calculating computational spectra with a high degree of accuracy for comparison to experiment.

References

[1] J. E. Kyle, X. Zhang, K. K. Weitz, M. E. Monroe, Y. M. Ibrahim, R. J. Moore, J. Cha, X. Sun, E. S. Lovelace, J. Wagoner, S. J. Polyak, T. O. Metz, S. K. Dey, R. D. Smith, K. E. Burnum-Johnson, and E. S. Baker, "Uncovering biologically significant lipid isomers with liquid chromatography, ion mobility spectrometry and mass spectrometry," *The Analyst*, vol. 141, no. 5, pp. 1649–1659, 2016.

[2] H. Maeda, T. Takata, N. Fujii, H. Sakaue, S. Nirasawa, S. Takahashi, H. Sasaki, and N. Fujii, "Rapid survey of four asp isomers in disease-related proteins by lc-ms combined with commercial enzymes," *Analytical Chemistry*, vol. 87, no. 1, pp. 561–568, 2015. PMID: 25479244.

[3] Ł. Marczak, P. Znajdek-Awiżeń, and W. Bylka, "The use of mass spectrometric techniques to differentiate isobaric and isomeric flavonoid conjugates from axyris amaranthoides," *Molecules*, vol. 21, p. 1229, Sept. 2016.

[4] M. Belka, W. Hewelt-Belka, J. Sławiński, and T. Baczek, "Mass spectrometry based identification of geometric isomers during metabolic stability study of a new cytotoxic sulfonamide derivatives supported by quantitative structure-retention relationships," *PLoS ONE*, vol. 9, p. e98096, June 2014.

[5] J. M. Dela Cruz, V. V. Lozovoy, and M. Dantus, "Quantitative mass spectrometric identification of isomers applying coherent laser control," *The Journal of Physical Chemistry A*, vol. 109, no. 38, pp. 8447–8450, 2005. PMID: 16834240.

[6] B. S. R. Claes, E. Takeo, E. Fukusaki, S. Shimma, and R. M. A. Heeren, "Imaging isomers on a biological surface: A review," *Mass Spectrometry*, vol. 8, pp. A0078–A0078, Dec. 2019.

[7] W. S. Hopkins, "Determining the properties of gas-phase clusters," *Molecular Physics*, vol. 113, no. 21, pp. 3151–3158, 2015.

[8] B. M. Kolakowski and Z. Mester, "Review of applications of high-field asymmetric waveform ion mobility spectrometry (faims) and differential mobility spectrometry (dms)," *The Analyst*, vol. 132, pp. 842–864, 2007.

[9] J. L. Campbell, J. Y. L. Blanc, and R. G. Kibbey, "Differential mobility spectrometry: a valuable technology for analyzing challenging biological samples," *Bioanalysis*, vol. 7, pp. 853–856, Apr. 2015.

[10] V. Blagojevic, A. Chramow, B. B. Schneider, T. R. Covey, and D. K. Bohme, "Differential mobility spectrometry of isomeric protonated dipeptides: Modifier and field effects on ion mobility and stability," *Analytical Chemistry*, vol. 83, no. 9, pp. 3470–3476, 2011. PMID: 21504141.

[11] J. L. Campbell, T. Baba, C. Liu, C. S. Lane, J. C. Y. L. Blanc, and J. W. Hager, "Analyzing glycopeptide isomers by combining differential mobility spectrometry with electron- and collision-based tandem mass spectrometry," *Journal of The American Society for Mass Spectrometry*, vol. 28, pp. 1374–1381, Apr. 2017.

[12] S. W. C. Walker, A. Mark, B. Verbuyst, B. Bogdanov, J. L. Campbell, and W. S. Hopkins, "Characterizing the tautomers of protonated aniline using differential mobility spectrometry and mass spectrometry," *The Journal of Physical Chemistry A*, vol. 122, no. 15, pp. 3858–3865, 2018. PMID: 29219313.

[13] J. L. Campbell, A. M.-C. Yang, L. R. Melo, and W. S. Hopkins, "Studying gas-phase interconversion of tautomers using differential mobility spectrometry," *Journal of The American Society for Mass Spectrometry*, vol. 27, pp. 1277–1284, Apr. 2016.

[14] C. S. Hansen, B. B. Kirk, S. J. Blanksby, R. A. J. O'Hair, and A. J. Trevitt, "Uv photodissociation action spectroscopy of haloanilinium ions in a linear quadrupole ion trap mass spectrometer," *Journal of the American Society for Mass Spectrometry*, vol. 24, no. 6, pp. 932–940, 2013. PMID: 23609184.

[15] J. S. Brodbelt, "Photodissociation mass spectrometry: new tools for characterization of biological molecules," *Chem. Soc. Rev.*, vol. 43, pp. 2757–2783, 2014.

[16] X. Zhang, X. Liang, H. Xiao, and Q. Xu, "Direct characterization of bitter acids in a crude hop extract by liquid chromatography-atmospheric pressure chemical ionization mass spectrometry," *Journal of the American Society for Mass Spectrometry*, vol. 15, no. 2, pp. 180 – 187, 2004.

[17] A. Anwar, J. Psutka, *et al.*, "Separating and probing tautomers of protonated nucleobases using differential mobility spectrometry," *International Journal of Mass Spectrometry*, vol. 492, pp. 174–181, 2018.

[18] H. Keller, A. K. Weickhmann, T. Bock, and J. Wöhnert, "Adenine protonation enables cyclic-di-gmp binding to cyclic-gamp sensing riboswitches," *RNA*, vol. 24, no. 10, p. 1390–1402, 2018.

[19] E. Fuchs, C. Falschlunger, R. Micura, and K. Breuker, "The effect of adenine protonation on RNA phosphodiester backbone bond cleavage elucidated by deaza-nucleobase modifications and mass spectrometry," *Nucleic Acids Research*, vol. 47, pp. 7223–7234, 07 2019.

[20] H. Borsdorf and G. A. Eiceman, "Ion mobility spectrometry: Principles and applications," *Applied Spectroscopy Reviews*, vol. 41, no. 4, pp. 323–375, 2006.

[21] V. Gabelica and E. Marklund, "Fundamentals of ion mobility spectrometry," *Current Opinion in Chemical Biology*, vol. 42, pp. 51 – 59, 2018. Omics.

[22] S. J. Allen, K. Giles, T. Gilbert, and M. F. Bush, "Ion mobility mass spectrometry of peptide, protein, and protein complex ions using a radio-frequency confining drift cell," *Analyst*, vol. 141, pp. 884–891, 2016.

[23] W. S. Hopkins, "Chapter four - dynamic clustering and ion microsolvation," in *Advances in Ion Mobility-Mass Spectrometry: Fundamentals, Instrumentation and Applications* (W. A. Donald and J. S. Prell, eds.), vol. 83 of *Comprehensive Analytical Chemistry*, pp. 83 – 122, Elsevier, 2019.

[24] S. Zhu, J. L. Campbell, I. Chernushevich, J. C. Y. Le Blanc, and D. J. Wilson, "Differential mobility spectrometry-hydrogen deuterium exchange (dms-hdx) as a probe of protein conformation in solution," *Journal of the American Society for Mass Spectrometry*, vol. 27, no. 6, pp. 991–999, 2016. PMID: 26965162.

[25] J. L. Campbell, A. M.-C. Yang, L. R. Melo, and W. S. Hopkins, "Studying gas-phase interconversion of tautomers using differential mobility spectrometry," *Journal of the American Society for Mass Spectrometry*, vol. 27, no. 7, pp. 1277–1284, 2016. PMID: 27094827.

[26] N. J. A. Coughlan, P. J. J. Carr, S. C. Walker, C. Zhou, M. Guna, J. L. Campbell, and W. S. Hopkins, "Measuring electronic spectra of differential mobility-selected ions in the gas phase," *Journal of the American Society for Mass Spectrometry*, vol. 31, no. 2, pp. 405–410, 2020. PMID: 32031386.

[27] S. J. P. Marlton, B. I. McKinnon, B. Ucur, J. P. Bezzina, S. J. Blanksby, and A. J. Trevitt, "Discrimination between protonation isomers of quinazoline by ion mobility and uv-photodissociation action spectroscopy," *The Journal of Physical Chemistry Letters*, vol. 11, no. 10, pp. 4226–4231, 2020. PMID: 32368922.

[28] J. S. Brodbelt, L. J. Morrison, and I. Santos, "Ultraviolet photodissociation mass spectrometry for analysis of biological molecules," *Chemical Reviews*, vol. 120, no. 7, pp. 3328–3380, 2020. PMID: 31851501.

[29] E. F. van Dishoeck and R. Visser, "Molecular photodissociation," 2011.

[30] R. Schinke, *Photodissociation Dynamics: Spectroscopy and Fragmentation of Small Polyatomic Molecules*. Cambridge Monographs on Atomic, Molecular and Chemical Physics, Cambridge University Press, 1993.

[31] J. Hollas, *Modern Spectroscopy*. Wiley, 2004.

[32] M. Orio, D. A. Pantazis, and F. Neese, "Density functional theory," *Photosynthesis Research*, vol. 102, pp. 443–453, Dec 2009.

[33] P. Hohenberg and W. Kohn, "Inhomogeneous electron gas," *Phys. Rev.*, vol. 136, pp. B864–B871, Nov 1964.

[34] W. Kohn and L. J. Sham, "Self-consistent equations including exchange and correlation effects," *Phys. Rev.*, vol. 140, pp. A1133–A1138, Nov 1965.

[35] *What is Density Functional Theory?*, ch. 1, pp. 1–33. John Wiley Sons, Ltd, 2009.

[36] A. D. Becke, "Density-functional exchange-energy approximation with correct asymptotic behavior," *Phys. Rev. A*, vol. 38, pp. 3098–3100, Sep 1988.

[37] J. P. Perdew, K. Burke, and M. Ernzerhof, "Generalized gradient approximation made simple," *Phys. Rev. Lett.*, vol. 77, pp. 3865–3868, Oct 1996.

[38] C. Lee, W. Yang, and R. G. Parr, "Development of the colle-salvetti correlation-energy formula into a functional of the electron density," *Phys. Rev. B*, vol. 37, pp. 785–789, Jan 1988.

[39] C. Adamo and D. Jacquemin, "The calculations of excited-state properties with time-dependent density functional theory," *Chem. Soc. Rev.*, vol. 42, pp. 845–856, 2013.

[40] E. K. U. Gross and N. T. Maitra, "Introduction to TDDFT," in *Fundamentals of Time-Dependent Density Functional Theory*, pp. 53–99, Springer Berlin Heidelberg, 2012.

[41] A. S. Coolidge, H. M. James, and R. D. Present, "A study of the franck-condon principle," *Journal of Chemical Physics*, vol. 4, pp. 193–211, 1936.

[42] N. S. Bayliss and E. G. McRae, "Solvent effects in organic spectra: Dipole forces and the franck-condon principle," *Journal of Physical Chemistry*, vol. 58, pp. 1002–1006, 1954.

[43] A. McC., *Aufenthaltswahrscheinlichkeit harmonischer Oszillator.png.* Oct 2007.

[44] P. Atkins, J. De Paula, and V. Walters, *Physical Chemistry.* W. H. Freeman, 2006.

[45] J. B. Coon, R. E. DeWames, and C. M. Loyd, "The franck-condon principle and the structures of excited electronic states of molecules," *Journal of Molecular Spectroscopy*, vol. 8, pp. 285–299, 1962.

[46] F. J. Avila Ferrer and F. Santoro, "Comparison of vertical and adiabatic harmonic approaches for the calculation of the vibrational structure of electronic spectra," *Phys. Chem. Chem. Phys.*, vol. 14, pp. 13549–13563, 2012.

[47] A. Hazra, H. H. Chang, and M. Nooijen, "First principles simulation of the uv absorption spectrum of ethylene using the vertical franck-condon approach," *The Journal of Chemical Physics*, vol. 121, no. 5, pp. 2125–2136, 2004.

[48] J. P. Götze, B. Karasulu, and W. Thiel, "Computing uv/vis spectra from the adiabatic and vertical franck-condon schemes with the use of cartesian and internal coordinates," *The Journal of Chemical Physics*, vol. 139, no. 23, p. 234108, 2013.

[49] T. Pacher, L. S. Cederbaum, and H. Köppel, "Approximately diabatic states from block diagonalization of the electronic hamiltonian," *The Journal of Chemical Physics*, vol. 89, no. 12, pp. 7367–7381, 1988.

[50] A. Hazra and M. Nooijen, "Vibronic coupling in the excited cationic states of ethylene: Simulation of the photoelectron spectrum between 12 and 18ev," *The Journal of Chemical Physics*, vol. 122, no. 20, p. 204327, 2005.

[51] J. Endicott, "Fully quadratic vibronic model of electronic transitions through conical intersections," 2014.

[52] H. H. Chang, "From electronic structure theory to molecular spectroscopy," 2003.

[53] A. Hazbra, "Electronic absorption spectra from first principles," 2005.

[54] J. Endicott, "Generating vibronic coupling models and simulating photoelectron spectra," 2012.

[55] M. Nooijen, "Vibronic notes," 2011.

[56] M. Nooijen, "Ccce calgary 2012:construction of accurate vibronic models and the simulation of electronic spectra," 2012.

[57] "The multiconfiguration time-dependent hartree (mctdh) method: a highly efficient algorithm for propagating wavepackets," *Physics Reports*, vol. 324, no. 1, pp. 1 – 105, 2000.

[58] "The multi-configurational time-dependent hartree approach," *Chemical Physics Letters*, vol. 165, no. 1, pp. 73 – 78, 1990.

[59] G. A. Worth, M. H. Beck, A. Jäckle, and H.-D. Meyer. The MCTDH Package, Version 8.4 (2007). Current version: 8.4.18 (2019). See http://mctdh.uni-hd.de.

[60] R. Barrow, D. Millen, and D. Long, *Molecular Spectroscopy*. No. v. 2 in Molecular Spectroscopy: A Specialist Periodical Report, Chemical Society, 1973.

[61] B. Jaskula, P. Kafarski, G. Aerts, and L. De Cooman, "A kinetic study on the isomerization of hop -acids," *Journal of Agricultural and Food Chemistry*, vol. 56, no. 15, pp. 6408–6415, 2008. PMID: 18598038.

[62] HerrSchnapps, *Cross-section of hop cone.svg*. May 2008.

[63] M. A. Farag, A. Porzel, J. Schmidt, and L. A. Wessjohann, "Metabolite profiling and fingerprinting of commercial cultivars of humulus lupulus l. (hop): a comparison of ms and nmr methods in metabolomics," *Metabolomics*, vol. 8, pp. 492–507, Jun 2012.

[64] "Chapter 2 - the alpha acids," in *Chemistry and Analysis of Hop and Beer Bitter Acids* (M. VERZELE and D. DE KEUKELEIRE, eds.), vol. 27 of *Developments in Food Science*, pp. 17 – 43, Elsevier, 1991.

[65] O. Oladokun, K. Smart, and D. Cook, "An improved hplc method for single-run analysis of the spectrum of hop bittering compounds usually encountered in beers," *Journal of the Institute of Brewing*, vol. 122, no. 1, pp. 11–20, 2016.

[66] D. Intelmann, O. Demmer, N. Desmer, and T. Hofmann, "18o stable isotope labeling, quantitative model experiments, and molecular dynamics simulation studies on the trans-specific degradation of the bitter tasting iso-alpha-acids of beer," *Journal of agricultural and food chemistry*, vol. 57, p. 11014—11023, November 2009.

[67] "Chapter 5 - the isohumulones," in *Chemistry and Analysis of Hop and Beer Bitter Acids* (M. VERZELE and D. DE KEUKELEIRE, eds.), vol. 27 of *Developments in Food Science*, pp. 88 – 126, Elsevier, 1991.

[68] J. Christensen, A. M. Ladefoged, and L. Nørgaard, "Rapid determination of bitterness in beer using fluorescence spectroscopy and chemometrics," *Journal of the Institute of Brewing*, vol. 111, no. 1, pp. 3–10, 2005.

[69] Zhang, Qiuying, "Characterizing humulone content in beer using differential mobility spectrometry," 2018.

[70] T. Yanai, D. P. Tew, and N. C. Handy, "A new hybrid exchange–correlation functional using the coulomb-attenuating method (cam-b3lyp)," *Chemical Physics Letters*, vol. 393, no. 1, pp. 51 – 57, 2004.

[71] D. De Keukeleire, A. Heyerick, K. Huvaere, L. Skibsted, and M. Andersen, "Beer lightstruck flavor: The full story," *Cerevisia*, vol. 33, pp. 133–144, 01 2008.

[72] A. Heyerick, Y. Zhao, P. Sandra, K. Huvaere, F. Roelens, and D. D. Keukeleire, "Photolysis of hop-derived trans-iso--acids and trans-tetrahydroiso--acids: product identification in relation to the lightstruck flavour of beer," *Photochem. Photobiol. Sci.*, vol. 2, pp. 306–314, 2003.

[73] B. Marchetti, T. N. V. Karsili, and M. N. R. Ashfold, "Exploring norrish type i and type ii reactions: an ab initio mechanistic study highlighting singlet-state mediated chemistry," *Phys. Chem. Chem. Phys.*, vol. 21, pp. 14418–14428, 2019.

[74] *Beer and ESR Spin Trapping.* Beer in Health and Disease Prevention.

[75] H. Egts, D. J. Durben, J. A. Dixson, and M. H. Zehfus, "A multicomponent uv analysis of - and -acids in hops," *Journal of Chemical Education*, vol. 89, no. 1, pp. 117–120, 2012.

[76] G. Alderton, G. F. Bailey, J. C. Lewis, and F. Stitt, "Spectrophotometric determination of humulone complex and lupulone in hops," *Analytical Chemistry*, vol. 26, no. 6, pp. 983–992, 1954.

[77] F. R. Sharpe and I. H. L. Ormrod, "Fast isomerisation of humulone by photo-reaction: Preparation of an hplc standard," *Journal of the Institute of Brewing*, vol. 97, no. 1, pp. 33–37, 1991.

[78] O. Kornysova, Z. Stanius, K. Obelevicius, O. Ragazinskiene, E. Skrzydlewska, and A. Maruska, "Capillary zone electrophoresis method for determination of bitter (- and -) acids in hop (humulus lupulus l.) cone extracts," *Advances in medical sciences*, vol. 54, pp. 41–6, 02 2009.

[79] V. Singh, B. I. Fedeles, and J. M. Essigmann, "Role of tautomerism in rna biochemistry," *RNA*, vol. 21, no. 1, p. 1–13, 2014.

[80] H. Y. Zhao, K.-C. Lau, *et al.*, "Unveiling the complex vibronic structure of the canonical adenine cation," *Physical Chemistry Chemical Physics*, vol. 20, pp. 20756–20765, 2018.

[81] A. Dang, Y. Liu, and F. Tureček, "Uv–vis action spectroscopy of guanine, 9-methylguanine, and guanosine cation radicals in the gas phase," *The Journal of Physical Chemistry A*, vol. 123, no. 15, pp. 3272–3284, 2019. PMID: 30912657.

[82] G. C. P. van Zundert, S. Jaeqx, G. Berden, J. M. Bakker, K. Kleinermanns, J. Oomens, and A. M. Rijs, "Ir spectroscopy of isolated neutral and protonated adenine and 9-methyladenine," *ChemPhysChem*, vol. 12, no. 10, pp. 1921–1927, 2011.

[83] K. Rajabi, K. Theel, E. A. L. Gillis, G. Beran, and T. D. Fridgen, "The structure of the protonated adenine dimer by infrared multiple photon dissociation spectroscopy and electronic structure calculations," *The Journal of Physical Chemistry A*, vol. 113, no. 28, pp. 8099–8107, 2009. PMID: 19548662.

[84] D. Nolting, R. Weinkauf, I. V. Hertel, and T. Schultz, "Excited-state relaxation of protonated adenine," *ChemPhysChem*, vol. 8, no. 5, pp. 751–755, 2007.

[85] H. Kang, G. Féraud, C. Dedonder-Lardeux, and C. Jouvet, "New method for double-resonance spectroscopy in a cold quadrupole ion trap and its application to uv–uv hole-burning spectroscopy of protonated adenine dimer," *The Journal of Physical Chemistry Letters*, vol. 5, no. 15, pp. 2760–2764, 2014. PMID: 26277976.

[86] S. Øvad Pedersen and K. S. others, "Gas-phase spectroscopy of protonated adenine, adenosine 5-monophosphate and monohydrated ions," *Physical Chemistry Chemical Physics*, vol. 15, pp. 19748–19752, 2013.

[87] C. Marian, D. Nolting, and R. Weinkauf, "The electronic spectrum of protonated adenine: Theory and experiment," *Phys. Chem. Chem. Phys.*, vol. 7, pp. 3306–3316, 2005.

[88] N. R. Cheong, S. H. Nam, H. S. Park, S. Ryu, J. K. Song, S. M. Park, M. Pérot, B. Lucas, M. Barat, J. A. Fayeton, and C. Jouvet, "Photofragmentation in selected tautomers of protonated adenine," *Phys. Chem. Chem. Phys.*, vol. 13, pp. 291–295, 2011.

[89] E. Matthews and C. E. H. Dessent, "Experiment and theory confirm that uv laser photodissociation spectroscopy can distinguish protomers formed via electrospray," *Phys. Chem. Chem. Phys.*, vol. 19, pp. 17434–17440, 2017.

[90] S. J. P. Marlton, B. I. McKinnon, B. Ucur, A. T. Maccarone, W. A. Donald, S. J. Blanksby, and A. J. Trevitt, "Selecting and identifying gas-phase protonation isomers of nicotineh+ using combined laser, ion mobility and mass spectrometry techniques," *Faraday Discuss.*, vol. 217, pp. 453–475, 2019.

[91] M. Berdakin, G. Féraud, C. Dedonder-Lardeux, C. Jouvet, and G. A. Pino, "Excited states of protonated dna/rna bases," *Phys. Chem. Chem. Phys.*, vol. 16, pp. 10643–10650, 2014.

[92] M. J. Frisch, G. W. Trucks, H. B. Schlegel, G. E. Scuseria, M. A. Robb, J. R. Cheeseman, G. Scalmani, V. Barone, G. A. Petersson, H. Nakatsuji, X. Li, M. Caricato, A. V. Marenich, J. Bloino, B. G. Janesko, R. Gomperts, B. Mennucci, H. P. Hratchian, J. V. Ortiz, A. F. Izmaylov, J. L. Sonnenberg, D. Williams-Young, F. Ding, F. Lipparini, F. Egidi, J. Goings, B. Peng, A. Petrone, T. Henderson, D. Ranasinghe, V. G. Zakrzewski, J. Gao, N. Rega, G. Zheng, W. Liang, M. Hada,

M. Ehara, K. Toyota, R. Fukuda, J. Hasegawa, M. Ishida, T. Nakajima, Y. Honda, O. Kitao, H. Nakai, T. Vreven, K. Throssell, J. A. Montgomery, Jr., J. E. Peralta, F. Ogliaro, M. J. Bearpark, J. J. Heyd, E. N. Brothers, K. N. Kudin, V. N. Staroverov, T. A. Keith, R. Kobayashi, J. Normand, K. Raghavachari, A. P. Rendell, J. C. Burant, S. S. Iyengar, J. Tomasi, M. Cossi, J. M. Millam, M. Klene, C. Adamo, R. Cammi, J. W. Ochterski, R. L. Martin, K. Morokuma, O. Farkas, J. B. Foresman, and D. J. Fox, "Gaussian˜16 Revision C.01," 2016. Gaussian Inc. Wallingford CT.

[93] F. Neese, "Software update: the orca program system, version 4.0: Software update," *Wiley Interdisciplinary Reviews: Computational Molecular Science*, vol. 8, p. e1327, 07 2017.

[94] R. Berraud-Pache, F. Neese, G. Bistoni, and R. Izsák, "Unveiling the photophysical properties of boron-dipyrromethene dyes using a new accurate excited state coupled cluster method," *Journal of Chemical Theory and Computation*, vol. 16, no. 1, pp. 564–575, 2020. PMID: 31765141.

[95] M. Nooijen, "First-principles simulation of the uv absorption spectrum of ketene," *International Journal of Quantum Chemistry*, vol. 95, no. 6, pp. 768–783, 2003.

[96] H. Köuppel, W. Domcke, and L. S. Cederbaum, *Multimode Molecular Dynamics Beyond the Born-Oppenheimer Approximation*, pp. 59–246. John Wiley Sons, Ltd, 2007.

[97] H. Tamura, "Diabatization for time-dependent density functional theory: Exciton transfers and related conical intersections," *The Journal of Physical Chemistry A*, vol. 120, no. 46, pp. 9341–9347, 2016. PMID: 27801581.

[98] M. Beck, A. Jäckle, G. Worth, and H.-D. Meyer, "The multiconfiguration time-dependent hartree (mctdh) method: a highly efficient algorithm for propagating wavepackets," *Physics Reports*, vol. 324, no. 1, pp. 1 – 105, 2000.

[99] H.-D. Meyer, U. Manthe, and L. Cederbaum, "The multi-configurational time-dependent hartree approach," *Chemical Physics Letters*, vol. 165, no. 1, pp. 73 – 78, 1990.

[100] G. W. R. I. B. M. H. B. A. J. G. A. Worth, K. Giri and H.-D. Meyer, "The quantics package, version 1.1," *University of Birmingham, Birmingham, U.K.*, 2015.

[101] C. C. Nelson and J. A. McCloskey, "Collision-induced dissociation of adenine," *Journal of the American Chemical Society*, vol. 114, no. 10, pp. 3661–3668, 1992.

[102] S. Matsika, "Three-state conical intersections in nucleic acid bases," *The Journal of Physical Chemistry A*, vol. 109, no. 33, pp. 7538–7545, 2005. PMID: 16834123.

[103] W. M. I. Hassan, W. C. Chung, N. Shimakura, S. Koseki, H. Kono, and Y. Fujimura, "Ultrafast radiationless transition pathways through conical intersections in photo-excited 9h-adenine," *Phys. Chem. Chem. Phys.*, vol. 12, pp. 5317–5328, 2010.

[104] W. Credo Chung, Z. Lan, Y. Ohtsuki, N. Shimakura, W. Domcke, and Y. Fujimura, "Conical intersections involving the dissociative 1* state in 9h-adenine: a quantum chemical ab initio study," *Phys. Chem. Chem. Phys.*, vol. 9, pp. 2075–2084, 2007.

[105] S. Brøndsted Nielsen and T. I. Sølling, "Are conical intersections responsible for the ultrafast processes of adenine, protonated adenine, and the corresponding nucleosides?," *ChemPhysChem*, vol. 6, no. 7, pp. 1276–1281, 2005.

[106] L. Giacomozzi, G. D'Angelo, S. Diaz-Tendero, N. de Ruette, M. H. Stockett, M. Alcamí, H. Cederquist, H. T. Schmidt, and H. Zettergren, "Decay pathways for protonated and deprotonated adenine molecules," *The Journal of Chemical Physics*, vol. 151, no. 4, p. 044306, 2019.

[107] F. Santoro, "Diabatization and scripts.".

APPENDICES

Appendix A

Computational protocol for creating vibronic models

In this Appendix, the exact computational protocol for creating vibronic models and generating spectra is outlined. Example input files are provided in both a dropbox folder on the Hopkins group dropbox under Fiorella\vibronic\Examples.

All electronic structure calculations were conducted using the B3LYP/6-311++G(d,p) level of theory on Gaussian 16. The diabatization scheme and creation of vibronic model was performed using a series of scripts written by Fabrizio Santoro. [107] All scripts can be located on the Hopkins group dropbox under the folder Fiorella\vibronic\Santoro. The time-propagation and spectra generation was performed using the QUANTICS package. Quantics

Step 1. Define the ground state (GS) PES by performing an optimization and frequency

Input orientation:

Center Number	Atomic Number	Atomic Type	Coordinates (Angstroms) X	Y	Z
1	6	0	0.731758	0.779131	-0.000021
2	6	0	0.220616	-0.523959	0.000010
3	6	0	2.322292	-0.745310	-0.000008
4	7	0	2.082809	0.616020	-0.000022
5	1	0	2.772922	1.356952	-0.000032
6	1	0	3.325636	-1.144990	-0.000008
7	7	0	1.223333	-1.457544	0.000031
8	6	0	-1.261081	1.739540	-0.000024
9	7	0	0.020904	1.924893	-0.000038
10	6	0	-1.172857	-0.684879	0.000021
11	7	0	-1.867607	0.495991	0.000004
12	1	0	-1.940843	2.583306	-0.000033
13	7	0	-1.788822	-1.863289	0.000024
14	1	0	-1.222880	-2.701861	0.000074
15	1	0	-2.792102	-1.969741	0.000143
16	1	0	-2.881424	0.476700	-0.000001

(a) Input orientation

Harmonic frequencies (cm**-1), IR intensities (KM/Mole), Raman scattering activities (A**4/AMU), depolarization ratios for plane and unpolarized incident light, reduced masses (AMU), force constants (mDyne/A), and normal coordinates:

	1	2	3	4	5
	A	A	A	A	A
Frequencies ---	163.2802	207.3016	277.7730	278.2965	365.1485
Reduced masses ---	5.7153	4.1907	3.4755	5.2397	1.1968
Force constants ---	0.0898	0.1061	0.1580	0.2391	0.0940
IR Intensities ---	9.9039	26.4377	7.2609	0.2838	118.3966
Coord Atom Element:					
1 1 6	0.00000	-0.00000	0.02010	-0.00002	0.00000
2 1 6	0.00000	-0.00000	0.05299	-0.00006	0.00001

(b) Harmonic frequencies

calculation. The GS PES is modelled as being a harmonic potential. This is a satisfactory approximation because excitation events typically occur at the GS equilibrium geometry. An example input file is provided.

Step 2. Run an excited state calculation at the optimized geometry using TD-DFT using the same functional and basis set in Step 1. It is recommended to request for at least 5 excited states. The excited state energy levels found in this step define the adiabatic states. An example input file is provided.

Step 3. Using the results from the output (.log) file obtained in Step 1, prepare a prep.fc input file in accordance to the example provided. Change the number of atoms in the prep.fc input file to correspond with your system. In the .log file of the optimization and frequency calculation, search the document for the keyword **Input orientation**. Copy and paste all the numerical values underneath the dotted lines into your input number as shown in A.1a. Next, search the document for the keyword **Harmonic frequencies**. Copy and paste the remainder of the document into the input file, starting at the line enumerating the normal modes, as shown in A.1b. Run this input file with the executable prep.fc.e.

Step 4. Create a genepointder input file in accordance with the example provided by

changing the number of atoms, normal modes, and atom masses to match your system. Step two generated a *mass* file that contains the exact masses of the atoms in the system. Execute the script gene-pointder.e to read your input file. A Gaussian input file will be created that displaces the ground state geometry by a small amount δq_i along each normal mode. The geometry is displaced 6N times, where N represents the number of atoms in the system. After each displacement, the adiabatic states are recalculated by performing a TD-DFT calculation. Run the Gaussian input file. Once the Gaussian calculation is finished, convert the checkpoint files (.chk) for each new geometry into formal checkpoint files (.fchk) by executing the script formchk4script.

Step 5. Now, the diabatization scheme is run. Create an overdia input file using the example provided by adding the name of the Gaussian log file created in Step 4, along with the number of atoms, normal modes, and excited states for your system. Execute the script overdia-par.e by reading in the created input file.

Step 6. An analysis of the results from the diabatization is performed to generate to the vibronic model. Create a coupling input file using the example provided by including the name of the output file from step 5, and the correct number of atoms and normal modes for your system. Include the vertical excitation energies for the states of interest obtained in Step 2 in eV and include the normal mode frequencies obtained from Step 1 in wavenumber. Execute the script overdia_2_opfile.e by reading in th coupling input file. You will generate an operator file (.op) that will define the Hamiltonian used for the time-propagation step.

Step 7. Open the operator file and scroll to the end of the file. Above the end-operator keyword, include a section that defines the coupled states in accordance to the example in the example provided and in A.2. Ensure to add in the right amount of normal modes and excited states in your operator file. **Step 8.** Duplicate the operator file three times,

```
end-hamiltonian-section
HAMILTONIAN-SECTION_Ex
modes | el | v01 | v02 | v03 | v04 | v05 | v06 | v07 | v08 | v09|
modes  | v10 | v11 | v12 | v13 | v14 | v15 | v16 | v17 | v18|
modes  | v19 | v20 | v21 | v22 | v23 | v24 | v25 | v26 | v27|
modes  | v28 | v29 | v30 | v31 | v32 | v33 | v34 | v35 | v36|
modes  | v37 | v38 | v39 | v40 | v41 | v42 |

Ex_s00_s01                  |1 S1&2
Ex_s00_s02                  |1 S1&3
Ex_s00_s03                  |1 S1&4
Ex_s00_s04                  |1 S1&5
Ex_s00_s05                  |1 S1&6
Ex_s00_s06                  |1 S1&7
end-hamiltonian-section

end-operator
```

Figure A.2: Overlap Hamiltonian inclusion

and label one copy for each of the three Cartesian coordinates **x, y ,z**. Open the operator file and search the document for the keyword end-parameter-section. Above this keyword, add in a section on the transition electric dipole moments as shown the example provided and in the figure A.3. The transition electric dipole moments are taken from the TD-DFT calculation in Step 2. It is important to note that the dipole moment being selected is the value along the Cartesian coordinate in question.

Step 9. Prepare an MCTDH input file in accordance to the example provided. Ensure that the correct amount of normal modes is listed in each section of the input file. Within the SPF-BASIS-SECTION, ensure that each normal mode is followed by a string of numbers that total to the amount of excited states that are being studied. When each normal mode is comprised of a series of 1s, this is called Time-dependent-Hartree. Each excited state is being defined by an individual single particle function (SPF). When the normal mode is comprised of a series of numbers greater than one, this is called Multi-configurational time-depedent Hartree. Run this input file using the MCTDH suite. The calculation should be performed for each Cartesian coordinate.

```
#     Electronic transition moments
# ---------------------------------

# tmom in direction Ex
Ex_s00_s01                =      -0.0007    , ev
Ex_s00_s02                =      -0.0000    , ev
Ex_s00_s03                =      -0.2046    , ev
Ex_s00_s04                =      -0.0000    , ev
Ex_s00_s05                =      -0.0000    , ev
Ex_s00_s06                =      -0.1639    , ev


end-parameter-section
```

Figure A.3: Transition dipole moments inclusion

Step 9. The completion of the MCTDH calculation will yield an autocorrelation function file (auto). Within the directory of the MCTDH outputs, execute the command autospec84. This will generate a spectrum (.spectrum) file.

Step 10. From the spectrum file, copy the energy (eV) and G2 contribution onto excel. In the energy column, add in a linear shift comprised of $E_{VE(1)} - E_{ZPE}$, where $E_{VE(1)}$ is the energy of the first vertical excitation in eV found in Step 2 and E_{ZPE} is the zero-point energy of the GS structure obtained in Step 1. Finally, sum the contributions from each Cartesian coordinate and plot to generate the rotationally-averaged, vibronic spectrum.

Appendix B

Chapter 4: Supplementary information

Table B.1: The ESI conditions used to perform DMS-MS experiments on deprotonated isohumulone using a concentration of 100 ng/mL $ACN : H_2O$ solvent, as described in Chapter 4.

Parameter	$N_{2(g)}$	IPA modifier	MeOH modifier
ESI probe voltage (IS)	4500 V	4500 V	4.500 V
Nebulizing pressure (GS1)	30 psi	40 psi	40 psi
Auxiliary pressure (GS2)	10 psi	40 psi	40 psi
Source temperature (TEM)	70^oC	300^oC	300^oC
Curtain gas (CUR)	20 psi	20 psi	20 psi
Collision activated gas (CAD)	-3	-3	-3

Table B.2: The ESI conditions used to perform DMS-MS experiments on deprotonated humulone using a concentration of 100 ng/mL $ACN : H_2O$ solvent, as described in Chapter 4.

Parameter	IPA modifier
ESI probe voltage (IS)	4500 V
Nebulizing pressure (GS1)	20 psi
Auxiliary pressure (GS2)	0 psi
Source temperature (TEM)	0^oC
Curtain gas (CUR)	20 psi
Collision activated gas (CAD)	-3

Table B.3: The ESI conditions and photodissociation conditions used to collected photodissociation action spectrum of deprotonated humlone and deprotonated isohumulone, using a concentration of 100 ng/mL $ACN : H_2O$ solvent, as described in Chapter 4.

Parameters	humulone	isohumulone
Number of cycles	10	20
ESI probe voltage (IS)	4500 V	4500 V
Nebulizing pressure (GS1)	20 psi	30 psi
Auxiliary pressure (GS2)	0 psi	10 psi
Source temperature (TEM)	0^oC	70^oC
Curtain gas (CUR)	20 psi	20 psi
Collision activated gas (CAD)	-1	-1

B.1 Additional features from EMC mode

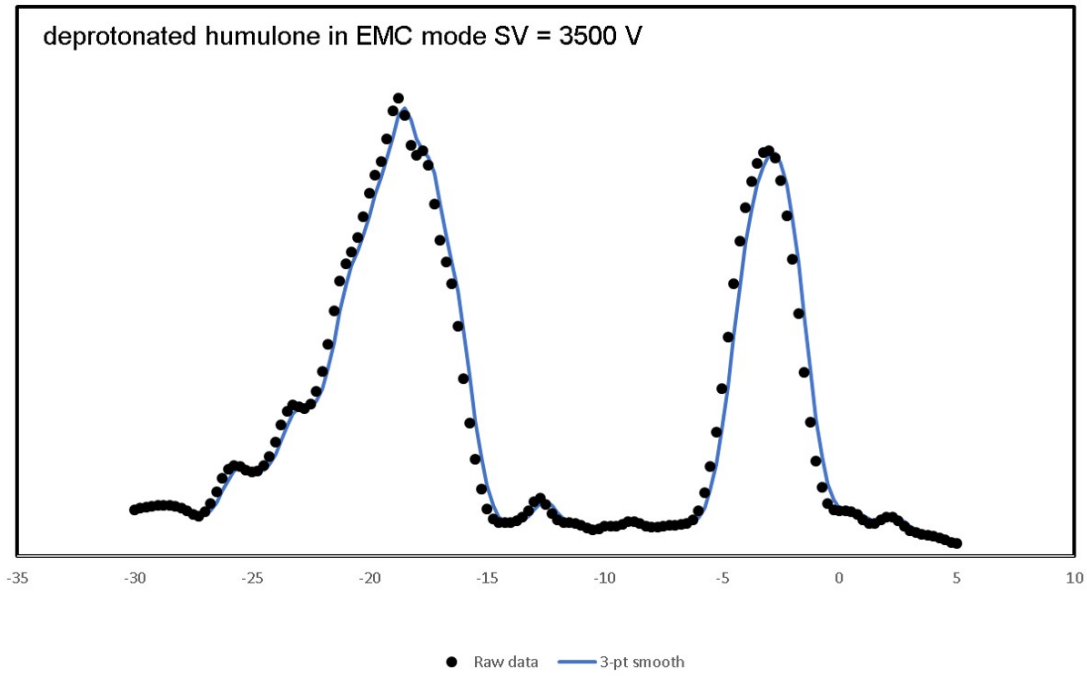

Figure B.1: Ionogram obtained for deprotonated humulone at SV = 3500 V in an IPA seeded environment when using EMC mode.

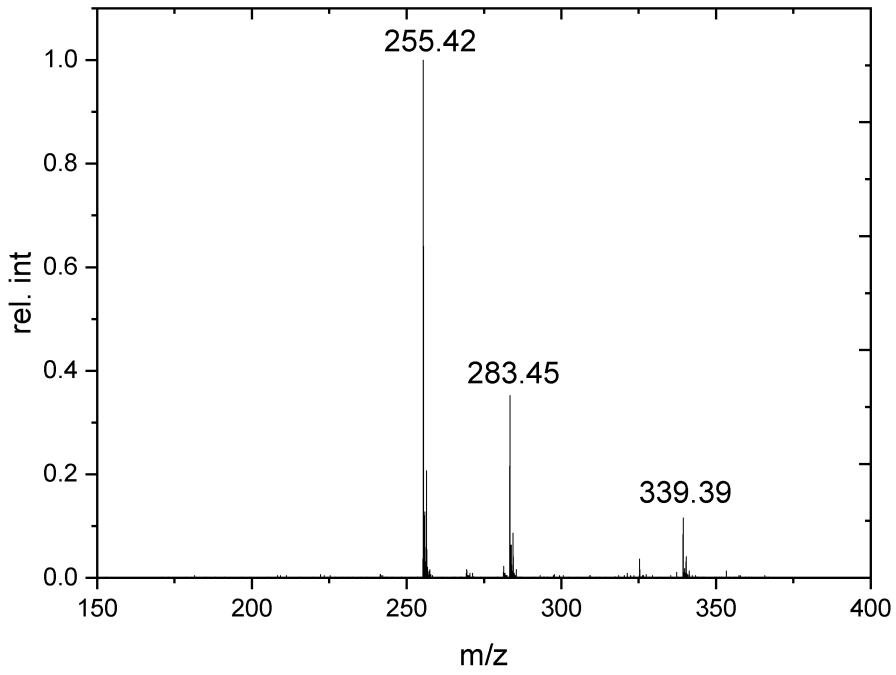

Figure B.2: The resultant MS under the new feature in the ionogram for deprontonated humulone in IPA at SV = 3500 V, shown in B.1

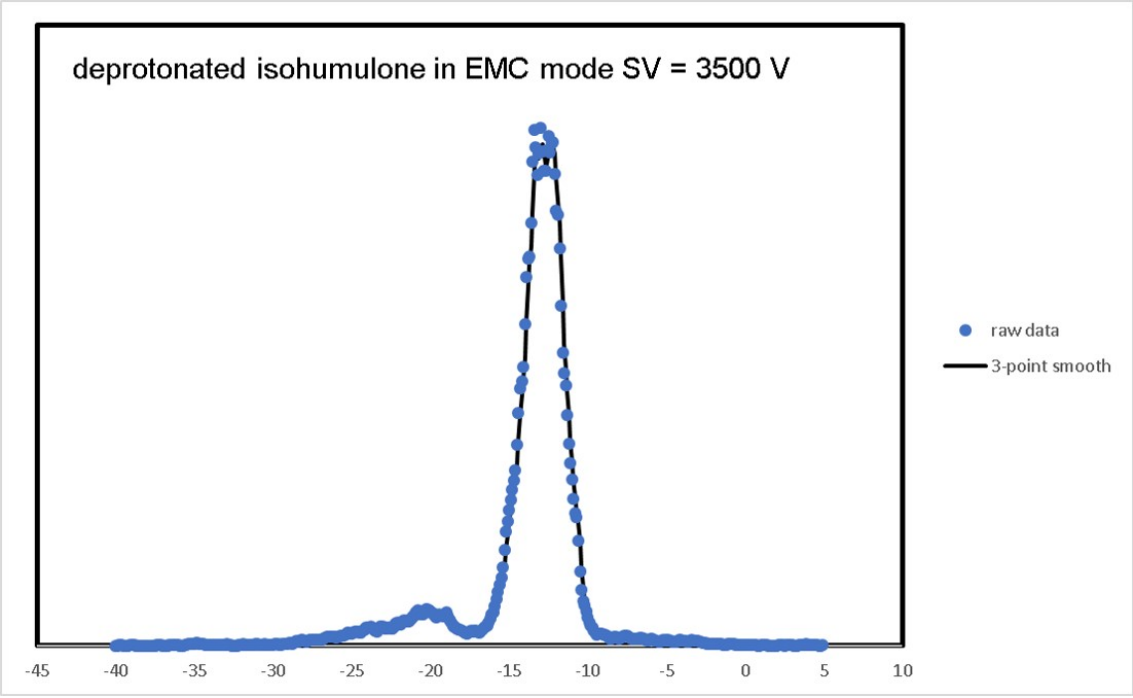

Figure B.3: Ionogram obtained for deprotonated isohumulone at SV = 3500 V in an IPA seeded environment when using EMC mode.

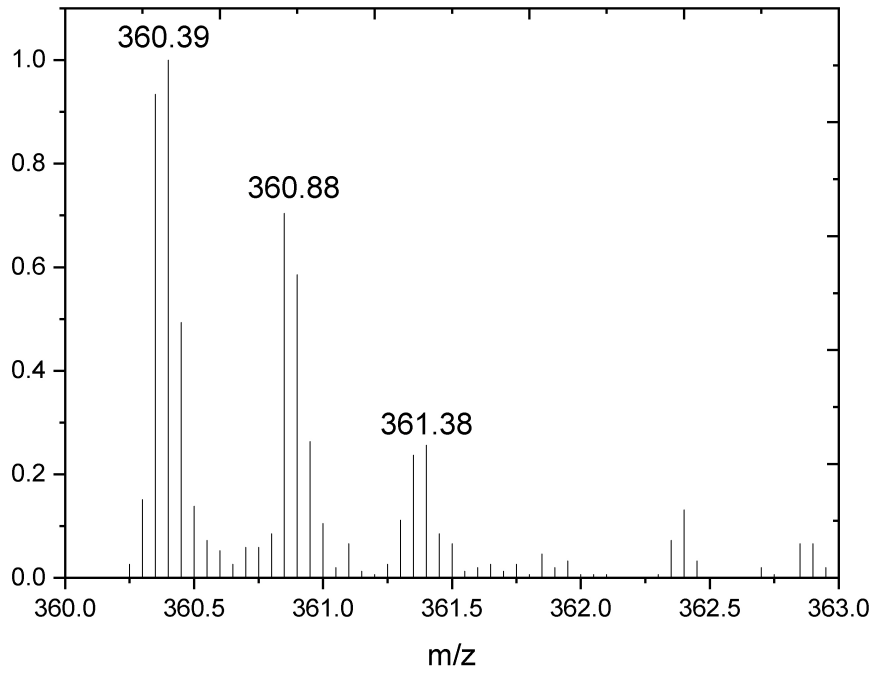

Figure B.4: The resultant MS under the new feature in the ionogram for deprontonated isohumulone in IPA at SV = 3500 V, shown in **??**

B.2 Observed mass peak shift during UVPD experiments

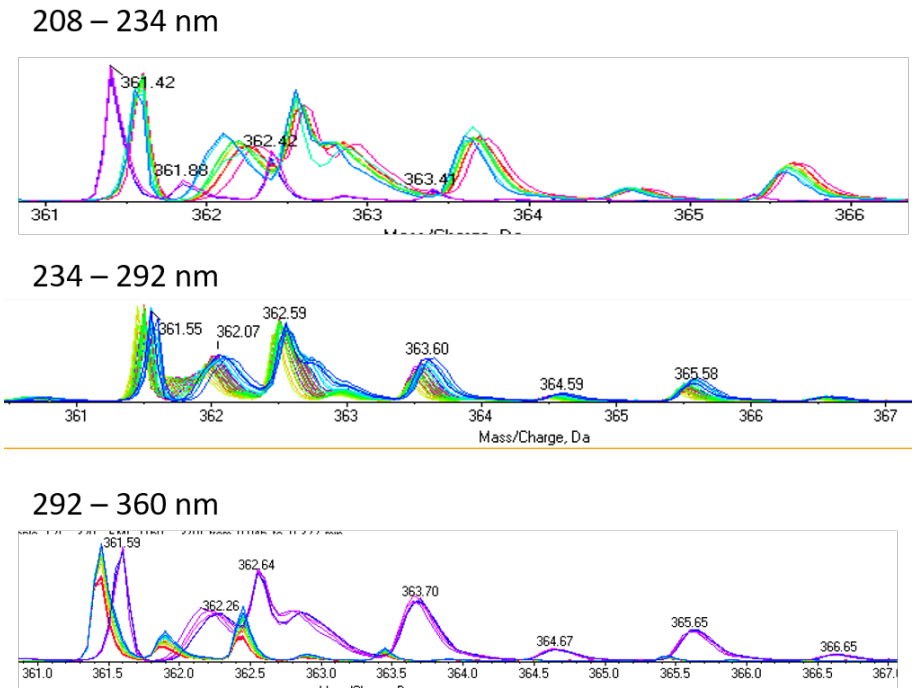

Figure B.5: The observed mass shift for deprotonated isohumulone during UVPD spectroscopy experiments. Due to frequency dependency of the mass shifts, likely caused by a change in photodepletion conditions rather than chemistry.

Appendix C

Chapter 5: Supplementary information

C.1 Repeated trials of protonated adenine spectra

In this section, we report the repeated collected spectra for protonated adenine. All experimental parameters are consistent with those reported in Chapter 5. The reported spectra found in Chapter 5 is the trial from January 8th, 2020. Broadening of the spectra is observed in the trials from January 29th and January 30th. However, the fingerprint region identifying the two tautomers, namely the observed shift in onset of the first vibronic progression, is maintained even in the broadened spectra. Broadening may be a result of high intensity of the laser beam, causing for complete fragmentation or initiation of multiphoton processes, or due to oversaturation of parent ion concentration.

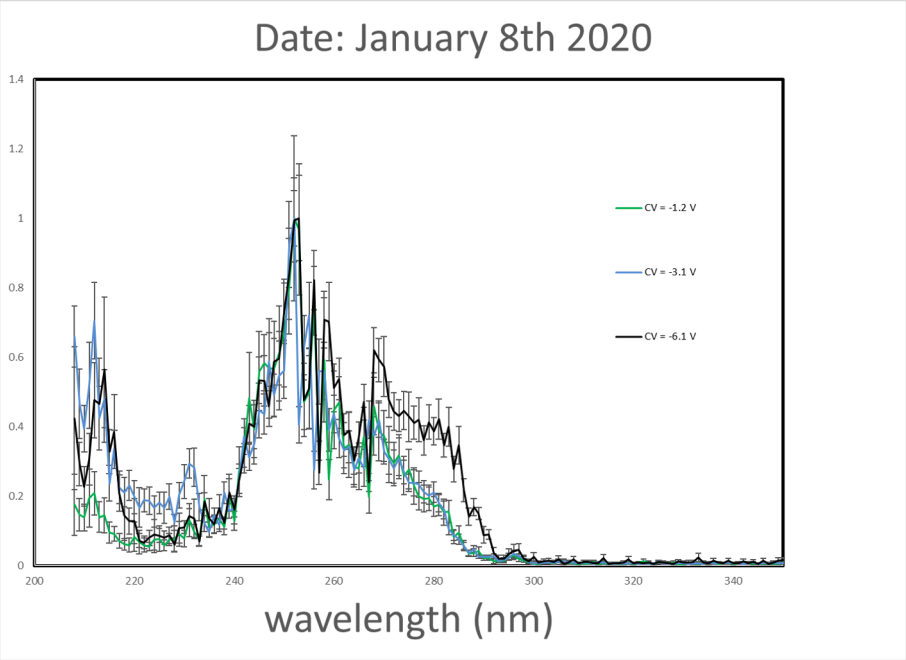

Figure C.1: The recorded action spectrum recorded at SV = 3500 V and CV = -1.2 V, -3.1 V, and -6.1 V in a pure $N_{2(g)}$ environment. ESI and photodissociation conditions match those reported in Chapter 5.

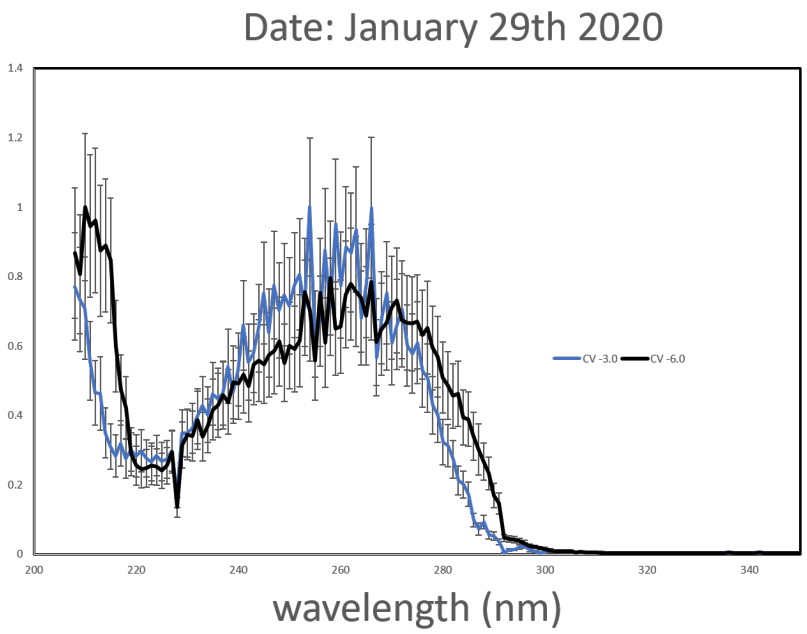

Figure C.2: The recorded action spectrum recorded at SV = 3500 V and CV = -3.0 V, and -6.0 V in a pure $N_{2(g)}$ environment. ESI and photodissociation conditions match those reported in Chapter 5. Wavelength reported in nanometres (nm).

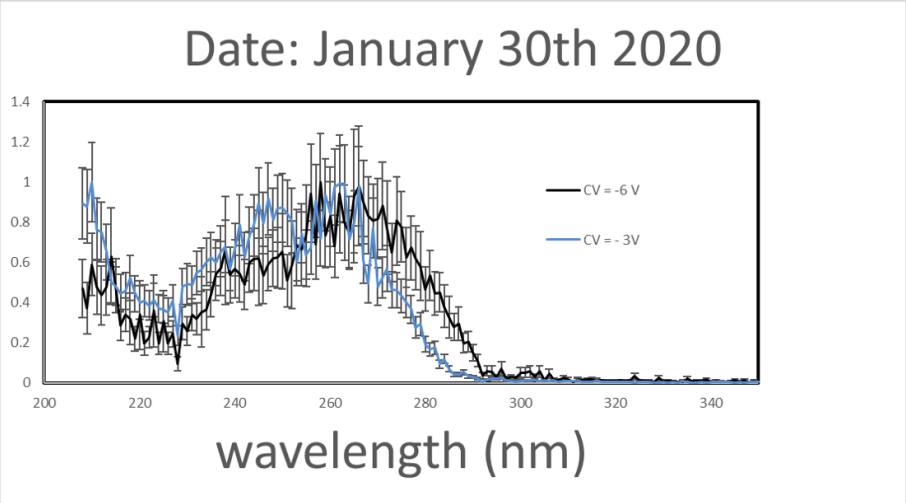

Figure C.3: The recorded action spectrum recorded at SV = 3500 V and CV = -3.0 V, and -6.0 V in a pure $N_{2(g)}$ environment. ESI and photodissociation conditions match those reported in Chapter 5. Wavelength reported in nanometres (nm).

C.2 Action spectrum of feature at CV = -2.1 V

In this section, the action spectrum obtained from the small feature at CV = -2.1 V of the SV = 3500 V ionogram for protonated adenine is reported.

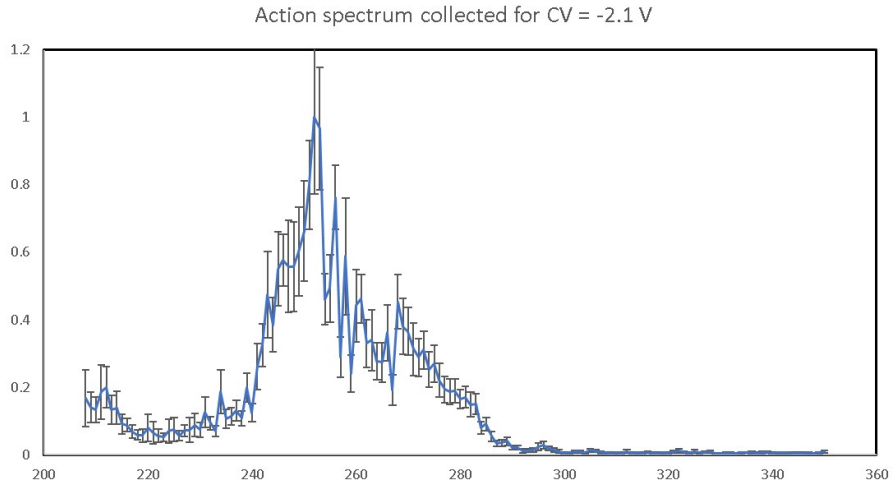

Figure C.4: The recorded action spectrum recorded at SV = 3500 V and CV = -2.1 V in a pure $N_{2(g)}$ environment. ESI and photodissociation conditions match those reported in Chapter 5.

C.3 Action spectra of individual fragmentation channels

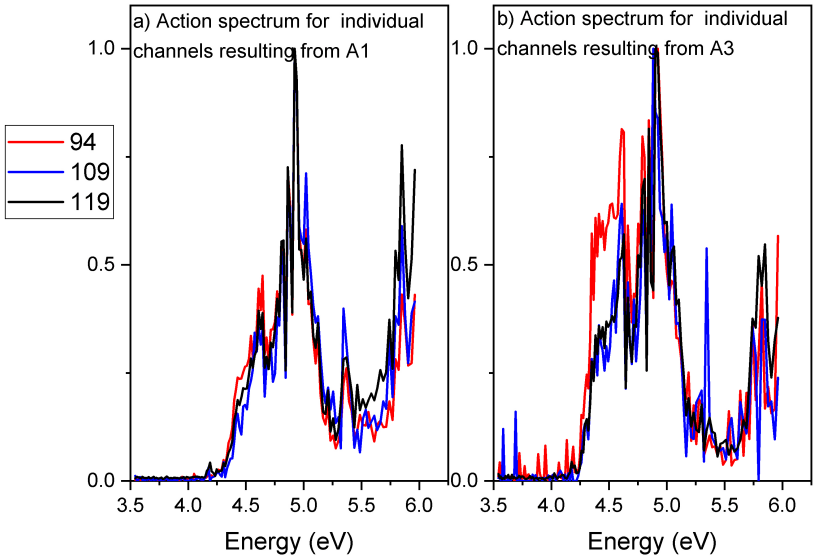

Figure C.5: The individual action spectrum for the individual dissociation channel for the fragments m/z = 119, 109, and 94, arising from parent a) A1 and b) A3. Conditions used to record these action spectra can be found in Chapter 5.

C.4 Determination of thermodynamic thresholds for fragmentation

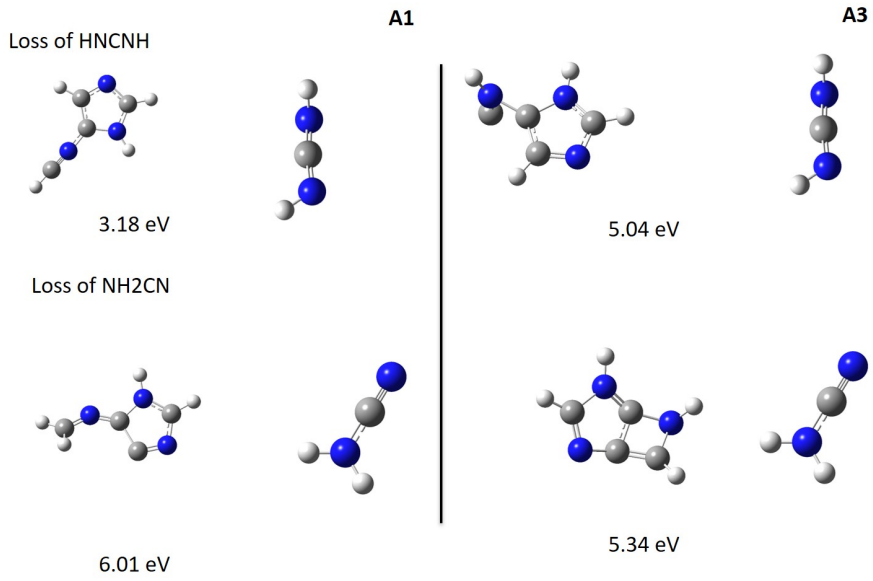

Figure C.6: The structures used to calculate fragmentation thresholds for structures A1 and A3. Structures were optimized at the B3LYP/6-311++G(d,p) on Gaussian16.

C.5 Cytosine

In this section, the experimental action spectrum, the theoretical vibronic spectrum obtained using an LVC Hamiltonian, and the relative energy ordering of the tautomers of protonated cytosine are shown. LVC models are created using the first fifteen excited states calculated at the B3LYP/6-311++G(d,p) level of theory, while reported electronic energies are determined using CCSD(T)/6-311++G(d,p).

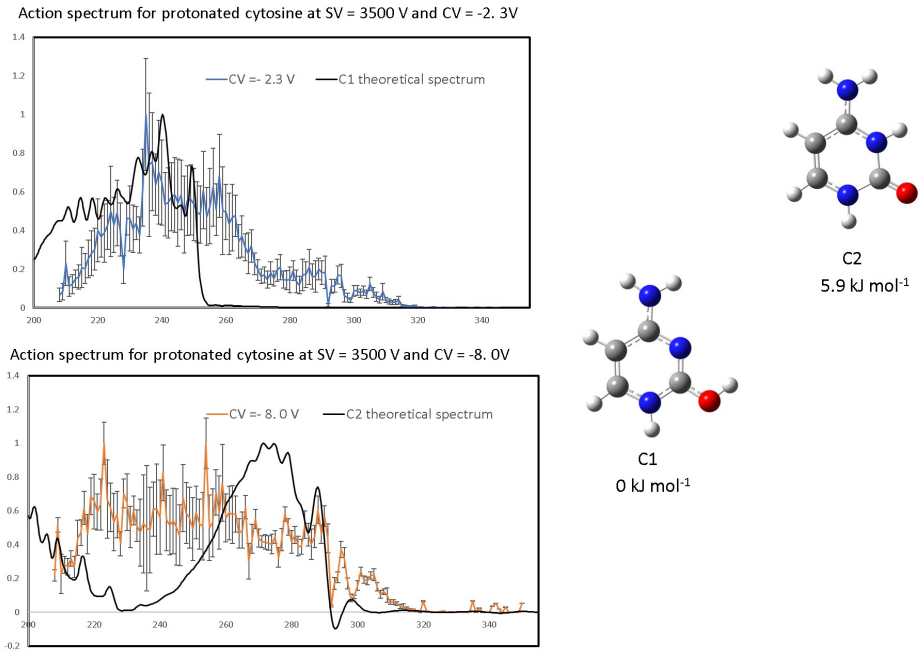

Figure C.7: Action spectrum obtained by selecting for protonated cytosine at m/z=112 at SV = 3500 V in a pure $N_{2(g)}$ environment. The ESI probe voltage was set to 5500 V, with a nebulizing pressure (GS1) and auxiliary pressure (GS2) of 20 psi and 0 psi, respectively. The source temperature was set to 32^oC. Nitrogen was used as both the curtain (20 psi) and collision activation gas(-3).

C.6 Uracil

In this section, the experimental action spectrum, the theoretical vibronic spectrum obtained using an LVC Hamiltonian, and the relative energy ordering of the tautomers of protonated uracil are shown. LVC models are created using the first fifteen excited states calculated at B3LYP/6-311++G(d,p) level of theory, while reported electronic energies are determined using CCSD(T)/6-311++G(d,p).

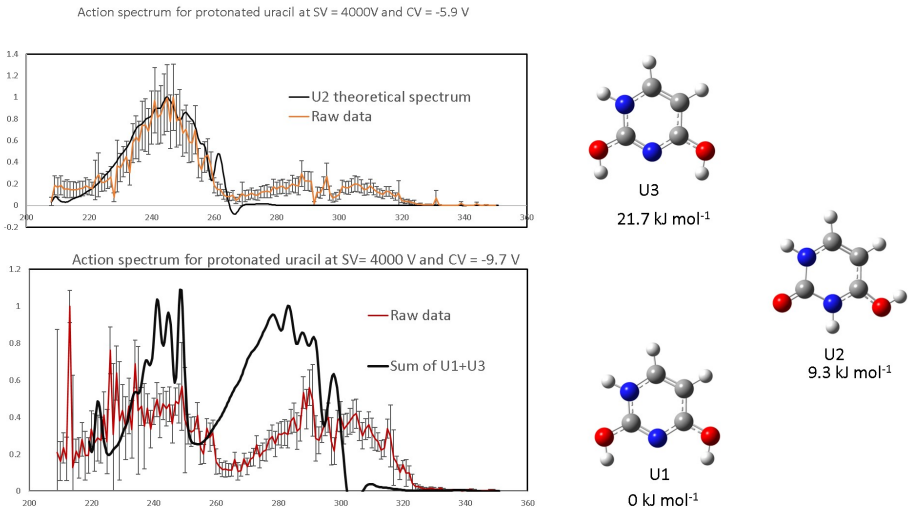

Figure C.8: Action spectrum obtained by selecting for protonated uracil at m/z=113 at SV = 4000 V in a pure $N_{2(g)}$ environment. The ESI probe voltage was set to 5000 V, with a nebulizing pressure (GS1) and auxiliary pressure (GS2) of 20 psi and 20 psi, respectively. The source temperature was set to 100^oC. Nitrogen was used as both the curtain (20 psi) and collision activation gas(-3).

C.7 MCTDH parameters and sample input file

In this section, the parameters selected for all QUANTICS simulations are shown in a sample calculation.

C.7.1 Input file

RUN-SECTION

name = A1_tdh_y_15_Santoro propagation

tfinal = 1000.0 tout = 0.2 tpsi= 1.0

psi auto=once steps gridpop

title =Adenine

end-run-section

OPERATOR-SECTION

oppath = .

opname = op_A1_15_y_2

end-operator-section